FABRICATION, SELECTED MICROSTRUCTURE-PROPERTY CORRELATIONS AND APPLICATIONS OF Si NANOWALLS

By

ANIL KUMAR BEHERA
Enrolment No. : PHYS 02 2014 04 008

Indira Gandhi Centre for Atomic Research, Kalpakkam, India.

A thesis submitted to the
Board of Studies in Physical Sciences
In partial fulfillment of requirements
for the Degree of
DOCTOR OF PHILOSOPHY
of
HOMI BHABHA NATIONAL INSTITUTE

September, 2020

Homi Bhabha National Institute

Recommendations of the Viva Voce Committee

As members of the Viva Voce Committee, we certify that we have read the dissertation prepared by **Anil Kumar Behera** entitled **"Fabrication, selected microstructure-property correlations and applications of Si nanowalls"** and recommend that it may be accepted as fulfilling the thesis requirement for the award of Degree of Doctor of Philosophy.

Chairman: Dr. M. Kamruddin Date: 20/5/2021

Guide/ Convener: Dr. Tom Mathews Date: 20/05/2021
Mathews

External Examiner: Dr. Harish C. Barshilia
Barshilia
Date: May 20, 2021

Member 1: Dr. K. I. Gnanasekar Date: 20-05-2021
Gnanasekar

Member 2: Dr. Arup Dasgupta Date: 20-05-2021

Member 3: Dr. T. R. Ravindran Date: 20/5/2021
T R Ravindran

Final approval and acceptance of this thesis is contingent upon the candidate's submission of the final copies of the thesis to HBNI.

I hereby certify that, I have read this thesis prepared under my direction and recommend that it may be accepted as fulfilling the thesis requirement.

Date: 20/05/2021
Place: IGCAR/Kalpakkam

Mathews
Dr. Tom Mathews
(Guide)

Homi Bhabha National Institute

Recommendations of the Viva Voce Committee

As members of the Viva Voce Committee, we certify that we have read the dissertation prepared by **Anil Kumar Behera** entitled **"Fabrication, selected microstructure-property correlations and applications of Si nanowalls"** and recommend that it may be accepted as fulfilling the thesis requirement for the award of Degree of Doctor of Philosophy.

Chairman: Dr. M. Kamruddin Date: 20/5/2021

Guide/ Convener: Dr. Tom Mathews Date: 20/05/2021

External Examiner: Dr. Harish C. Barshilia

Date: May 20, 2021

Member 1: Dr. K. I. Gnanasekar Date: 20-05-2021

Member 2: Dr. Arup Dasgupta Date: 20-05-2021

Member 3: Dr. T. R. Ravindran Date: 20/5/2021

Final approval and acceptance of this thesis is contingent upon the candidate's submission of the final copies of the thesis to HBNI.

I hereby certify that, I have read this thesis prepared under my direction and recommend that it may be accepted as fulfilling the thesis requirement.

Date: 20/05/2021
Place: IGCAR/Kalpakkam

Dr. Tom Mathews
(Guide)

STATEMENT BY AUTHOR

This dissertation has been submitted in partial fulfillment of requirements for an advanced degree at Homi Bhabha National Institute (HBNI) and is deposited in the Library to be made available to borrowers under rules of the HBNI.

Brief quotations from this dissertation are allowable without special permission, provided that accurate acknowledgement of source is made. Requests for permission for extended quotation from or reproduction of this manuscript in whole or in part may be granted by the Competent Authority of HBNI when in his or her judgment the proposed use of the material is in the interests of scholarship. In all other instances, however, permission must be obtained from the author.

Anil Kumar Behera

Anil Kumar Behera

DECLARATION

I, hereby declare that the investigation presented in the thesis has been carried out by me. The work is original and has not been submitted earlier as a whole or in part for a degree / diploma at this or any other Institution / University.

Anil Kumar Behera

Anil Kumar Behera

List of Publications arising from the thesis

Journal

1. "Synthesis, microstructure and visible luminescence properties of vertically aligned lightly doped porous silicon nanowalls"
   Anil K. Behera, R. N. Viswanath, C. Lakshmanan, K. K. Madapu, M. Kamruddin, Tom Mathews
   Microporous and Mesoporous Materials, **2019**, *273,* 99-106.
2. "Synthesis of silicon nanowalls exhibiting excellent antireflectivity and near super-hydrophobicity"
   Anil K. Behera, R. N. Viswanath, C. Lakshmanan, Tom Mathews, M. Kamruddin
   Nano-Structures & Nano-Objects, **2020,** *21,* 100424.
3. "Electrochemical studies on wafer-scale synthesized silicon nanowalls for supercapacitor application"
   Anil K. Behera, C. Lakshmanan, R. N. Viswanath, C. Poddar, Tom Mathews
   Bulletin of Materials Science, **2020**, *43,* 1-8.
4. "Hydrogen sensing behaviour of platinum and palladium functionalized silicon nanowalls"
   Anil K. Behera, R. N. Viswanath, T. Manovah David, A. K. Prasad, P. K. Ajikumar, Tom Mathews
   Applied Physics A, **2021,** *127,* 1-12.
5. "Light trapping and hydrophobic effects in silicon nanowall structures"
   Anil K. Behera, R. N. Viswanath, C. Lakshmanan, Neha Sharma, P. K. Ajikumar, S. Tripura Sundari, Tom Mathews
   Under Review (Materials Science in Semiconductor Processing)
6. "Effect of H_2O_2 concentration on morphology, antireflectivity and wettability of Si nanowalls prepared by metal assisted chemical etching"
   Anil K. Behera, R. N. Viswanath, C. Poddar, Tom Mathews
   Under Preparation

Conferences Proceedings and Abstracts

1. "Thermal oxidation and nitridation of Si nanowalls prepared by metal assisted chemical etching" (*Poster presentation*)
   Anil K. Behera, R. N. Viswanath, C. Lakshmanan, S. R. Polaki, R. M. Sarguna, Tom Mathews
   AIP Conference Proceedings, **2018**, *1942,* 050062-1–050062-4.
   62nd DAE Solid State Physics Symposium, BARC, Mumbai, 26-30 December, 2017.
2. "Luminescence behaviour of porous silicon in the presence of de-wetted silver" *(Poster presentation)*
   Anil K. Behera, C. Lakshmanan, R. N. Viswanath, T. Mathews, S. Dash

Second International Conference on Materials Science and Technology (ICMST-2016), Department of Physics, St. Thomas College, Palai, Kottayam-686574, Kerala, India, June 5-June 8, 2016.

3. "Growth mechanism of silver nanoparticles on silicon substrate by galvanic by galvanic displacement process" *(Poster presentation)*
Anil K. Behera, R. N. Viswanath, C. Lakshmanan, S. R. Polaki, G. Mangamma, Tom Mathews, S. Dash
International Conference on Advances in Nanomaterials and Nanotechnology (ICANN-2016), Centre for Nanoscience and Nanotechnology, Jamia Millia Islamia, New Delhi, India, November 4-November 5, 2016.

4. "Low energy positron beam studies on thermally oxidized Si nanowalls" *(Poster presentation)*
Anil K. Behera, C. Lakshmanan, R. N. Viswanath, R. Rajaraman, Tom Mathews, G. Amarendra
Research Scholars Meet on Materials Science and Engineering of Nuclear Materials (RSM MSENMS-2018), Indira Gandhi Centre for Atomic Research, Kalpakkam, Tamil Nadu, India, May 7-May 9, 2018.

5. "Transport properties of vertically aligned Si nanowall array" (Poster presentation)
Anil K. Behera, R. N. Viswanath, C. Lakshmanan, T. Mathews
5th International Conference on Nanoscience and Nanotechnology (ICONN-2019), Department of Physics and Nanotechnology, SRM Institute of Science and Technology, Kattankulathur-603203, Chengalpattu District, Tamil Nadu, India, January 28-January 30, 2019.

Workshops, Seminars and Webinars Participated/Attended

1. "One day workshop on Photovoltaics: Fundamentals, Device Characterization, Simulation and Emerging Concepts"
Department of Physics, Indian Institute of Technology Madras, March 10, 2018.

2. "Workshop on Nanomaterials for Improved Health Care"
Centre of Excellence for Nanotechnology Research & department of Humanities and Sciences, Aarupadai Veedu Institute of Technology, VMRF, Paiyanoor-603104, Kanchipuram, Tamil Nadu, India, January 30, 2019.

3. "Seminar on Structural Analysis through X-ray Diffraction (SAXD-2016)"
Department of Physics, Pondicherry University, Puducherry, India, January 28-January 19, 2016.

4. "Webinar on Materials Engineering and Technology"
Centre for Nanotechnology Research, Humanities and Science and Department of Mechanical Engineering-Aarupadai Veedu Institute of Technology (AVIT), VMRF, Paiyanoor-603104, Kanchipuram, Tamil Nadu, India, June 22- June 23, 2020.

Others Publications (Not included in the thesis)

1. "Microstructure studies in nanoporous Au: Effects on electro-oxidation"

C. Lakshmanan, **Anil K. Behera**, R. N. Viswanath, S. Amirthapandian, R. Rajaraman, G. Amarendra
Scripta Materialia, **2018**, *146*, 68-72.

2. "Variable energy positron beam Doppler broadening and microscopy studies of vertically aligned silicon nanowalls"
C. Lakshmanan, R. N. Viswanath, **Anil K. Behera**, P.K. Ajikumar, R. Rajaraman, G. Amarendra
Review (Nuclear Instruments and Methods in Physics Research, Section B)

3. "Study of infrared light induced electrochemical hydrogen evolution activity in flexible polymer supported carbon-palladium electrodes"
R. N. Viswanath, **Anil K. Behera**, C. Lakshmanan, T. Mathews
Review (Journal of Electroanalytical Chemistry)

4. "Synthesis and corrosion behavior of nano-porous metallic glass in artificial body fluid for bio-medical application"
C. Poddar, D. Vijayshankar, R. Priya, **Anil K. Behera**, S. Ningshen
Review (Applied Surface Science)

Anil Kumar Behera

Anil Kumar Behera

Dedicated
to my parents
Mr. Muralidhar Behera
and Smt. Sailabala Behera

"A parent's love is whole
no matter how many times divided."
-Robert Breault-

Acknowledgements

It would not have been possible for me to prepare my doctoral thesis without the help of a number of people, who have shaped my ideas and helped in my research.

First and foremost, I would like to thank and express my sincere gratitude to my supervisor, Dr. Tom. Mathews for his guidance and patience throughout the course of present dissertation. I immensely thank him for the stimulating discussions, constructive criticisms and friendly discussions.

I express with great pleasure my deep sense of appreciation and gratitude to my research coordinator Dr. R. N. Viswanath for initiating me into this fascinating, cutting-edge research project. I thank him for his systematic guidance, constant encouragement, and patience. I have learnt, grown and gained invaluable research experience from him.

I am extremely indebted to my Doctoral committee members, Dr. M. Kamruddin, Dr. K. I. Gnanasekar, Dr. Arup Dasgupta, and Dr. T. R. Ravindran. Their insightful comments and constructive criticism have directed my thesis in a proper manner.

I gratefully acknowledge financial support given by Department of Atomic Energy, India. I would like to thank the present director of Indira Gandhi Centre for Atomic Research, Dr. A. K. Bhaduri and the former directors Dr. S. A. V. Satyamurthy and Dr. P. R. Vasudeva Rao for providing timely sanctions/approvals whenever necessary.

I would like to express my deep gratitude to the Director of Materials Science Group, Dr. Shaju K. Albert and the former directors Dr. G. Amarendra, Shri. M. P. Janawadkar, MSG for providing a conducive atmosphere during my entire research tenure.

I would like to thank Dean, Physical Sciences, Dr. R. Rajaraman and the former deans Dr. N. V. Chandra Shekar and Dr. B. V. R. Tata for their support. I would also like to thank Dr. Vidya Sundararajan**,** Dr. Lakshmi Narasimman and Dr. M. Saibaba for their support and the wonderful hospitality during my stay at JRF Enclave.

I do not have words to render thanks to my senior Dr. C. Lakshmanan, for his immense love and support till this day. I also deeply express my heart-felt thanks Dr. Manovah David for continuous encouragement and careful review of my thesis. I am thankful to my seniors Dr. Preethi L.K., Dr. Rajani P Antony, Dr. Madhusmita Sahoo, Dr. R. Mohandoss for the support and scientific discussions.

I would like to thank my collaborators, Dr. P. K. Ajikumar, Dr. S. R. Polaki, Dr. S. Amirthapandian, Dr. K. K. Madapu, Dr. Neha Sharma, Dr. S. Tripura Sundari, Dr. Arun K. Prasad, Ms. Reshma P R, Dr. R. M. Sarguna, Dr. S. Ilango, Mrs. Sunitha and Mrs. Sruthi Mohan for experimental measurements and faithful scientific discussion.

I also thank all my section members, division members and division head Dr. Sandip Dhara, all the MSG members, all the friends in JRF enclave and all my well-wishers.

I wish to thank my seniors Dr. Mahendran , Dr. Bonu, Dr. Avinash, Dr. Devidas, Dr. Subrata, Dr. Sivadasan, Dr. Raghavendran, Dr. Santosh, Dr. Madhusmita, Dr. Padmalochan, Dr. Nilakantha, Dr. Manoj, friends Santanu, Pradosh, Harimohan, Biswa, Arpita, Sithara, Alaka, Balasaritha, Shardha, Podar, Anuj, Thiru, Sivakumar, Sitakanta, Binaya, Bijaya, Suvendu, Gopi, Alok, Dilip, Prasant, Bala, Dhillipan, Darpan and juniors Jeevaraj, Sekhar, Paban, Avinash, Prabhu, Kesav, Pragyna, Jagyaseni, Sindhuja, Gayatri and Mohasin for giving unforgettable moments at IGCAR and for the entire fun that we had together.

No words can suffice to thank my dear family for their patience, understanding and love. I owe highest gratitude and thanks to my dear parents Mr. Muralidhar Behera & Smt. Sailabala Behera for their unsurpassed sacrifice, unconditional love & belief in every stage of my life. My heartiest thanks to my grandparents (Late), sisters, brother and sister in- law for all their good wishes and affection. Special thanks to my niece Shaisha.

Last but not least, I would like to place my deep sense of respect and reverence to all of my teachers who has inspired, motivated, encouraged and educated me.

Table of contents

Chapter 5 Application of MACE fabricated Si nano-architectures for gas sensor and energy storage devices.......................................99

List of Figures

List of tables

Chapter 6

Conclusion and future prospects

This chapter summarizes the important results and conclusive remarks of the present thesis work. In addition to this, a few future directions are also suggested.

6.1. Conclusion

The present thesis reports the successful fabrication of vertically aligned single crystalline Si nanowalls (SiNWs) atop the Si wafer by 2-step metal assisted chemical etching (MACE). The influence of etching parameters viz. etching time and H_2O_2 concentration, on the morphology were investigated, which reveals that higher etching parameter leads to agglomeration of nanowalls. The lightly doped porous SiNWs were successfully fabricated by the modified MACE (i.e MACE combined with anodic polarization etching). The SiNWs fabricated with low etching time exhibits the dual behaviour of excellent antireflectivity and near-superhydrophobicty which can be utilized for enhancing the efficiency and life time of optoelectronic devices like Si solar cells. The lightly doped porous SiNWs shows visible photoluminescence which reveal that MACE combined with anodic polarization etching is capable of producing visible light emitting porous SiNWs. The H_2 sensing performance was carried out on the pristine SiNWs and SiNWs functionalized with Pt and Pd by fluoride-free galvanic displacement deposition. Pt/Pd functionalized SiNWs exhibit enhanced sensing behaviour compared to pristine SiNWs, with Pt and Pd showing better performance at low and high temperature respectively. Since the fabrication and functionalization of SiNWs are achieved by a facile, low cost and CMOS compatible technique, the present study opens room for scaling-up the process to fabricate employable hydrogen sensors. The electrochemical performance of the fabricated SiNWs are also investigated in the electrolyte, tetraethylammonium tetrafluroborate (NEt_4BF_4) in propylene carbonate, where the cyclic voltammetry and galvanostatic charge-discharge studies reveal that SiNWs exhibit redox peaks in low and high potential regions. The origin of the redox peaks is proposed. Although, the present fabricated SiNWs shows lower capacitance than VLS grown Si nanowires/nanotrees, the present study is the first report on the electrochemical studies of the MACE fabricated SiNWs in the present organic electrolyte. The reason behind the low capacitance behaviour and its improvement are suggested. Since, MACE is simple, low cost and CMOS compatible, the presents study suggests its direct utilization in existing established silicon microelectronic industry for the fabrication of silicon nanostructure based electrochemical capacitors.

6.2. Future prospects

Based on the study carried out in the present thesis, the scope for future can be summarized below,

- ☐ Other low cost metals such as copper, nickel can be investigated to be used for MACE to further reduce the cost.
- ☐ MACE technique can be tested for fabrication of polycrystalline Si nano-architectures to further reduce the cost.
- ☐ Optoelectronic devices like solar cells or photodetectors can be made, to test the performance of the fabricated SiNWs as an effective antireflection layer.
- ☐ Other nano-architectures can be synthesized and studied to enhance the contact angle above 160º for better self-cleaning behaviour.
- ☐ The FDTD simulation studies can be undertaken on agglomerated SiNWs to get the insight about its effect on the antireflection behaviour
- ☐ The agglomeration occurring at higher etching time needs to investigated in detail and the process or remedy to avoid the agglomeration has to be found.

- The modified MACE (combination of MACE and anodic polarization etching) can be studied in more details by varying other etching parameter such as HF concentration, current density and its influence on luminescence behaviour can be explored.
- The fluoride-free galvanic displacement deposition can be studied in detail by varying the process parameters to produce well decorated metal particles to be used for sensor application.
- The SiNWs has to be prepared with the suggested factors to enhance the electrochemical capacitor performance.

Abstract

Silicon (Si) occupies the leading position in electronics and photovoltaics industries. However, its indirect band gap limits its application in the field of optoelectronics. A possible solution to this is nanostructuring of Si, where the phenomenon of quantum confinement leads to increase in emission and absorption. In addition, Si nanostructures exhibit extremely low reflectance and therefore is anticipated to be efficient towards applications in optoelectronics. The potential of Si nanostructures for a suitable application rely on its controllable fabrication. Among the various synthesis techniques, metal assisted chemical etching (MACE) has received much interest owing to its simplicity, cost-effectiveness and versatility. Si nano-architectures prepared using MACE technique has shown excellent antireflection, surface hydrophobicity / superhydrophobicity and visible photoluminescence (PL). In addition, the nano-architectures find application in gas sensors and energy storage devices. However, studies on the synthesis of Si nano-architectures using MACE technique, their properties and applications are lacking, and needs to be investigated in details which forms the basis for the present study.

Nonporous and porous Si nanowalls (SiNWs) were fabricated on lightly doped Si wafers by 2-step MACE and modified MACE processes respectively. In the first step, an interconnected Ag nano-cluster network with uniform separation is achieved using the cost effective galvanic displacement deposition technique and network formation mechanism behind the same is explored. The Si wafer covered with the interconnected Ag nano-cluster network is then etched in HF/H_2O_2 solution and the influence of the etching parameters (etching time and H_2O_2 concentration) on the morphology is investigated. The high resolution transmission electron microscopy (HRTEM) and grazing incidence X-ray diffraction (GIXRD) studies revealed that the Si nanowalls are single crystalline and (100) oriented. It was also confirmed from HRTEM studies that the nanowalls are of smooth

surface and covered with a thin amorphous layer. The attenuated total reflectance-Fourier transform infrared spectroscopy (ATR-FTIR) and Raman spectroscopic studies revealed that the amorphous layer consist mostly of Si-O-Si bonded structures. Porous SiNWs were fabricated by combing MACE with anodic polarization etching (i.e by applying a constant current to the Si wafer during etching). The scanning electron microscopy and transmission electron microscopy studies confirmed the formation of porous SiNWs.

The microstructure of the MACE fabricated Si nano-architectures was correlated with its antireflection, wetting and PL properties. The nonporous Si nanowalls carved on the Si wafer exhibited remarkable reduction in reflectance compared to that of planar Si wafer, in the wide wavelength range (230-1200 nm). The low reflectance is explained using finite-difference time-domain (FDTD) simulation. A possible mechanism based on the agglomeration of SiNWs and slight tapering at the top region of SiNWs was suggested to explain the reflectance observed at high etching time. The wetting properties of SiNWs synthesized at different etching times were also studied. It is observed that the SiNWs etched for one minute exhibits a high water wetting contact angle (WCA) of 135° as compared to that of planar Si wafer (67°). As the etching time increases, the contact angle of the SiNWs increased to a maximum of 142°, for SiNWs obtained from 5 minutes etching, and then decreased to 61° for SiNWs obtained at 30 minutes of etching. The wetting behaviour was successfully explained by considering the observed vertical and agglomerated nature of Si nanowalls obtained at low and high etching times respectively. The PL studies carried out on both nonporous and porous SiNWs showed that porous SiNWs exhibit visible PL with peaks at 1.71 and 2.01 eV, whereas the nonporous nanowalls do not show visible PL. In order to find the origin of visible PL, other studies viz. temperature dependent PL, Raman scattering, ATR-FTIR and HRTEM were carried out. The studies confirm that the peaks at 1.71 and 2.01 eV originates from Si quantum structures and Si-O-Si bonded amorphous structures respectively. A qualitative correlation of quantum structure size with the photoluminescence peak energy is carried out.

The MACE fabricated SiNWs were explored for gas sensor and energy storage device applications. On the hydrogen gas sensing front, virgin and Pt & Pd functionalized SiNWs are exploited. The functionalization was achieved by the novel fluoride-free galvanic displacement deposition technique. Both Pt and Pd loaded SiNWs exhibited enhanced sensor performance compared to pristine SiNWs. The temperature dependent sensing studies manifest that Pt functionalized Si nanowalls display superior sensing behaviour at low temperatures (50 - 100ºC) in comparison to Pd functionalized Si nanowalls and vice versa at high temperature (150 - 200ºC). A parallel resistance model bearing the effect of electronic and chemical sensitization was used to elucidate the observed sensing behaviour. For energy storage devices, the SiNWs are explored for possible application as electrochemical capacitor, using the organic electrolyte tetraethylammonium tetrafluoroborate (NEt_4BF_4) in propylene carbonate. The cyclic voltammetry and galvanostatic charge-discharge studies revealed that the SiNWs exhibit redox peaks in low and high potential regions. The origin of these peaks are attributed to the silver related deep level trap state in silicon in contact with adsorbed water and from the oxidation of silicon and its hydrides by the moisture present in the electrolyte, respectively.

Chapter 1

Introduction

The chapter provides a brief introduction on silicon (Si), summarizing its importance, structure, bandgap and limitations followed by remedy through nanostructuring of Si, for various applications. The subsequent section briefly discus the different techniques for the fabrication of Si nanostructures with a special attention to metal assisted chemical etching (MACE) owing to its merits over other techniques. Some exciting properties of the Si nanostructures fabricated by MACE are also described. Finally, selected applications of the MACE fabricated Si nanostructures are discussed, followed by a statement highlighting the objective of the present thesis.

1.1. A brief introduction on silicon

Silicon (Si), is the prime material in electronics and photovoltaics industries and has been the foundation of knowledge based civilization [1-4].The leading position of Si trails from its inimitable amalgamation of beneficial features viz. high natural abundance (second most abundant element on earth's crust), high stability, non-toxicity, tunable electrical properties and availability of large single crystals. These features are at the origin of the electronic industry to follow Moore's law for the past half a century and have made possible to establish the Si technology to its present maturity. In addition, its optimum bandgap (1.12 eV) for capturing the solar spectrum, in case of a single-junction device, has enabled Si to be the ideal material of choice for photovoltaics with a share of around 90% of the solar panels, in the present day solar cell market.

The structure and bandgap of Si are described below,

1.1.1. Structures

Silicon is a group IV element and has a diamond crystal structure. Unit cell of the diamond structure is described in Fig. 1.1 a) [5]. The diamond lattice can be understood by considering the tetrahedral structure shown in Fig. 1.1 b). This structure is basically a body-centered cubic with four of the corner atoms missing. Every atom in the tetrahedral structure has four nearest neighbors and it is the basic building block of the diamond lattice. Si atom possess fourteen electrons. In the ground state, they are arranged in the electron configuration [Ne]$3s^2 3p^2$. Of these, four are valance electrons, occupying the 3s orbital and two 3p orbitals. Hence, it can complete its octet to obtain the stable noble gas configuration of argon by forming tetrahedral sp^3 hybrid orbitals. The hybrid sp^3 orbitals of central Si atom share its electron with four other Si atoms.

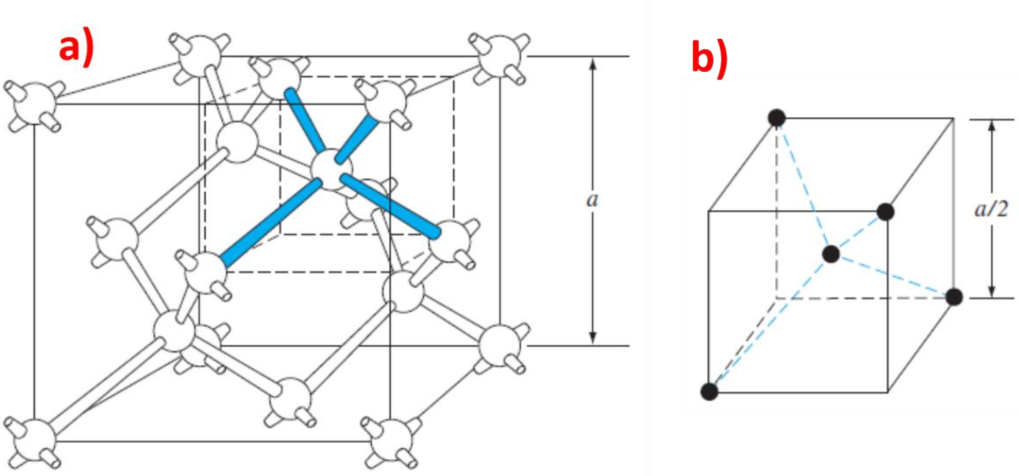

Figure 1.1 a) The diamond structure. b) The tetrahedral structure of closest neighbours in the diamond lattice [5].

1.1.2. Bandgap

Silicon has bandgap of 1.12 eV. The bandgap is indirect in nature, which means that the energy minimum of conduction band and energy maximum of valance band do not fall at the same wave vector. This is described in Fig. 1.2. The energy band diagram of Si is compared with GaAs, a direct bandgap material for clear understanding [4].

In a steady state, electrons (blue circles) occupy the lowest energy states of the conduction band while holes (red circles) occupy the upper states of the valence band. When electron and hole recombine radiatively, emission of photon takes place. This means the electron in the conduction band drops down to the empty states of a hole in the valance band. The process of recombination is given in equation 1.1.

$$\hbar\omega = E_C - E_V \cong E_g \tag{1.1}$$

Where, $\hbar\omega$ is the energy of photon, E_C is the minimum energy of conduction band, E_V is the maximum energy of valance band and E_g is the bandgap energy of the semiconductor. Besides energy, momentum is also conserved during the process. Notably,

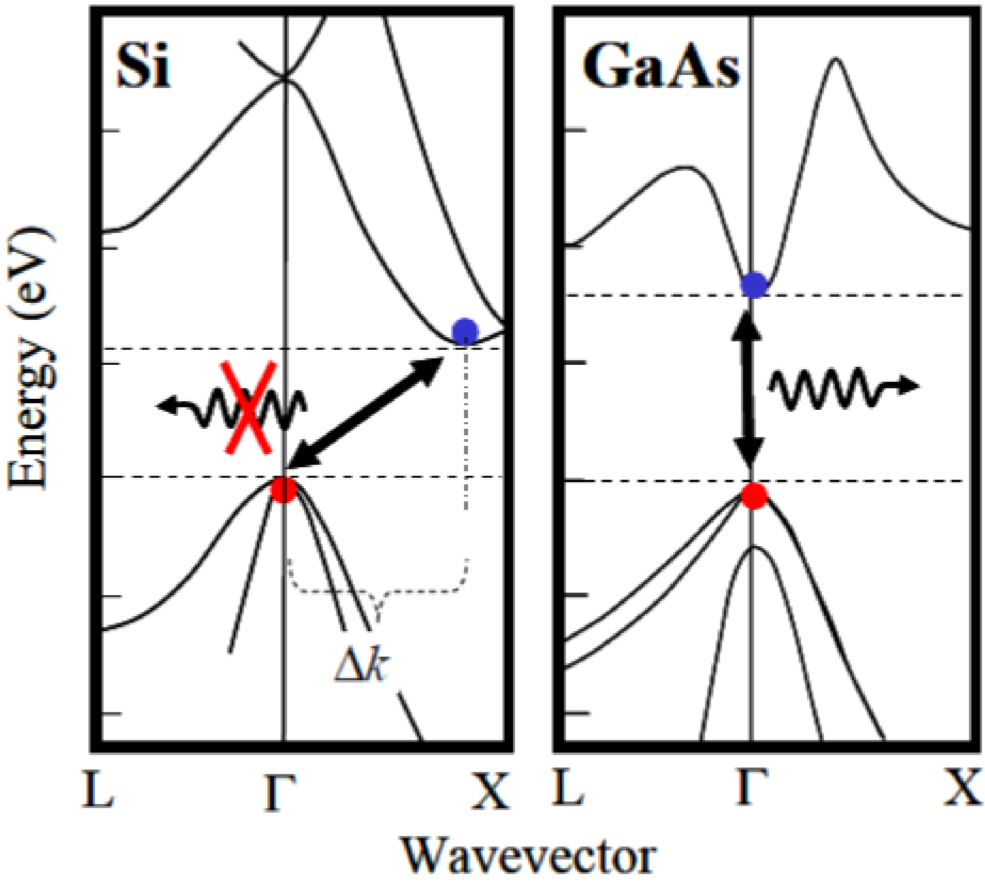

Figure 1.2 Energy-band diagrams for Si and GaAs. The dispersion curves are along the [100] direction (X-point) and the [111] direction (L-point). Conduction electrons (blue circles) occupy the band's minimum and valence holes (red circles) occupy the band's maximum with Δk being the wavevector's difference for Si. Photon emission is not allowed for Si [4].

the wavelength of photon ($\lambda = 2\pi/k \sim 1\mu\text{m}$ for Si) is about three orders of magnitude larger than the de-Broglie wavelength of the electrons (is of the order of the lattice constant in semiconductors ~5Å). Therefore, the photon momentum can be neglected compared to that of electrons and holes. For direct bandgap semiconductors like GaAs, both the electrons and the holes possess the same momentum at the center of the Brillouin zone (Γ-point in Fig. 1.2). Consequently, vertical radiative recombination can take place. However, in Si, the large momentum mismatch between electrons and holes does not allow direct radiative recombination. The recombination process in Si involves another entity; a phonon is required to satisfy the momentum conservation.

1.1.3. Limitation of Si and remedy

However, the application of Si has been significantly limited in the field of optoelectronics because of its indirect bandgap. As described above, the indirect transition requires the participation of phonons to satisfy momentum conservation. The additional participation hinders efficient emission and absorption of radiation [1, 4, 6-9]. Therefore, in order to extend the functionality of Si technology from microelectronics to optoelectronics, the poor optical properties of Si need to be addressed. One of the possible solutions to improve this physical inability is to reduce the size of Si to nanometer regime, where the phenomenon of quantum confinement becomes prominent. In the domain of quantum confinement, the carriers are localized in the small nanometer volume which causes increase in uncertainty of carrier momentum, according to Heisenberg uncertainty principle [10],

$$\Delta x \, \Delta p_x \geq \frac{\hbar}{2} \tag{1.2}$$

Where, Δx, Δp_x and $\hbar$ denote the uncertainty in position, uncertainty in momentum and Planck constant divided by 2π, respectively. According to equation (1.2), if the uncertainty in position is low (as carrier confined in a quantum structure) then the uncertainty in momentum is high. So, the probability of fulfilling the momentum conservation condition is much higher. Moreover, following Fermi’s golden rule for transition probability, when electron-hole pairs are localized spatially in small nanometer volume, their wave functions overlap more in position space, and that leads to enhancement in oscillator strength for more recombination. In addition, the Si nanostructure array shows extremely low reflectance in contrast to the high natural reflectance (>35%) of Si in the wide wavelength range [11, 12]. This can increase the absorption and hence the efficiency of optoelectronic devices like solar cells and photo-detectors. These prospects suggest that Si nanostructures can address the aforementioned issues of bulk Si and open up opportunity for Si to be an efficient material in the field of optoelectronics. Moreover, as the dimension is reduced to the nanoscale regime, the surface to volume ratio is greatly increased. As a result, Si nanostructures exhibit superior selected physical and chemical properties compared to its bulk counterpart [13]. Therefore, Si nanostructures in its various forms like nanopyramids, nanowires, nanotubes, nanowalls, nanostructured thin films, nanopores etc., have been explored for potential applications in diverse fields, such as nanoscale electronics [14], thermoelectric [15], field emission [16], terahertz emission [17], energy conversion [18-20], energy storage [21-24], as well as chemical and bio-sensors [25-30].

1.2. Different techniques for fabrication of Si nanostructures

The potential of Si nano-architectures for a suitable application rely on its controllable fabrication. Numerous techniques utilizing the bottom-up approach such as vapor-liquid-solid (VLS) growth, molecular beam epitaxy, laser ablation etc. and the top-down approach such as reactive ion etching, laser-induced etching, electrochemical etching (or anodic polarization etching), metal assisted chemical etching (MACE) etc. [17, 29] have been developed with the aim to control different synthesis parameters for the fabrication of desirable Si nanostructures. Some of the techniques are briefly described below.

1.2.1. Vapor-liquid-solid (VLS) growth

Vapor-liquid-solid (VLS) technique is a one dimensional nanostructure growth technique. It can be used to produce nanostructures like nanowires, whiskers, nanorods.

Wagner and Ellis were the first to describe the VLS technique for growing wires [31]. The VLS method for growing Si nanowires is illustrated schematically in Fig. 1.3. In this growth process, Si gas precursors such as SiH_4, and $SiHCl_3$ are collected at the metal catalyst. This assists in lowering the dissociation energy of gaseous molecules. Gold (Au) is the commonly used catalyst. According to the phase diagram, in presence of sufficient Si, the Au-Si alloy becomes liquid above the eutectic point of 363ºC. During the continuous flow of precursor gas, additional Si atoms are collected into the Au-Si liquid alloy. At a certain point the metal alloy becomes supersaturated, then Si will precipitate at the interface between the particle and the substrate, leading to the growth of solid Si wires [32]. Substrate versatility is one of the advantages of VLS method. But it has a limitation, owing to the poor control on nanowire orientations. Generally, the direction of growth in this technique and hence the axis of the wires, is along either <111> or <110> direction [33]. Moreover, VLS being a high temperature process, there can be metal contamination in Si nanowires which creates issue related to its complementary metal-oxide-semiconductor (CMOS) compatibility.

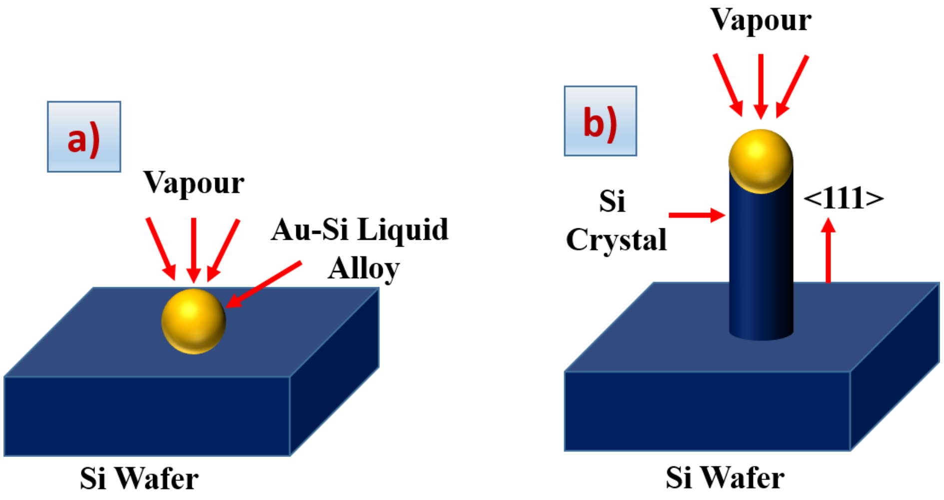

Figure 1.3 Schematic diagram depicting Si wire growth through the Vapor-Liquid-Solid (VLS) method. a) Initial formation of a liquid alloy droplet from a solid Au particle on the substrate. b) Growth of wire with the liquid droplet at the tip.

1.2.2. Reactive ion etching (RIE)

Reactive ion etching (RIE) of Si utilizing halogen radicals is used for Si micromachining [19]. Highly anisotropic etching is accomplished by mixing some components to the etching gas which creates a passivation layer over Si. Jansen et al. [34] were the first to investigate the anisotropic RIE using a mixture of SF_6 and O_2 gas . In the plasma, the two molecule species are broken along with the production of F*- and O*-radicals, respectively as shown in Fig.1.4 [19]. The F* will attack the Si surface and form volatile SiF_4. On the other hand, the O* reacts with SiF_4 forming silicon-oxyfluoride (SiO_xF_y) at cryogenic temperature. SiO_xF_y works as passivation layer serving as an etch stop for F*. The passivation layer is etched on horizontal faces because of ion bombardment from plasma. But the removal of the passivation layer in vertical faces is lesser because of the directionality of the plasma ions. So the sidewalls are escaped from the etching by F*. Therefore, the overall process becomes anisotropic. In this regime precipitates from the gas phase can result to form random nanostructures. Micro-masking by those particles results in the formation of silicon needles [34]. Moreover, the random formation of micromask occurs during the plasma process, which some researchers have used to prepare tailored micromask using silica [35] or silicon-oxybromide [36] nanoparticle. However, dry etching has limitation in producing high aspect ratio nanostructures with smooth surface. In addition to it, it is a cost intensive and complex process. It is also time consuming where one wafer at a time can be etched [32].

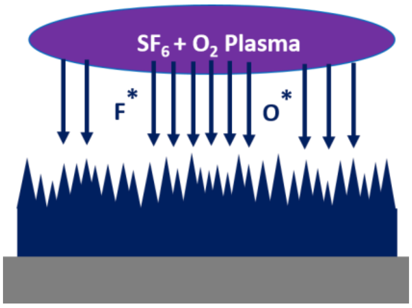

Figure 1.4 Depicts the inductive coupled plasma reactive ion etching (RIE) process in an atmosphere of SF_6 and O_2.

1.2.3. Electrochemical (anodic polarization) etching

This method is generally used for the preparation of porous Si. In this process, the etching of Si in HF solution is carried out through anodization via external power supply. Fig. 1.5 shows the schematic of the two electrode electrochemical etching process. In this process Si is used as working electrode (anode) and platinum is generally used as counter electrode (cathode). The two half-cell reaction of the electrochemical cell are summarized as below [37],

$$\text{At cathode: } 2H^{+}+2e^{-}\rightarrow H_2 \qquad (1.3)$$

$$\text{At anode: } Si + 6F^{-}+2H^{+}\rightarrow SiF_6^{2-}+H_2+2^{-} \qquad (1.4)$$

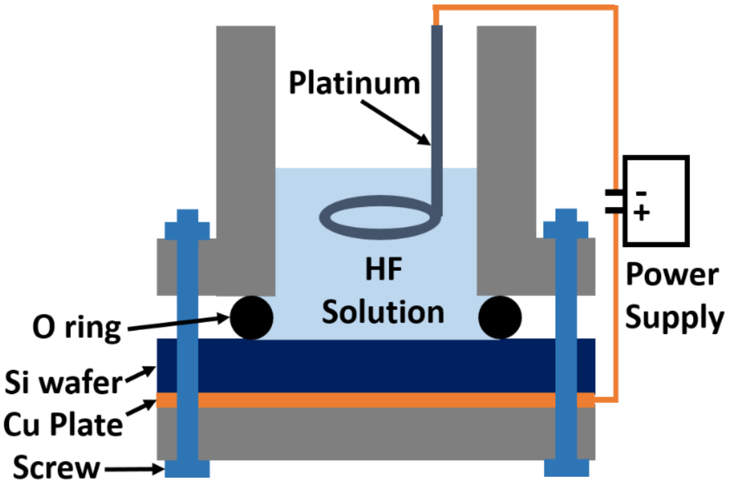

Figure 1.5 Schematic illustration of a two - electrode electrochemical cell for fabrication porous Si.

1.2.4. Metal assisted chemical etching (MACE)

Metal assisted chemical etching (MACE) is a novel technique to fabricate various Si nanostructures. Since the technique has been used in the present study it is explained in detail. MACE was first discovered in 1997 by Dimova-Malinovska et al. [38], when they produced porous Si by etching aluminum (Al) deposited Si substrate in a solution composed of HF, HNO_3 and H_2O. They reported no “incubation period” to the onset of etching. MACE was further investigated in detail by Li and Bohn [39]. The research group found that a thin layer of noble metal (e.g., Au, Pt, or Au/Pd alloy) sputtered on the surface of Si substrate catalyzed the etching process in a mixed solution containing HF, H_2O_2 and ethanol. This systematic etching resulted in straight pores or columnar structures. Peng et al. [40] further developed MACE for producing Si nanowires. Generally, in MACE procedure, the Si substrate partly covered with a noble metal is exposed to an etchant comprising HF and an oxidizing agent. The Si underneath the noble metal is etched much faster than the Si surface without noble metal coverage. As a consequence, the noble metal sinks into the Si substrate, creating pores and or wires. The geometry of the produced Si structures depends on the original morphology of the noble metal coverage [41].

MACE is distinct and promising owing to the following benefits [32, 41-43]:

- MACE is simple, cost-effective and versatile. Also it has the ability to produce different kinds of nanostructures such as nanopores, nanowires, nanowalls and porous nanowires.
- MACE has the potential to control different parameters like cross-sectional shape, diameter, length, orientation and doping.
- MACE is a room temperature method which is CMOS compatible. This means it can be easily integrated into the standard chip manufacturing process.

MACE generally comprises of two successive processes viz. surface nucleation of metal catalysts and anisotropic etching. Depending on the occurrence of these two processes, it is categorized into two types: one-step MACE and two-step MACE [44]. In one-step MACE, the two successive processes occur in the etching solution comprising HF and suitable metal salt (e.g. $AgNO_3$, $KAuCl_4$ etc.) as shown in Fig. 1.6 a) [44-46]. Whereas, in two-step MACE, first step is the deposition of metal catalyst and the second step is etching in the solution consisting of HF and a suitable oxidizing agent (H_2O_2, $Fe(NO_3)_3$, aerated O_2

etc.), as depicted in Fig. 1.6 b) [47-50]. Since, metal catalysts are deposited separately in two-step MACE, it has an advantage, over one-step MACE, in terms of independent control over metal morphology, thereby deciding the shape of the Si nanostructures to be prepared. For example, ordered arrays of nanowires, nanofins and nanopores have been fabricated using two-step MACE with the proper patterning of the catalytic metal on Si substrate [50-55]. However, patterning of these metals were achieved by using various lithography techniques like colloidal (or nanosphere) lithography, soft lithography, laser interference lithography, substrate conformal imprint lithography and deep ultraviolet lithography, which are complex and cost intensive. The alternative way for metal catalyst deposition is done by using vacuum techniques (thermal evaporation, electron beam evaporation and sputtering) which are energy and cost intensive. The electroless metal deposition techniques, though patterning of metal morphology is difficult [56], possesses the benefits such as being simple, versatile, cost effective and allows the whole process to be carried out in the chemical lab. Therefore, several researchers have utilized electroless deposition of catalytic metals (mostly Ag and Au) as the first step of MACE towards the synthesis of Si nanostructures. Using this technique they have fabricated different nanostructures and studied various properties and related applications of the fabricated nanostructures [6, 57, 58]. However, studies on the effect of deposition parameters over the morphology of metal catalyst and its formation mechanism that helps in producing desired Si nanostructures are still lacking. In two-step MACE, the variation of etching parameters like etching time, HF concentration and oxidant concentration (mostly H_2O_2 is used) have been carried out in order to understand the underlying etching mechanism. However, to fully comprehend the influence of etching parameters on the morphology of Si nanostructures [6, 59-71], several studies are still required.

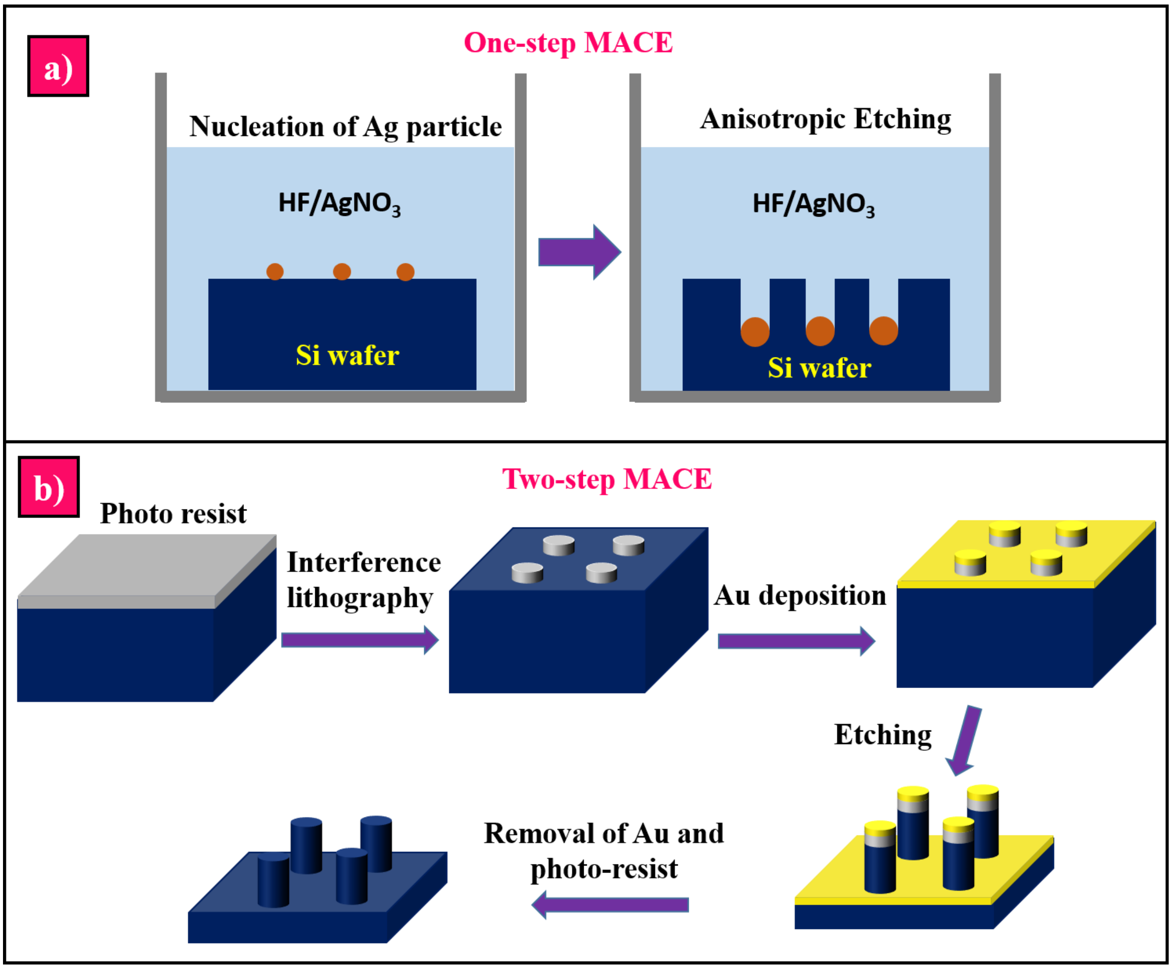

Figure 1.6 Schematic of a) one-step and b) two-step MACE .

The porous Si nanostructures (like porous nanowires / nanowalls) are new kind of nano-architectures which combine both the physical features of nanowires / nanowalls and porous characteristics. The unique combination is expected to open novel avenues for Si-based optoelectronic and photo-electrochemical devices [6, 60]. As mentioned previously, MACE is capable of producing porous Si nanostructures. The porous Si nanostructures exhibit visible photoluminescence [6, 72, 73]. But, Si nanostructures with high porosity can only be fabricated from highly doped Si wafer using MACE [60, 73, 74]. However, high doping concentration can cause spectral red shift and reduction in quantum yield of visible luminescence. Also, heavy doping can cause serious carrier recombination that leads to reduction in the solar cell efficiency [75]. Therefore, it is exciting to fabricate lightly doped porous Si nano-architectures using MACE for its wide range of potential application.

1.3. Some exciting properties of MACE fabricated Si nanostructures

Beside the ease in fabrication, the MACE fabricated Si nanostructures have shown the following exciting properties:

1. Excellent antireflection
2. Surface hydrophobicity/superhydrophobicity
3. Visible photoluminescence

1.3.1. Excellent antireflection

Several research on Si nanostructures prepared by MACE [12, 76-80] display excellent antireflection behaviour. Srivastava et al.[76], performed a detailed study on the antireflection behaviour of Si nanowires prepared by MACE. They have investigated the effect of etching time (or wire length: since wire length linearly varies with etching time) on the antireflection behaviour. The reflectance (reflectivity) spectra of Si nanowires as well as polished Si wafer (0 min etching time) as a function of wavelength (λ) are shown in Fig. 1.7 [76]. They observed a decrease in reflectivity with an increase in etching time (i.e. with increasing wire length). Moreover, reflectivity shows a minimum of ~1.5% in the 300–600 nm range and <4% in the spectral range 600–1000 nm in the samples etched for 15 min or more. The optical photographs of the Si nanowire arrays fabricated for 45 min and polished Si wafer are shown in the inset of Fig. 1.7, where the appearance of black colour reveals the antireflection behaviour. They also observed that there is no significant reduction in reflectance in case of samples selected for more than 25 min, as depicted in Fig. 1.8, where the reflectivity at 600 nm wavelengths is plotted against etching time.

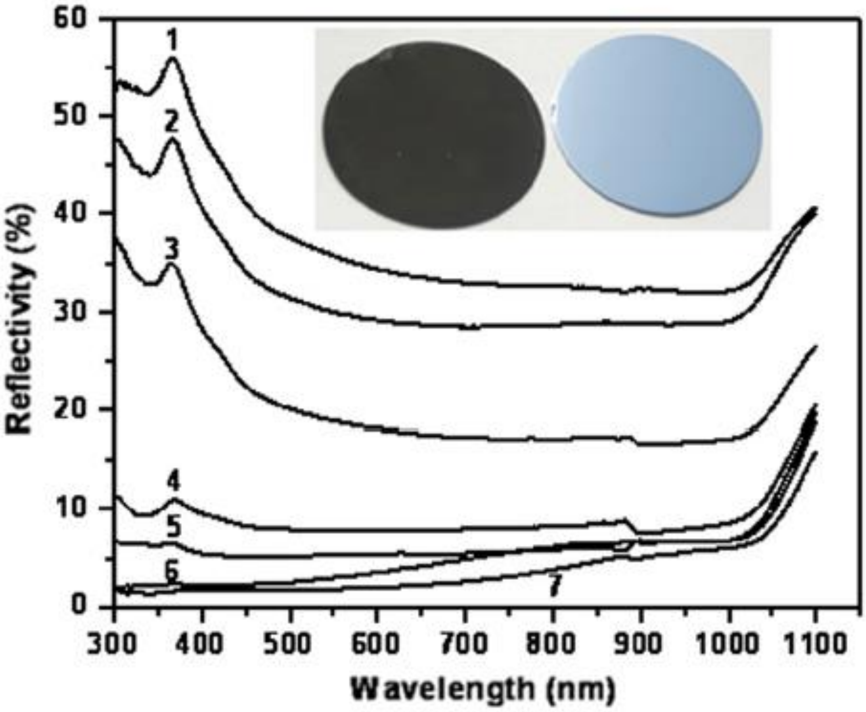

Figure 1.7 Reflectivity as function of wavelength (λ). The spectra denoted as 1, 2, 3, 4, 5, 6 and 7 represent samples obtained for etching time of 0, 1, 1.5, 2, 5, 15 and 45 min, respectively. The sample obtained for 0 minute etching time denotes the polished Si wafer. Inset displays the optical photograph of Si nanowires obtained for etching time of 45 min and polished Si wafer [76].

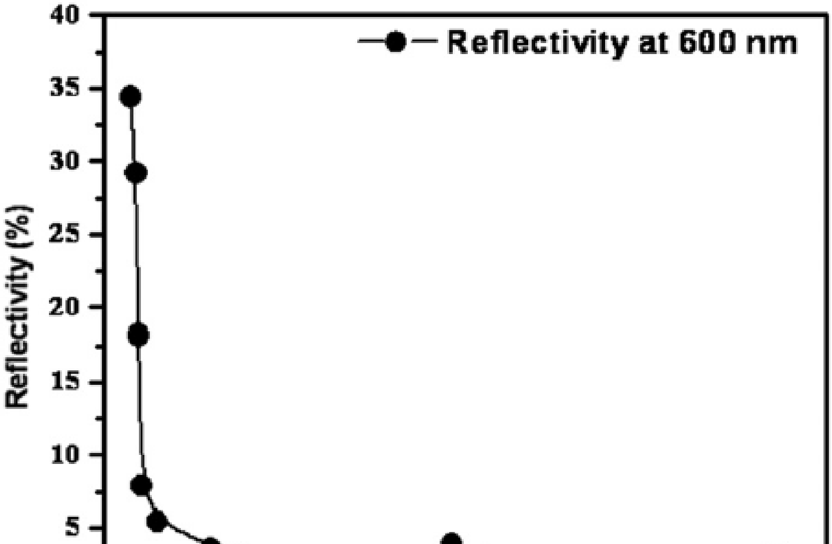

Figure 1.8 Reflectivity of Si nanowires at 600 nm wavelength with increasing etching time [76] .

1.3.2. Surface hydrophobicity/superhydrophobicity

Several studies have shown that Si nanostructure fabricated by MACE exhibit surface hydrophobicity/superhydrophobicity [81-84]. Lee et al. [81], fabricated rough silicon surfaces with micro and nanostructures by copper (Cu)-assisted chemical etching process. The report indicates that the as-prepared hierarchically rough silicon surfaces exhibit hydrophobic behaviour with a contact angle value ranging from 93° to 149° depending on the size of Cu nanoparticle. Moreover, they modified the hierarchically rough silicon surfaces by spin-coating a thin layer of Teflon film and achieved superhydrophobic behaviour with extremely high contact angle of ~ 180°. Figure 1.9 a) and b) and their insets display respectively the SEM micrographs and water contact angle of as-prepared hierarchical rough Si surface generated with Cu nanoparticles of 30 nm size and hierarchically surface generated with Cu nanoparticles of 30 nm size modified by 3 wt% Teflon precursor solutions.

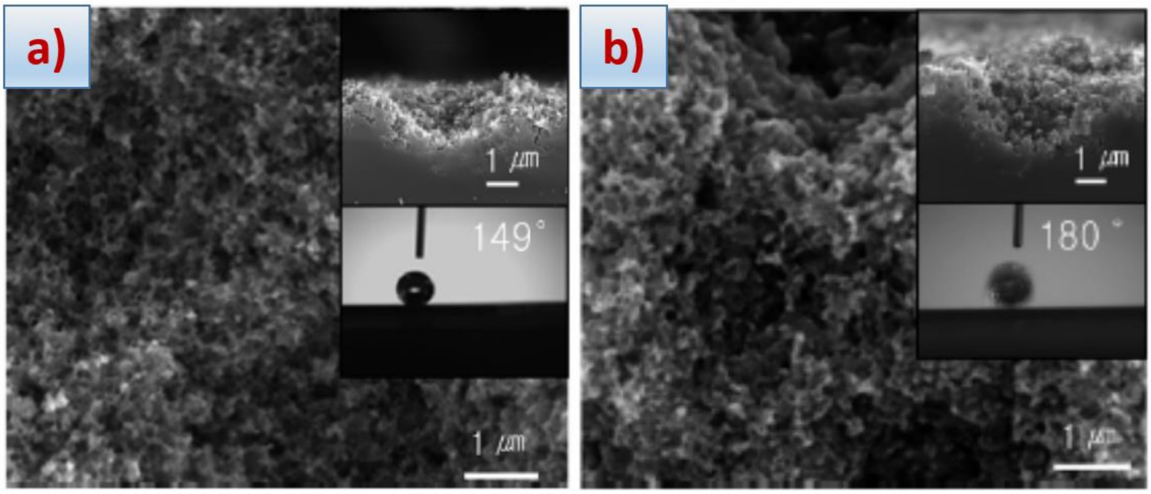

Figure 1.9 a) SEM micrographs of MACE generated hierarchically rough Si surfaces with Cu nanoparticles of 30 nm. b) SEM micrograph of MACE generated hierarchically rough Si surfaces with Cu nanoparticles of 30 nm modified by Teflon precursor solutions of 3wt%. Inset images display the respective cross-sectional SEM micrographs and water contact angles [81].

However, the reports showing the combined behaviour of excellent antireflection and hydrophobicity, which is beneficial for enhancing the efficiency as well as life time (due to self-cleaning nature of hydrophobicity /superhydrophobicity) of optoelectronic devices like solar cell and photodetectors are very rare. Table 1.1 depicts some list of articles on the antireflection and hydrophobic behaviour of Si nanostructure fabricated by metal (silver) assisted chemical etching.

Table 1.1 Antireflection and hydrophobic behaviour of Si nanostructure synthesized by metal (silver) assisted chemical etching. Note: contact angle refers to water contact angle, GD refers to galvanic displacement deposition process, R refers to reflectance, R_λ refers to average reflectance and R_{sw} refers to solar-weighted reflectance over the wavelength range indicated in the bracket.

Morphology	**Ag Deposition method**	**Etching solution**	**Reflectance (Wavelength range)**	**Contact Angle**	**Ref.**
Micro- and nanopores	Sputtering followed by annealing at 600°C	HF/H_2O_2	R_λ~4.7% (200-1100 nm)	-	[85]
Porous micro-cavity	$HF/AgNO_3$ (GD)	HF/H_2O_2 acid vapors	R_λ~6% (300-1100 nm)	-	[86]
Nanostructures	Spin coating followed by sintering at 170°C	HF/HNO_3	R_{SW} ~1.96% (300-1100 nm)	~102°	[87]
Nano-pores	$HF/AgNO_3$ (GD)	HF/H_2O_2	$R_\lambda < 4\%$ (400-1000 nm)	-	[12]
Nanoscale texture	Chemical reduction method with PEI as stabilizer.	HF/H_2O_2	R_λ~2.8% (200-1000 nm)	-	[88]
Nanowires	$HF/AgNO_3$ (GD)	HF/H_2O_2	R_λ~5.6% (250-800 nm)	-	[89]
Nanocones	$HF/AgNO_3$ (GD)	HF/H_2O_2 etching. Then ambient oxidation and etching by HF	$R < 3\%$ (400- 800 nm)	117°	[84]
Nanowires	Electron beam evaporation	HF/H_2O_2	R ~2-4% (< 1107)	-	[90]
Graded nanostructure	$HF/AgNO_3$ (GD). Then soaked in %	HF/H_2O_2	R_λ~1.6% (300–900 nm)	-	[79]

	HNO_3 for partial Ag removal				
Nanowires	$HF/AgNO_3$ (GD)	HF/H_2O_2	$R_\lambda \sim 1\%$ (300–1000 nm)	-	[91]
Nanowires	$HF/AgNO_3$ (GD)	HF/H_2O_2	$R < 1\%$ (300–1000 nm)	-	[80]
Tapered nanowires	$HF/AgNO_3$ (GD)	HF/H_2O_2 etching. Then KOH etching	$R_\lambda < 1\%$ (300–1000 nm)	-	[92]
Nanowires	$HF/AgNO_3$ (1-step)		$R_\lambda \sim 1.5\%$ (300-600 nm) and < 4% (600-1000 nm)	-	[76]
Nanopore	$HF/H_2O_2/AgNO_3$ (1-step)		Relative effective $R \sim 0.17\%$ (300–1000 nm)	-	[77]
Porous film	$HF/AgNO_3/IPA$ (1-step)		$R_\lambda \sim 0.5\%$ (300-800 nm)	-	[93]
Nanowires	$HF/AgNO_3$ (1-step)		$R \lesssim 1.4\%$ (300–600 nm)	-	[94]
Nanowires	$HF/AgNO_3$ (1-step)		$R_\lambda \sim 1.49\%$ (200–850 nm)	-	[95]

1.3.3. Visible photoluminescence (PL)

Numerous studies have exhibited visible photoluminescence (PL) of porous Si nanostructures prepared by MACE [6, 8, 44, 72, 73]. For instance, Qu et al. [72] fabricated vertical Si nanowire array through a two-step MACE of highly doped n-type Si (100) wafers. The PL studies of the fabricated Si nanowires are summarized in Fig.1.10. Figure 1.10 a) depict the PL spectrum of porous Si nanowires which shows clearly a broad visible emission centered around 650 nm. Fig. 1.10 b) presents the optical image of a selected single porous Si nanowire. The corresponding confocal PL image is shown in Fig. 1.10 c) which overlaps with the optical microscopy image. This confirms that the PL is indeed originated from the porous Si nanowire.

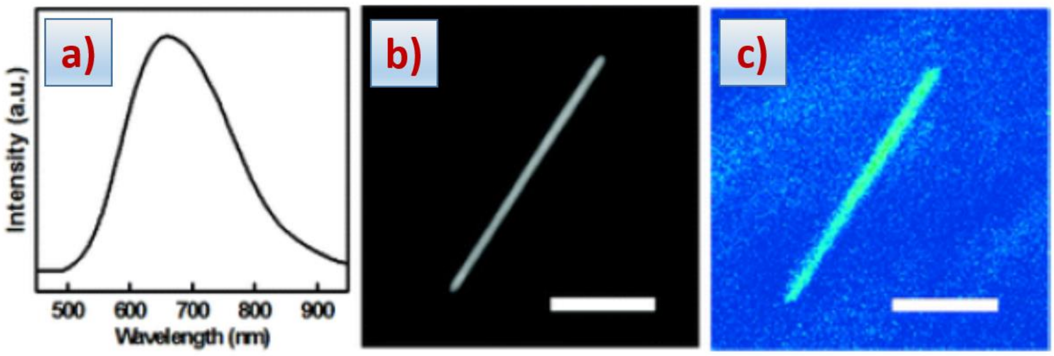

Figure 1.10 a) Photoluminescence spectrum of porous Si nanowires obtained by MACE. b) Optical image of a single porous silicon nanowire. c) Confocal photoluminescence image of the same single porous silicon nanowire. The scale bar in b) and c) is 3 µm [72].

However, as aforementioned, highly porous Si nanostructures are achieved from highly doped base Si wafer. The visible luminescence properties are mostly studied in highly doped porous Si nanostructures where high doping concentration can cause spectral red shift and reduction in quantum yield of visible luminescence. To the best of our knowledge there are no reports on study of visible PL properties of lightly doped porous Si nanostructures prepared by combining MACE with anodic polarization etching. Moreover, the studies correlating the microstructures of the fabricated Si nano-architectures with these properties, which are crucial in view of their favorable applications, are quiet less and needs to be investigated in detail.

1.4. Some applications of MACE fabricated Si nanostructures

Owing to the compatibility of MACE with established CMOS technology, Si nanostructures synthesized by MACE have been studied for the following applications

1. Gas sensors
2. Energy storage devices

1.4.1. Gas sensors

On gas sensing front, the sensing behaviour of MACE fabricated Si nanostructures towards hydrogen (H_2) gas is analyzed owing to its importance in nuclear industry. For H_2 sensing both pristine and functionalized (platinum (Pt) & palladium (Pd)) Si nanostructures have been investigated. Functionalized Si sensors are favorable due to their selectivity for a particular gas against other chemical species [25]. For instance, Gao et al. [25] fabricated a H_2 gas sensor based on a Si nanomesh structure decorated with Pd nanoparticles via polystyrene nanosphere lithography and top-down fabrication processes. The gas sensor shows dramatically improved H_2 gas sensitivity compared to Si thin film sensor without nanopatterns. Furthermore, a buffered oxide etchant (BOE) treatment of the Si nanomesh structure resulted in an additional performance improvement. Fig. 1.11 shows the real time response of the sensor, with BOE treated suspended Si nanomesh channel, to H_2 with concentrations of 50 ppm-0.8%. In general, the functionalization of Si nanostructures with these metals have mostly been achieved by techniques like electron beam evaporation, magnetron sputtering, pulsed laser deposition etc. [23] which are energy and cost intensive. Notably, there are only a few reports on the cost effective galvanic displacement deposition technique [96] to functionalize Si nanostructures for hydrogen sensing. However, the use of HF along with the metal salt solution in this method can alter the initial morphology of the fabricated Si nanostructures. Therefore, it is required to modify the technique, to functionalize the Si nanostructures without disturbing its initial morphology.

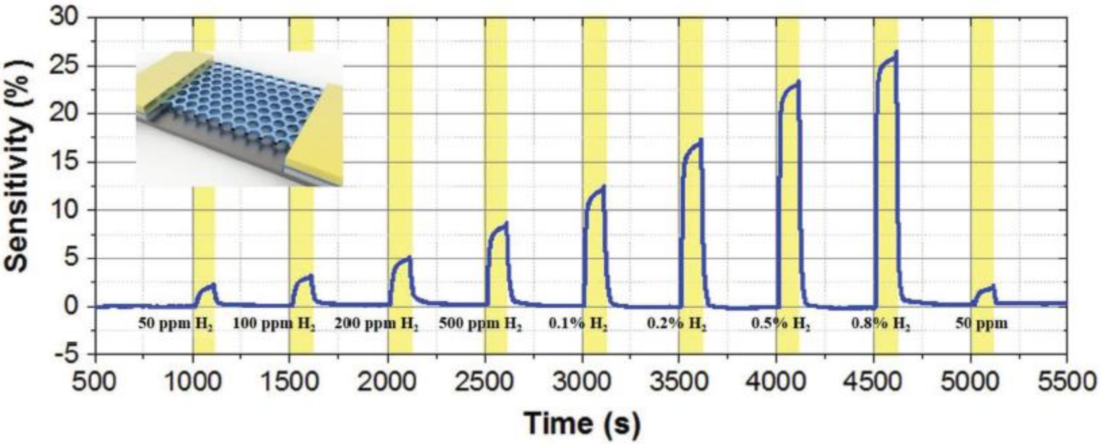

Figure 1.11 Real time response of the sensor with BOE treated suspended Si nanomesh channel to H_2 with concentrations of 50 ppm-0.8% [25].

1.4.2. Energy storage devices

Among the different energy storage devices, electrochemical capacitor has been considered as a prominent energy storage device because of its fast charge / discharge rate, high power density, long cycle-life and safety in operation [97]. For electrochemical capacitor application, the MACE fabricated Si nanostructures are usually coated with other materials, such as silicon carbide, ultrathin carbon sheath, graphene and nickel oxide [22, 98-100], due to the reactivity of Si with the commonly used aqueous electrolytes. But, use of these coated materials can cause compatibility issues with the established CMOS fabrication technology, as well as increase the production cost. Recently, the research group led by S. Sadki have studied silicon nanowires and nanotrees, grown by the vapour-liquid-solid (VLS) technique without any additional coating, for electrochemical capacitor application using different organic and ionic liquid electrolytes [21, 101, 102]. For instance, the growth of Si nanotrees and its electrochemical behaviour studied by the research group led by S. Sadki [102] is shown in Fig 2.1. Fig. 2.1 a) shows the Si nanotrees growth by **c**hemical **v**apour deposition (CVD) via gold catalysis in a three-steps process: growth of trunks and branches are separated by a new gold catalyst deposition. Fig. 2.1 b) shows the SEM micrograph of Si nanowires, i.e. the trunks, with 20-500 nm diameter and 52 μm lengths. Fig. 2.1 c) shows the SEM micrographs of Si nanotrees with 20-500 nm wide and 52 μm long trunks and 1 nm gold thin film as second gold catalyst deposition. As depicted in Fig. 2.1 d), both Si nanowires and Si nanotrees exhibit capacitive behaviour and have higher capacitance than that of bulk. The Si nanotrees shows more capacitance than that of Si nanowires. For Si nanotrees, the electrode capacitance is enhanced up to 900 $\mu F.cm^{-2}$, i.e. 150 fold higher than of bulk Si. However, high cost and issues related to the high temperature VLS growth method limit its application. Therefore, it is exciting to investigate the electrochemical behaviour of the MACE fabricated Si nanostructures in these electrolytes for its application towards electrochemical capacitor.

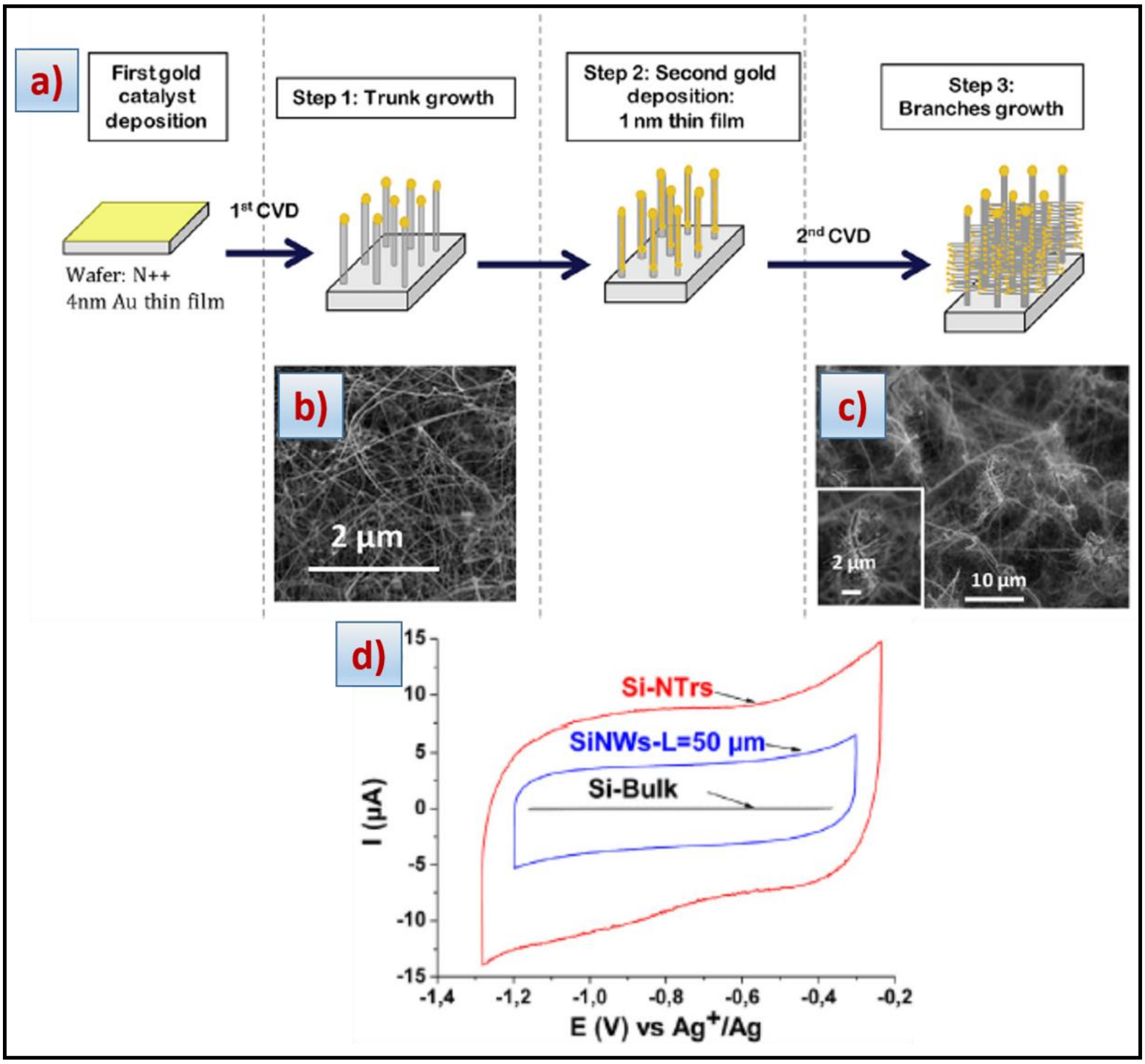

Figure 1.12 Schematic depicting the growth process of Si nanotrees via chemical vapour deposition. a) The process involves three steps: Step 1: Growth of Trunk, Step 2: Deposition of second gold catalyst, Step 3: Growth of branches. b) SEM micrograph of Si nanowires, i.e. the trunks, with 20-500 nm diameter and 52 µm lengths. (c) SEM micrographs of Si nanotrees; 20-500 nm width and 52 µm long trunks and 1 nm gold thin film as second gold catalyst deposition. d) Cyclic voltammetry curves in 1 M tetraethylammonium tetrafluoroborate (NEt_4BF_4) in propylene carbonate at 50 mV.s^{-1} of bulk silicon, 50 µm long Si nanowires, Si nanotrees with 50 µm long trunks and 1 nm gold thin film as second gold catalyst source.

1.5. Objective of the thesis

The key objectives of the thesis are summarized below,

- Synthesis of silicon nano-architectures using two step MACE with cost effective galvanic displacement deposition method for metal (Ag) deposition, optimization of process parameters, understanding the effect of etching parameters in fine tuning the morphology and delineating the mechanism behind the formation of nanostructures.

- Fabrication of lightly doped porous silicon nanowalls / nanowires using modified MACE.
- Investigation of the exciting properties of MACE fabricated Si nanowalls (like antireflection, wetting and photoluminescence) and correlation of its microstructure with these properties.
- The investigation of pristine Si nano-architectures and Si nano-architectures functionalized with Pt and Pd by fluoride-free galvanic displacement technique for hydrogen sensing application. Electrochemical behavior of silicon nano-architectures in the electrolyte, tetraethylammonium tetrafluoroborate (NEt_4BF_4) in propylene carbonate, for electrochemical capacitor application.

Chapter 2

Experimental techniques

The present chapter includes a brief report on the experimental techniques used for the synthesis of smooth and porous Si nanowalls (SiNWs) and their characterizations to investigate the electrochemical, morphological, crystallographic, structural, elemental, and optical properties. Following the electrochemical techniques, the basic principles of electron microscopic techniques (scanning electron microscopy (SEM) and transmission electron microscopy (TEM)) used for the morphological characterization of the fabricated samples are discussed. This is followed by discussion of the techniques used for structural characterization (X-ray diffraction (XRD), Raman spectroscopy, attenuated total reflectance-Fourier transform infrared (ATR-FTIR) spectroscopy). The basic principles of photoluminescence (PL), reflectance spectroscopy and finite-difference time-domain (FDTD) simulation method, used for studying optical behavior of prepared sample are summarized. Details of the contact angle measurements for understanding the wetting behaviour of the samples are also described. Further, the details of gas sensing facility and its applications are outlined.

2.1. Fabrication techniques

2.1.1. Metal assisted chemical etching (MACE)

The two-step metal assisted chemical etching (two-step MACE) technique was used for preparation of smooth SiNWs. After standard cleaning procedure, the Si wafer is housed into a home made Teflon electrochemical cell, depicted Fig. 2.1. It is worth to note that only one side of the Si-wafer (polished Si surface) is exposed to the solution using screw tightened Viton O-ring assembly. In the first-step, the deposition of metal (silver) is carried out using galvanic displacement deposition (electroless deposition) method in a solution mixture of HF and $AgNO_3$, followed by subsequent washing with 18.2 MΩ.cm grade water.

In the second-step, the etching of Ag deposited Si wafer was carried out in solution mixture of HF and H_2O_2. For both the steps, the same home made Teflon electrochemical cell was used.

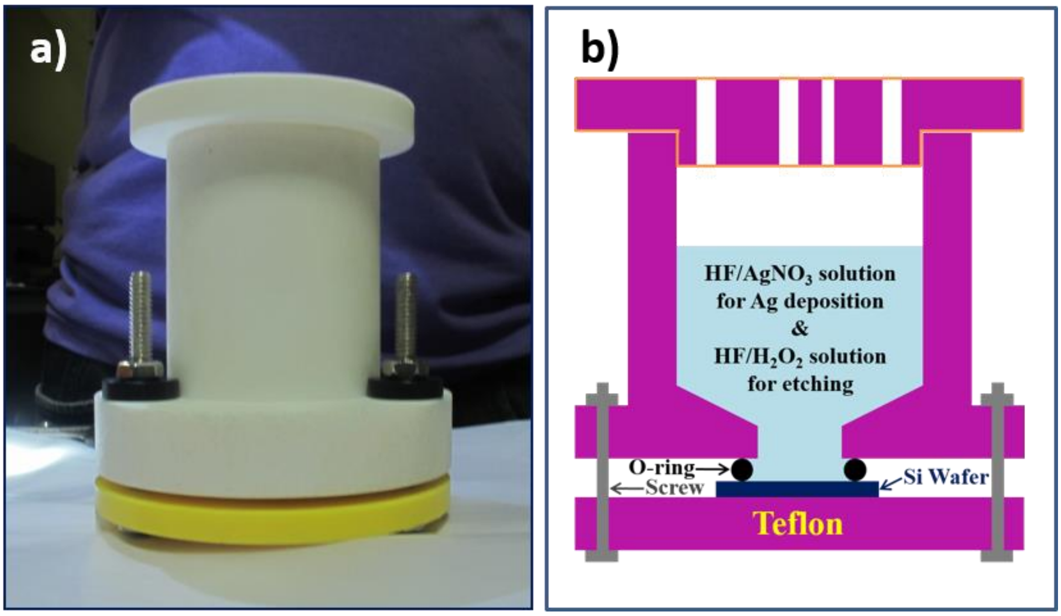

Figure 2.1 Description of home made Teflon electrochemical cell in a) Photographic view and b) Schematic view. The use of screw tightened Viton O-ring assembly ensures the corrosion and leak free deposition on one side of Si wafer.

2.1.2. Modified metal assisted chemical etching

Modified MACE was used for preapation of porous SiNWs. In the modified MACE, the first step is same as that of simple MACE (i.e the silver depostion on Si wafer by galvanic displacement depostion). However in the second step, an external constant current was applied to Ag deposited Si wafer (i.e modified MACE is combination of metal assisted chemical etching and anodic polarization etching) as shown schemtically in Fig. 2.2. In this configuaration, the other side (Ag free side of Si wafer) was in contact with a copper plate. Indium-Gallium eutectic alloy (99.99% purity, Sigma-Aldrich) was used between Si wafer and copper plate to ensure ohmic electrical contact. A constant current was applied between the Ag deposited Si wafer and graphitic carbon during etching.

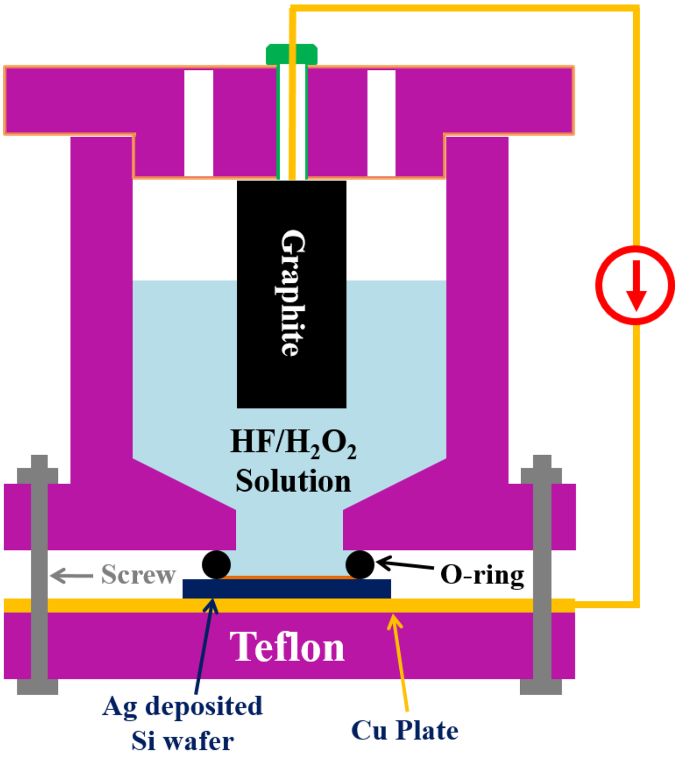

Figure 2.2 Schematic illustration of the electrochemical cell used for preparation of porous SiNWs. It is the same cell used for MACE, but this time a constant current was applied between the Ag deposited Si wafer and graphitic carbon.

2.2. Electrochemical characterization methods

2.2.1. Cyclic voltammetry

Cyclic voltammetry (CV) belongs to the group of potential sweep techniques and can be employed to study electron transfer kinetics and transport properties of electrolysis reactions [103]. The current is measured as a function of the linear potential applied. As species react at different potentials and with different intensity, the CV enables multiple detections in one measurement (qualitative), and estimation of their concentration in solution (quantitative). The current resulting from the potential application is due to the occurrence of redox reactions in the solution (Faradic current) and to the double layer charging (capacitive current). The current response is plotted as a function of voltage. Figure 2.3 depicts the CV of a reversible reaction using a macroelectrode. There are many possible techniques available for potentiometric experiments, but cyclic voltammetry is often the preferred technique due to its ease of experimental set-up and quantitative results.

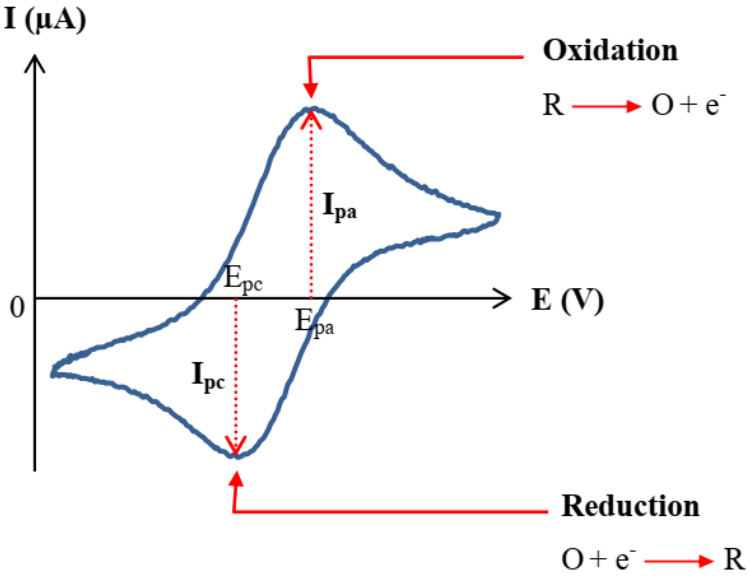

Figure 2.3 Cyclic voltammogram of a reversible reaction using a macroelectrode. E_{pc} *and* E_{pa} *are the peak potentials at the cathode and at the anode, respectively.* I_{pc} *and* I_{pa} *are the peak current at the cathode and at the anode, respectively.*

2.2.2. Charging/discharging

For galvanostatic cycling, the measured voltage at the electrode vs. time is recorded at a fixed current. An ideal capacitor can be charged and discharged for infinite cycles, thus cycle life is one of the important parameters for the electrochemical performance of material [103, 104]. Figure 2.4 shows the typical potential evolution under galvanostatic cycling where the curve A (red curve) and curve B (black curve) shows electric double-layer capacitive (EDLC) and pseudocapacitive behaviour of the electrode respectively. The potential evolution for EDLCs is symmetric during charging and discharging and nearly linear. On the other hand, the potential evolution for pseudocapacitive electrodes is asymmetric during charging and discharging and non-linear.

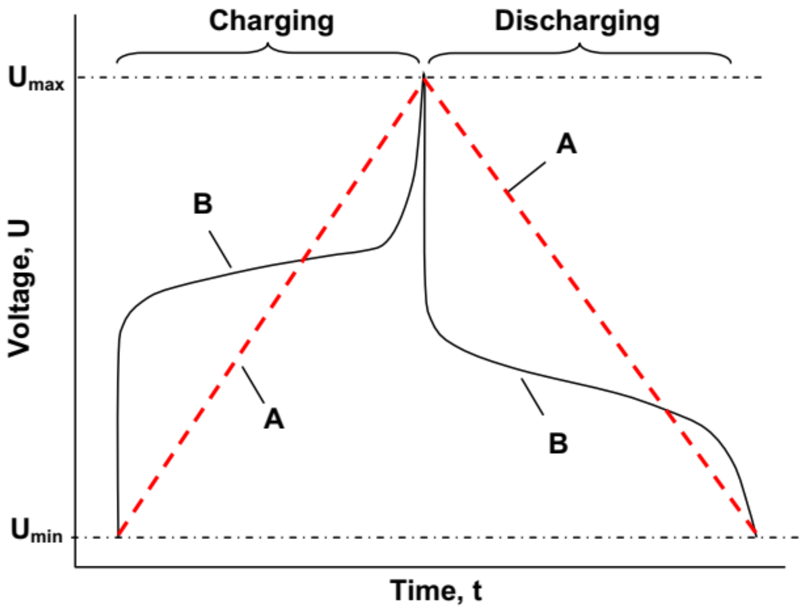

Figure 2.4 Illustrative comparison of the galvanostatic charging and discharging plots of a conventional supercapacitor (Electric double-layer capacitor: plot A, linear), and a supercapacitor containing a redox electrolyte (Pseudocapacitor: plot B, non-linear) [103].

The cyclic voltammetry and charging/discharging studies of the fabricated sample were conducted using the commercial potentiostat (Metrohm Autolab, model PGSTAT 302N) at room temperature. The sample was assembled into a home-built 3 electrodes electrochemical cell as shown in Fig. 2.5. In the cell, only the surface of Si wafer with SiNWs is exposed to the electrolyte. This is achieved by the use of an O-ring with screw tightening arrangement. The other side of the Si wafer was in perfect contact with a copper plate, where ohmic contact was ensured with the use of Indium-Gallium eutectic alloy (99.99% purity, Sigma-Aldrich). The SiNWs sample, platinum and Ag/AgCl couple were used as working, counter and reference electrodes respectively. A solution of tetraethylammonium tetrafluoroborate (NEt_4BF_4) in propylene carbonate (PC) was used as the electrolyte. All the electrochemical studies were performed in moisture free closed environment.

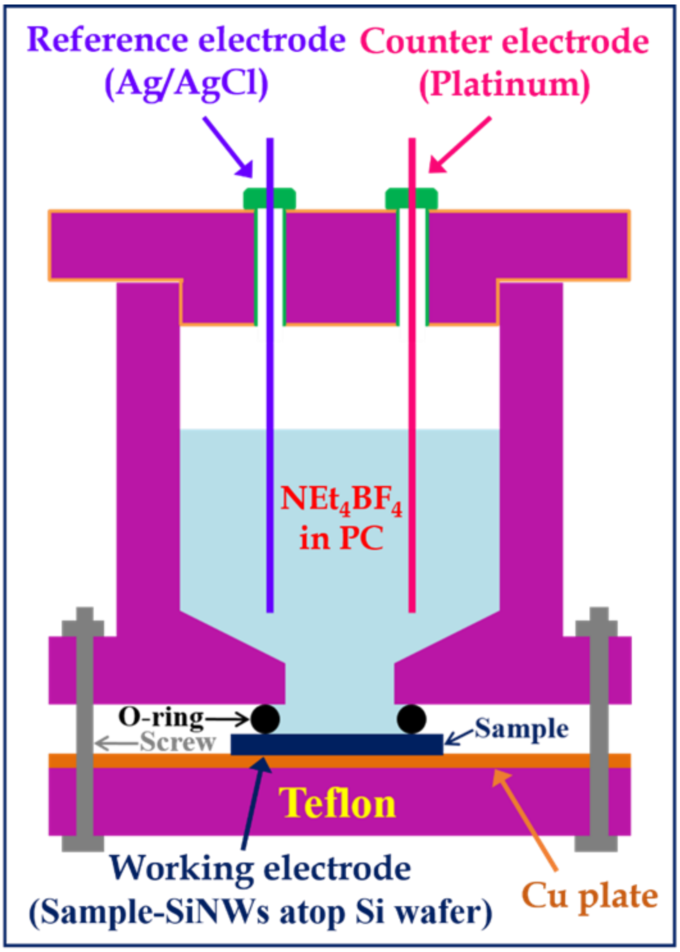

Figure 2.5 Schematic demonstrating the electrochemical cell set-up for electrochemical characterizations.

2.3. Structural and morphological characterization

2.3.1. Scanning electron microscopy (SEM) and energy dispersive X-ray spectroscopy (EDS or EDX)

In scanning electron microscopy, an electron beam is focused onto sample surface, kept in vacuum, by electro-magnetic lenses [105]. The beam is then scanned over the surface of the sample. The scattered electrons from the sample are then fed to the detector and then to a cathode ray tube through an amplifier, where the images are formed. This gives the information of the sample. The signals that derived from electron sample interactions reveal information about the sample including external morphology (texture), chemical composition, and crystalline structure and orientation. The field emission gun (FEG) is electron source. The FEG source has a number of advantages compared to the conventional thermionic emitter. It has high brightness, low evaporation of cathode material and low thermal drift during operation. These aspects enhance the resolution limits of a field emission SEM (FESEM). The FEG generates electrons and accelerates them to energy in the range 0.1-30 keV towards the sample. A series of lenses focus the electron beam on to the sample where it interacts with the sample to a depth of approximately ~1µm. Accelerated electron beam in a SEM carry significant amount of kinetic energy, and this energy is dissipated as a variety of signals produced by electron-sample interactions when the incident electrons are decelerated in the solid sample. These signals include secondary electrons (that produce SEM images), backscattered electrons (BSE), diffracted backscattered electrons (EBSD) that are used to determine crystal structures and orientations of minerals, characteristic X-rays that are used for elemental analysis and continuum X-rays, visible light and heat. Secondary electrons and backscattered electrons are most commonly used for imaging. Secondary electrons are most valuable for showing morphology and topography of samples and backscattered electrons are most valuable for illustrating contrasts in a composition of multiphase samples.

X-rays are produced when an electron moves from the outer to the inner shell of an atom, and they can be detected by the energy dispersive X-ray spectroscopy (EDS) which is coupled with the SEM. Each element has a different specific energy level of X-rays. The chemical composition is analyzed by a 2 µm wide beam or the average of a selected area. Abundance of elements present in the sample is given either as a spectrum, or as a map of the elements of interest. The EDS is equipped with a software, which aids identifying the elements in the spectrum, based on standard values. In this study, energy dispersive X-ray spectrometer equipped with FESEM (Model Zeiss SUPRA 55) with 30 kV source from a tungsten field emission tip was used to examine the morphology and structure of the prepared samples.

2.3.2. Transmission electron microscopy (TEM)

Transmission electron microscopy is a versatile and indispensable tool in the study of materials due to its high spatial resolution [106]. In this technique, a beam of high-energy electrons (typically 100-400 keV) is collimated by magnetic lenses and allowed to pass through a specimen, under high vacuum. The transmitted beam and a number of diffracted beams can form a resultant diffraction pattern, which is imaged on a fluorescent screen kept below the specimen. The diffraction pattern gives information regarding lattice spacing and symmetry of the structure under consideration. Alternatively, either the transmitted beam or the diffracted beams can be made to form a magnified image of the sample on the viewing screen as bright-and dark field imaging modes respectively. This gives information about the size and shape of the microstructural constituents of the material. High-resolution image contains information about the atomic structure of the material. This can be obtained by recombining the transmitted beam and diffracted beams together. All the diffracted electrons follow the Bragg's law $2d\sin\theta = n\lambda$, where d being the atomic spacing, θ being the angle between incident electron and atomic planes of the specimen, λ being the wavelength of incident electrons and n is an integer. By selecting the diffracted beam from a selected area on the specimen, selected area electron diffraction (SAED) pattern can be obtained. The SAED pattern is equivalent to an X-ray diffraction pattern. A single crystal leads to a well arranged spot pattern on the screen; a poly-crystal constitutes a ring pattern. Whereas, a glass or amorphous material produces a series of diffuse halos. The major components of the TEM can be categorized into the illumination system, the objective lens/stage, and the imaging system. By adjusting these three components of TEM and selecting the appropriate scattered electron beams from the specimen, several types of TEM images can be obtained. General analysis of the samples can be carried out by the different modes of the TEM, such as the bright field and dark field images, SEAD patterns, high resolution TEM (HRTEM) and fast Fourier transform (FFT) images. In the present thesis, the morphological and structural investigation of the prepared samples were carried out using HRTEM (LIBRA 200FE Zeiss) with 200 kV FE electron source. The schematic (Fig. 2.6) explains the function of the system.

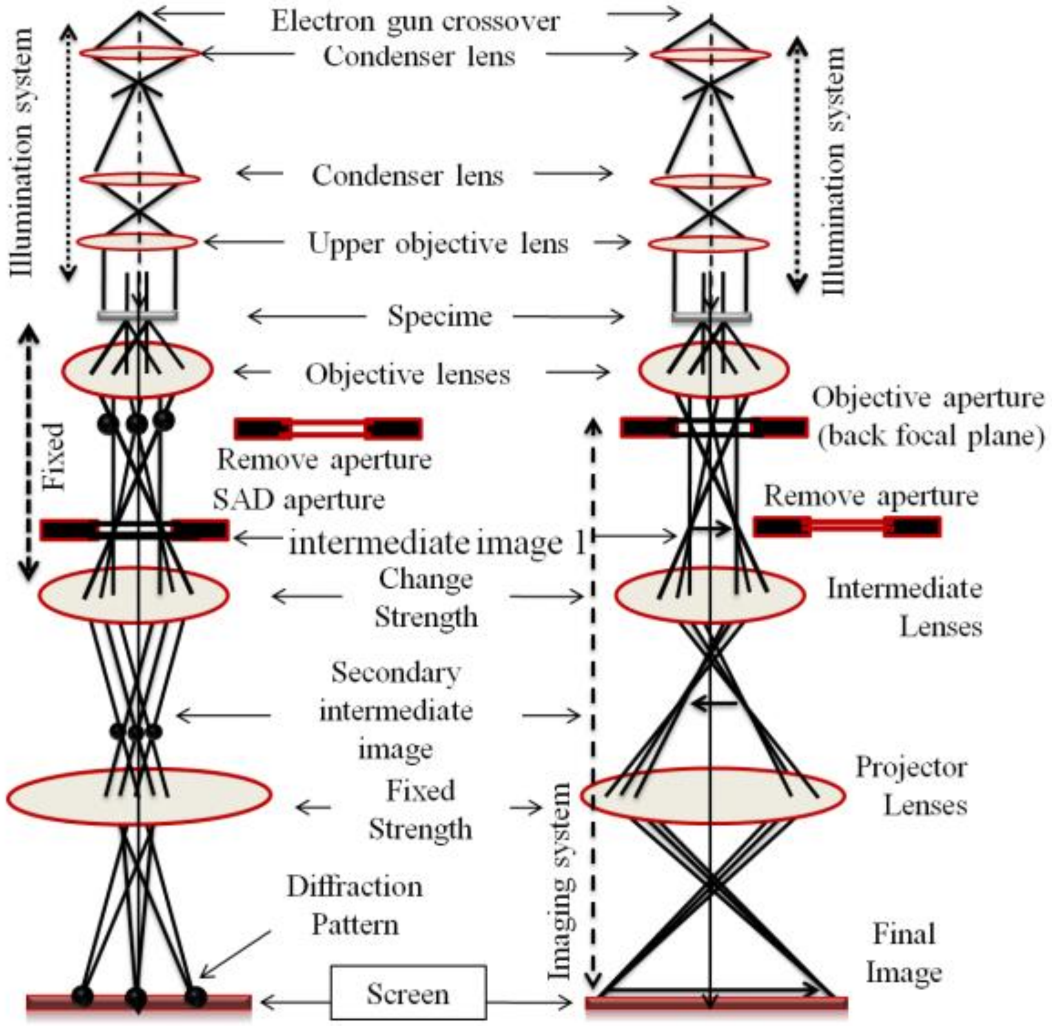

Figure 2.6 A ray diagram of TEM showing the diffraction mode operation (left side) and standard imaging mode operation (right side) with major components of the system.

2.3.3. X-ray diffraction (XRD)

When an electromagnetic radiation of wavelength λ is incident on a crystalline material having periodic structures in the length scale of λ; diffraction event takes place [107]. Since X-rays have wavelength comparable to interatomic spacing in a crystal, it can interact with the solid and scatter to produce a diffraction pattern. This happens when the interaction satisfies the Bragg's diffraction criterion given by, $n\lambda=2d\sin\theta$, where, n is an integer representing the order of diffraction, λ is the wavelength of the electromagnetic radiation, d is the inter-planar spacing for the family of diffracting planes and θ is angle between incident X-ray and atomic planes. The wavelength of the X-ray used is normally 1.54056Å (Cu Kα). Each peak in the diffraction pattern can be correlated to a set of planes in a crystal lattice. Different set of planes have different inter-planar spacing and according to Bragg's condition θ must vary with d variation. A schematic view of the X-ray Diffraction (XRD) process is shown in Fig. 2.7.

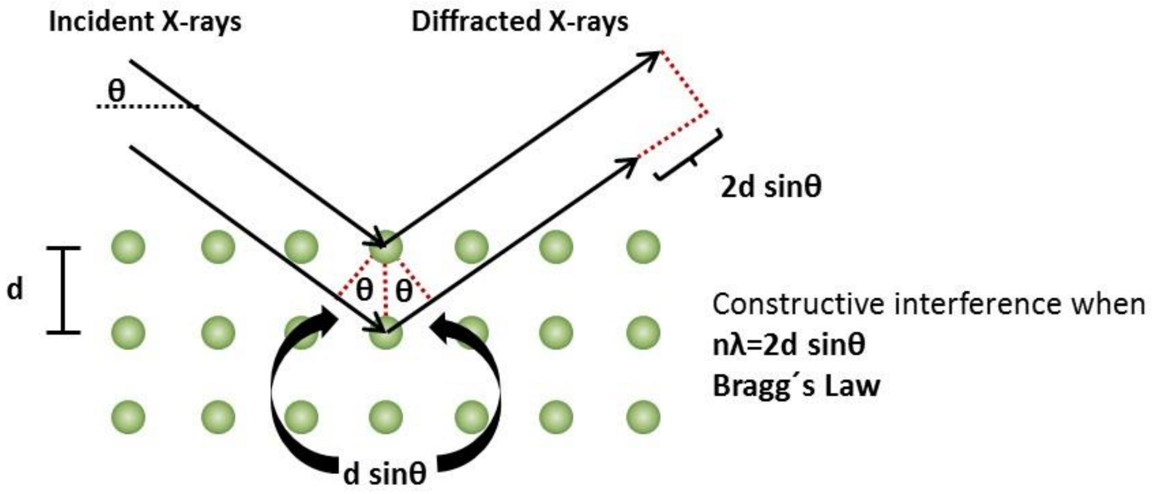

Figure 2.7 Schematic view of the X-ray diffraction (XRD) process

In the present study, grazing incidence X-ray diffraction (GI-XRD) (STOE / Inel, Equinox 2000) was used to reveal the structural information of fabricated samples.

2.3.4. Raman spectroscopy

In Raman spectroscopy, the material is excited with the laser beam of frequency ν_0 in the UV-Visible-IR region and the scattered light is analyzed. The scattered light consists of elastically scattered Rayleigh signal and inelastically scattered Raman signal as shown in

Fig. 2.8. Rayleigh signal comes with high intensity and frequency same as of the incident beam ν_0 . However, the Raman scattering is very weak (~ 10^{-5} of the incident beam) and has frequencies $\nu_0 \pm \nu_m$, where ν_m is the vibrational frequency of the system. ν_0- ν_m is called as Stokes line, and $\nu_0 + \nu_m$ is the anti-Stokes line [108]. Therefore, in the Raman spectroscopy, the vibrational frequency ν_m is measured as shift from the incident photon frequency ν_0. According to Maxwell-Boltzmann distribution law, the population of phonons in a solid at ground state is higher than the excited state. Therefore, the stokes lines are stronger than the anti-stoke lines. Since both Stokes and anti-Stokes lines provide the same information, in general practice the Stoke lines are measured experimentally because of its higher intensity than that of the anti-Stoke lines.

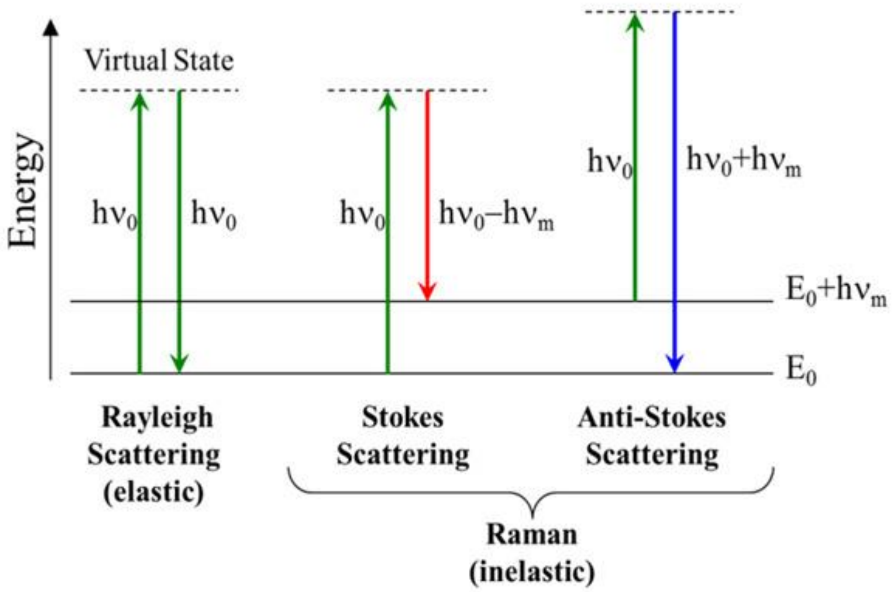

Figure 2.8 Schematic view of the elastic and inelastic processes in a material with incidence of light.

In the present thesis, the Raman spectra are recorded using Renishaw micro-Raman spectrometer (Model-INVIA). Figure 2.9. shows the schematic block diagram of facility. The major component and their working principle are briefly discussed below.

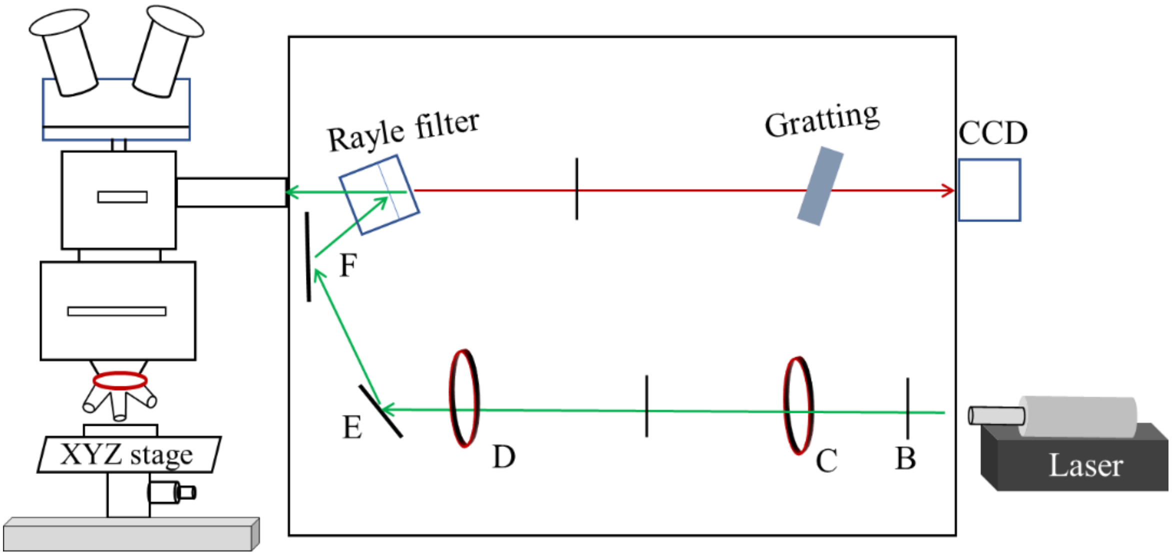

Figure 2.9 Schematic block diagram of the Raman setup with major parts, used for the present studies.

(i) **Laser:** An Ar^+ laser of wavelength of 514.5 nm was used as the light source for the Raman scattering measurement.

(ii) **Optical unit:** The laser entering the optical unit was first aligned by the mirror B followed by convergence to ~10 μm pinhole with the help of convergence lens C. Another objective lens D was used to make a well collimated parallel beam. The collimated parallel laser beam was reflected to the holographic filter with the help of mirrors E and F. The angle of the holographic filter was adjusted so that the laser beam can pass into the optical path of the microscope, located out of the spectrometer unit.

(iii) **Microscope unit:** The microscope unit helped in positioning and focusing the sample for the measurement. The microscope in the micro Raman system was facilitated with objective lenses of 5X, 20X, 50X and 100X for visible light.

Monochromator: In the Raman spectrometer the back scattered photons are dispersed through the single monochromator with gratings. The spectral resolution of the measurement is decided by the number of groves in the grating.

Detector: The dispersed light from the monochromator was focused on a charged coupled device (CCD), which served as a detector for spectra acquisition of the scattered photons.

2.3.5. Attenuated total reflectance - Fourier transform infrared (ATR-FTIR) spectroscopy

Fourier transform infrared (FTIR) spectroscopy is one of the vibrational spectroscopic tools, where infra-red (IR) spectra are measured. It relies on the principle of transmission of light [109]. When an infrared radiation is incident on the sample, molecules of sample selectively absorb radiation of specific wavelengths which cause the change in dipole moment of sample molecules. Consequently, the vibrational energy levels of sample molecules transfer from ground state to excited state. The frequency of absorption band, in the range of 4000-10 cm^{-1}, is proportional to the energy difference between the vibrational ground state and excited states. The number of absorption peaks depends on the number of vibrational degrees of freedom of the molecule. The intensity of absorption peaks depends on the possibility of transition of energy levels and change in dipole moment. FTIR spectroscopy is used to identify the functional groups like for instance C=O, C-H or N-H and for identifying the structure in the materials.

The attenuated total reflectance (ATR) crystal consists of an IR transparent material with a high refractive index and has polished surface (Fig. 2.10) [110]. As shown in the image, the infrared beam enters the ATR crystal at an angle of typically 45° (relative to the crystal surface) and is totally reflected at the crystal to sample interface. Due to its wave like properties, the light is not reflected directly on the boundary surface but by a virtual layer within the optically less dense sample (Goos-Hänchen effect [110]). The fraction of the light wave that reaches into the sample is called the evanescent wave. Its penetration depth depends on the wavelength, the refractive indices of ATR crystal and sample, and the angle of the entering light beam. Typically, it amounts to a few microns (ca.0.5-3µm). In those spectral regions where the sample absorbs energy, the evanescent wave will be attenuated.

After one or several internal reflections, the IR beam exits the ATR crystal and is directed to the IR-detector. To achieve a high quality spectrum some requirements must be fulfilled; Good contact between sample and ATR crystal has to be ensured as the evanescent wave penetrates only up to some microns into the sample. The refractive index of the crystal must be considerably higher than that of the sample.

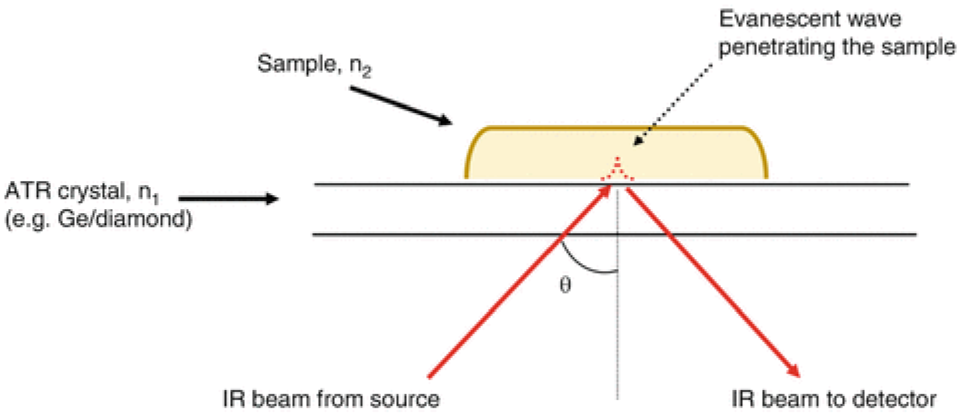

Figure 2.10 Schematic of the ATR-FTIR sampling mode (n, refractive index; θ, angle of incidence)

In the present studies, surface chemical bonding of prepared samples was investigated using ATR-FTIR spectrometer (Bruker Tensor II) in the spectral range of 700-4000 cm^{-1} using sixteen scans at 4 cm^{-1} resolutions.

2.4. Optical characterization

2.4.1. Photoluminescence (PL) spectroscopy

When an electromagnetic radiation is incident on a semiconductor material, a fraction of the incident photons get reflected at the surface and the rest transmit through the medium [111]. Inside the medium some of the photons may absorb or scatter while the remainder passes through the sample. Some of the absorbed photons may dissipate as heat or reemit at a different frequency. The latter process is known as photoluminescence. This is a radiative recombination process among excited carriers, such as, electrons/holes or excitons in semiconductor during external optical excitation process. When the photons of energy higher than that of the bandgap (E_g) of the semiconductor is incident on the material, the electrons get excited from the valence band to the conduction band via absorption of photons. After relaxation (non-radiative), the excited electrons return to the valence band by emitting photons of energy lower than the exciting photons as shown in Fig. 2.11 [111, 112]. The momentum conservation of the radiative recombination process of electrons and holes demands $k_e - k_h \sim 0$. Therefore, the luminescence efficiency of direct band gap semiconductors is significantly higher as compared to that of indirect band gap materials. The luminescence property of a material is also strongly affected by the presence of native defects, impurity, dopants and absorbed molecular species.

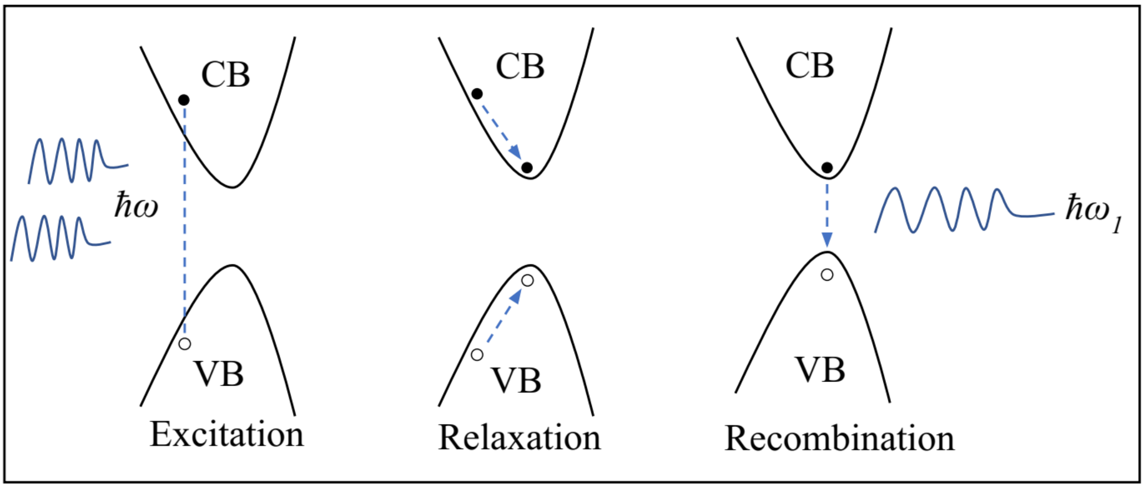

Figure 2.11 Schematic view of the PL process in a direct bandgap semiconductor

The PL study, reported in this thesis were carried out using the same setup used for the micro-Raman measurements (inVia, Renishaw) (Fig. 2.9). Low temperature PL measurements were recorded by cooling the samples in a liquid N_2 cooling stage.

2.4.2. Reflection spectroscopy

Reflection spectroscopy is used to measure the total amount of light that reflected off a diffusing material. The diffusing material is generally shaped into a slab of finite thickness. The instrumental apparatus for the measurement is a grating spectrometer equipped with an integrating sphere [113]. The integrating sphere is basically a hollow sphere. The internal surface of the integrating sphere is coated with a material having a very high reflectivity (generally > 99 %) across the entire infrared (IR), visible (Vis) and ultra-violet (UV) spectral range. The schematic of the reflection spectroscopy with the integrating sphere arrangement is shown in Fig. 2.12. The light enters through the entrance hole and get reflected form the sample placed at the exit hole. The reflected light undergoes multiple reflections on the inner surface of integrating sphere till it reaches the detector window. Fig. 2.13 a) show the measurement of only diffused reflection (or diffuse reflectance) where the specular component leaves the integrating sphere through the entrance hole. On the other hand, Fig. 2.13 b) shows the measurement of total reflection where the sample is tilted at some angle (ϴ) at the exit hole. If we denote specular, diffused and total reflection as T_{spec}, T_{diff}, and T_{tot}, then T_{tot} is given by,

$$T_{tot} = T_{spec} + T_{diff} \tag{2.1}$$

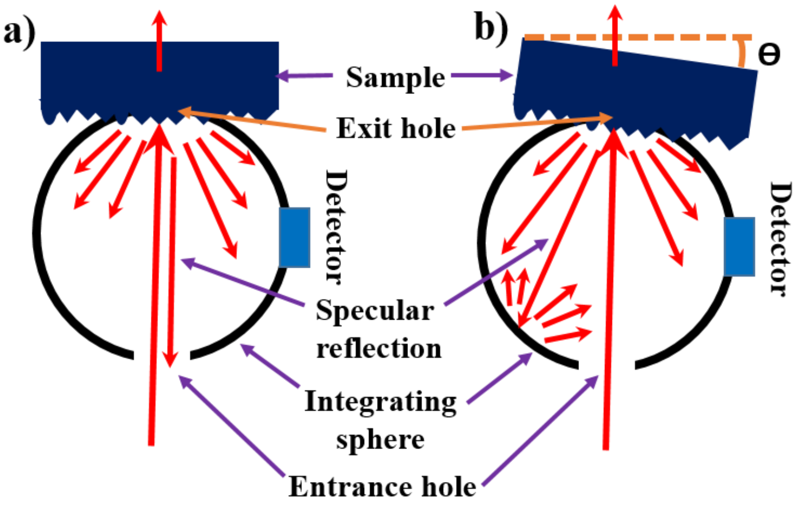

Figure 2.12 Schematic description of reflection spectroscopy with integrating sphere arrangement for a) diffuse reflection measurement and b) total reflection measurement.

The surface reflectance measurements of the prepared sample were carried out using a commercial UV-Vis-NIR spectrometer (Hitachi UH4150) with an integrating sphere arrangement.

2.4.3. Finite-difference time-domain (FDTD) method

Finite-difference time-domain (FDTD), a time domain method, is a numerical technique for solving Maxwell's equations in both time and space. This was first proposed by Yee [114]. The electric and magnetic field distribution for complex geometry can be obtained in this method. This method needs a Fourier transfer step to obtain frequency-resolved response.

The FDTD method involves the solving of time-dependent Maxwell̓s equation using a time-stepping algorithm in cubic lattice [114, 115]. A central approximation technique is used to discretize the Maxwell̓s equations. This produces a set of finite difference equations. The electric and magnetic components are calculated at different points about a unit lattice cell, and at alternating half-time steps (leapfrog steps). The formulation permits modelling of any arbitrary surfaces and shapes of metals and dielectric materials without needing any special modifications to satisfy boundary conditions at interfaces. This is because they are implicitly satisfied by Maxwell's equations.

For solving three dimensional structures, the FDTD method is computationally rigorous. This needs high resolution and multi-processor computers to run. The appropriate implementation of boundary conditions and the setting discretizing mesh with sufficient resolution in regions of interest decides the accuracy of the result.

In case of nanostructures, high resolution is essential in order to investigate its interaction with the incident radiation. Therefore, simulations were performed for either a single particle on a substrate or for a periodic array. It is important to optimize the set-up to have both accuracy and reduction of computational time.

In the present thesis, Lumerical FDTD Solutions 2013 software was used for the simulation.

2.5. Contact angle measurement

The contact angle (CA) is defined as the angle between the liquid-solid and liquid-vapor interface. Geometrically it is measured as the angle between the tangent to the liquid/air interface and the tangent to the solid/air interface [116]. This is schematically described in Fig. 2.13 a). The measurement can be used for investigating the surface wettability of the material of interest by a specific liquid. When the drop completely wets the surface, it indicates high surface energy. Depending on the value of contact angle, the wetting nature of the surface is further classified into four categories: hydrophilic, superhydrophilic, hydrophobic and superhydrophobic (Fig. 2.13 b)). The term is referred as superhydrophilicity, i.e.; the CA is ~ 0º (or < 10º). There exist surfaces, in which the CA will be more than 10° but less than 90º. This condition is known as hydrophilicity. When the CA will be ~ 180º (or > 150º) then the state is called superhydrophobic. When the CA ranges between 90º to 150º, the state is referred to hydrophobic.

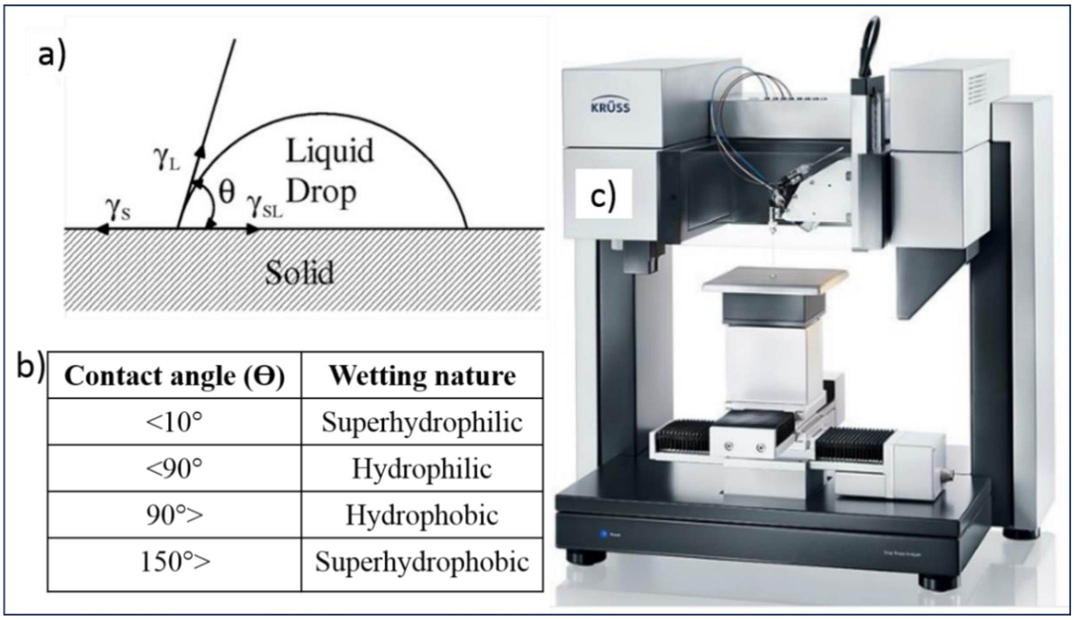

Contact angle (Θ)	Wetting nature
<10°	Superhydrophilic
<90°	Hydrophilic
90°>	Hydrophobic
150°>	Superhydrophobic

Figure 2.13 a) Schematic of contact angles (CA) formed by sessile liquid drops on smooth homogeneous solid surface, b) Table of CA with wetting property and c) Image of KRÜSS-DSA100M contact angle measurement setup .

In the present study, contact angle experiments of the samples were carried out in ambient environment using a contact angle meter (DSA100M, M/s. KRÜSS, Germany) provided with a CCD camera (Fig. 2.13 c)). The sessile drop method was used for the contact angle measurements. The surface energy and contact angle of the prepared sample were obtained using two liquids (water and diiodomethane). CCD camera was used to get the droplet image. The KRÜSS ADVANCE 1.6.2.0 software was used for data analysis.

2.6. Exposure facility for gas sensor (EFGS) testing system

The gas sensing properties of fabricated sample were studied using a custom-built exposure testing system whose schematic is shown in Fig. 2.14. The important components of the system include double walled stainless steel chamber, heater stage (also acting as sample holder), scroll pumps, flow controllers, pressure gauges, readout system, gas delivery lines and pneumatically actuated valves. The vacuum is maintained by using dry scroll pumps. Gas flow and temperature are controlled by mass flow controller (MFC) and PID controller respectively. The entire operation of the exposure facility system can be controlled externally using supervisory control and data acquisition (SCADA) software.

For electrical biasing and measurements on the sample, Agilent source measurements units were utilized. The sensor response, upon exposure to gases, manifests as a change in resistance of the sample. This resistance or other electrical output can be recorded on a PC via GPIB interface which is configured to acquire data at user-defined intervals. The variable parameters are vacuum inside the chamber, operation temperature and gas mass flow ratios to generate different concentrations of gas atmospheres. The gas sensing measurements were carried out using EFGS system in the dynamic condition. In dynamic sensing, the gas was flown at a constant flow rate over the sensor device while maintaining a fixed pressure in the sensing chamber under constant pumping using a dry pump.

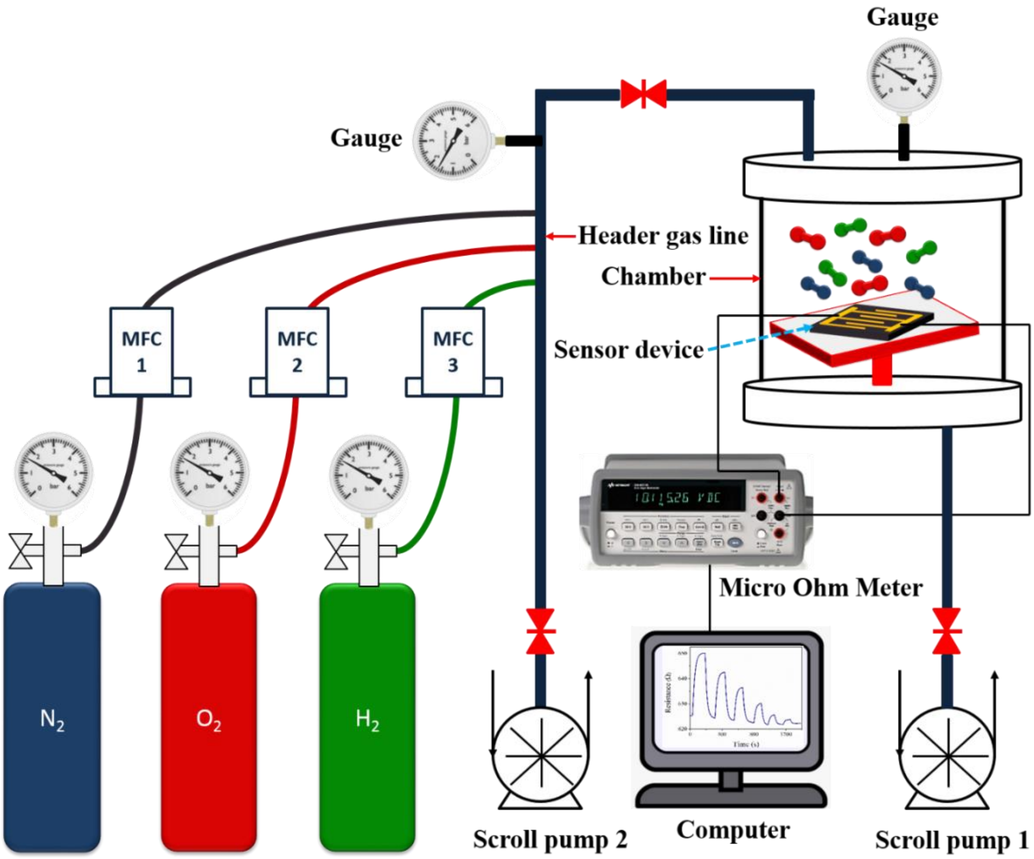

Figure 2.14 Schematic of the custom built gas exposure system for gas sensing measurement.

2.7. Summary

This chapter summarizes briefly the synthesis and characterization techniques utilized for conducting research on SiNWs and porous SiNWs. The basic principle of the microscopic imaging and spectroscopic characterization tools employed in the present study are described. The experimental techniques employed for studying the properties and applications of the fabricated samples are also summarized.

Chapter 3

Fabrication and characterization of Si nano-architectures by metal assisted chemical etching

---

Smooth and porous Si nanowall architectures were carved out on lightly doped Si wafers by 2-step metal assisted chemical etching (MACE) and modified MACE processes respectively. In the first step, silver metal was deposited in the form of interconnected Ag nano-cluster network with almost uniform separation by using the cost effective galvanic displacement deposition technique, in a home-made Teflon cell assembly. Optimization of process parameters to obtain the morphology was done and mechanism behind the same was delineated. In the second step, the Si wafer covered with the interconnected Ag nano-cluster networks is etched out to fabricate Si nanowall architectures and the etching parameters were varied to investigate their effect on morphology. The scanning electron microscopic studies of the fabricated Si nanostructures reveal that the synthesized structures are smooth and mostly wall like, bearing a linear dependence of its height with etching time and H_2O_2 *concentration. The HRTEM and GIXRD studies confirm that the Si nanowalls are single crystalline and (100) oriented, like the base Si wafer. The HRTEM studies further reveals that the surface of the nanowalls is smooth and covered with a thin amorphous layer. The amorphous layer was confirmed to comprise mostly of Si-O-Si bonded structures by ATR-FTIR and Raman spectroscopy. Porous Si nanowall architectures were fabricated by applying a constant current to the Si wafer during etching. The formation of porous Si nanowalls was confirmed by SEM and TEM studies.*

3.1. Introduction

The potential of Si nano-architectures is the ability of the Si nano-architecture based device’s compatibility with established CMOS technology, which can lead to direct on chip integration. The suitability of their application relies on the ability of the fabrication technique to control the morphological and structural parameters. Numerous techniques utilizing the bottom-up and top-down approaches [19, 117] have been developed with controllable synthesis parameters for the fabrication of desirable Si nanostructures. Among the various techniques, the bottom-up techniques viz. electrochemical (anodic polarization) etching and metal assisted chemical etching (MACE) are chosen by various research groups because of simplicity and cost effectiveness. MACE is preferred over electrochemical etching as it does not require sophisticated electrical power sources with high resolution and fine tuning ability. So owing to the simple, cost-effective and versatile nature of MACE along with the ability to produce different kind of nanostructures such as nanopores, nanowires, nanowalls, porous nanowires etc., with the potential to control parameters like cross-sectional shape, diameter, length, orientation etc. [41-43], it has been the focus of extensive scientific and technological attention in the recent past. Generally, MACE comprises of two successive processes viz. surface nucleation of metal catalysts and anisotropic etching. Depending on the occurrence of these two processes, it is categorized into: one-step MACE and two-step MACE [44]. In one-step MACE, the two successive processes occur in the etching solution containing HF and suitable metal salt (e.g. $AgNO_3$, $KAuCl_4$ etc.) [44, 45]. Whereas, in two-step MACE, metal catalyst deposition is followed by etching in the solution mixture of HF and a suitable oxidizing agent (H_2O_2, $Fe(NO_3)_3$, aerated O_2 etc.) [47-49]. Since, metal catalysts are deposited separately in two-step MACE, it has the advantage, over one-step MACE, in terms of independent control over metal morphology which decides the morphology of the synthesized Si nanostructures. For example, ordered arrays of nanowires, nanofins and nanoholes have been fabricated using two-step MACE with the proper patterning of the catalytic metal [50-55]. However, patterning of these metal over the substrate was achieved by using various lithography techniques like colloidal (or nanosphere) lithography, soft lithography, laser interference lithography, substrate conformal imprint lithography and deep ultraviolet lithography (UVL), which are complex and cost intensive. The alternative way of metal catalyst deposition is done by using vacuum techniques (thermal evaporation, e-beam evaporation, sputtering, laser ablation etc.) which are energy and cost intensive. The electroless metal deposition techniques, though patterning of metal morphology is difficult [56], possess the benefit that it is simple, versatile, cost effective and allow the whole process to be carried out in the chemical lab. Therefore, several researchers have utilized electroless deposition of catalytic metal (mostly Ag and Au) as the first step of MACE towards the synthesis of Si nanostructures and have studied the various properties and related applications of the fabricated nanostructures [6, 57, 58]. However, the study on effect of deposition parameters on the morphology of metal catalyst and its formation mechanism, which can help in producing desired Si nanostructures, is still lacking. Moreover, in two-step MACE, although the variation of etching parameters like etching time, HF concentration and oxidant concentration (mostly H_2O_2 is used) have been carried out in order to understand the underlying etching mechanism and their influence on Si nanostructures morphology [6, 59-71], more studies are still required to have a better understanding.

Synthesis of silicon nano-architectures using two step MACE with cost effective galvanic displacement deposition method for metal (Ag) deposition, optimization of process parameters, understanding the effect of the etching parameters in fine tuning the morphology and delineating the mechanism behind the formation of nanostructures are some of the highlights of the chapter.

The porous Si nanostructures (like porous nanowires/nanowalls) are new kind of nano-architectures which combine both the physical feature of nanowires/nanowalls and porous characteristics. The unique combination is expected to open novel avenues for Si-based optoelectronic and photoelectrochemical devices [6, 60]. As mentioned previously, MACE is capable of producing porous Si nanostructures. The porous Si nanostructure exhibit visible photoluminescence [5, 60, 61]. But, Si nanostructures with high porosity can only be fabricated on highly doped base Si wafer using MACE [60, 73, 74]. However, high doping concentration can cause spectral red shift and reduction in quantum yield of visible luminescence. Also, heavy doping can cause serious carrier recombination that leads to reduction in efficiencies of devices like solar cells [75]. Therefore, it is exciting to fabricate lightly doped porous Si nano-architectures using MACE for its wide range of potential application on industrial scale.

Fabrication of lightly doped porous silicon nanowalls/nanowires using modified MACE is a salient feature of the chapter.

3.2. Experimental

3.2.1. Synthesis of pore free Si nanowalls (SiNWs)

Single crystalline, (100) oriented, p-type (boron doped) Si wafers with resistivity 1-10 Ω.cm were used as the starting material for the present study. At the beginning, these wafers were ultrasonically cleaned by Milli-Q water (18.2 MΩ.cm), acetone and ethanol followed by copious rinsing in Milli-Q water trice after each step. The ultrasonically cleaned Si wafers were then cleaned with freshly prepared piranha solution (3:1 ratio of 98% H_2SO_4 and 30% H_2O_2) for 15 min in order to remove the residual organic contaminants. The cleaned wafers were subsequently washed thoroughly in Milli-Q water and dried by purging with 6 N purity nitrogen gas. The dried wafers were then treated with dilute HF solution to remove the surface oxide layer and housed into a home made Teflon electrochemical cell as depicted in Fig. 2.1 (Chapter 2). Silver deposition was carried out by galvanic displacement deposition (electroless deposition), in a solution mixture of HF and $AgNO_3$ (5% HF + 0.02 M $AgNO_3$) for different time durations viz. 15, 30, 45 and 60 seconds and subsequently washed thoroughly with 18.2 MΩ.cm grade water. Etching of Ag deposited Si wafer was carried out in solution mixture of HF and H_2O_2. First batch of sample were prepared at fixed solution concentration of 4.8 M HF and 0.4 M H_2O_2 for different etching time viz. 1, 2, 5, 15 and 30 minutes. Similarly, another batch of samples were prepared at fixed etching time of 10 minutes in solutions of 4.8 M HF and 0.2, 0.4, 0.6, 0.8 and 1 M concentrations of H_2O_2.

3.2.2. Synthesis of porous Si nanowalls (porous SiNWs)

For the preparation of porous Si nanowalls, modified MACE was used. After all the cleaning procedure (same as that in MACE for preapartion of SiNWs), the wafers were housed into the home made Teflon electrochemical cell used for modifed MACE, shown in Fig. 2.2 (Chapter 2). The etching was carried out in a solution mixture of HF/H_2O_2 with constant current of 5 mA.

It should be noted that the whole etching process in both MACE and modified MACE were carried out in dark to avoid the influence of light.

3.2.3. Characterization

Scanning electron microscope (SEM; Zeiss-Supra 55), high resolution transmission electron microscope (HRTEM; LIBRA 200FE Zeiss) and STOE grazing incidence X-ray diffractometer (GIXRD) are used to study the sample morphology and structure. The surface chemical bonding of the prepared samples was investigated using Bruker Tensor II FTIR spectrometer operating in attenuated total reflection (ATR) mode. The details about these techniques are discussed in Chapter 2.

3.3. Results and discussions

3.3.1. Electroless deposition (galvanic displacement deposition) of silver metal: First step of MACE

3.3.1.1. Electron microscopy & structural analyses

Figure 3.1 summaries the scanning electron microscopy and the X-ray crystallographic studies of the deposited Ag on Si wafer. The typical SEM morphologies of the Si exposed to 5% HF + 0.02 M $AgNO_3$ solution for 15, 30, 45 and 60 s are displayed in Fig. 3.1 a-d) respectively. It is observed from Fig. 3.1 a) that at low deposition time (15 s) isolated Ag nanoparticles are formed on the Si wafer. As depicted in Fig. 3.1 b, c), when the deposition time increases to 30 and 45 s respectively, the Ag nanoparticles gradually grow into clusters and some of the clusters join together forming interconnected clusters with an overall reduction in their inter-separation. Interestingly, it is manifested from Fig. 3.1 d) that for the deposition time of 60 s, all Ag clusters are interconnected with almost uniform inter-cluster separation. This indicates that 60 s time duration is the optimum deposition time and is a pre-requisite to fabricate stable Si nanowalls with uniform wall thickness. Figure 3.1 e) shows the grazing incidence X-ray diffraction pattern of Ag deposited for 60 s. The peaks arising at 38°, 44°, 64°, 78° and 82° are assigned to (111), (200), (220), (311) and (222) crystallographic planes of Ag lattice [International Centre for Diffraction data, File No. : 00-004-0783]. This manifests the polycrystalline nature of the deposited silver.

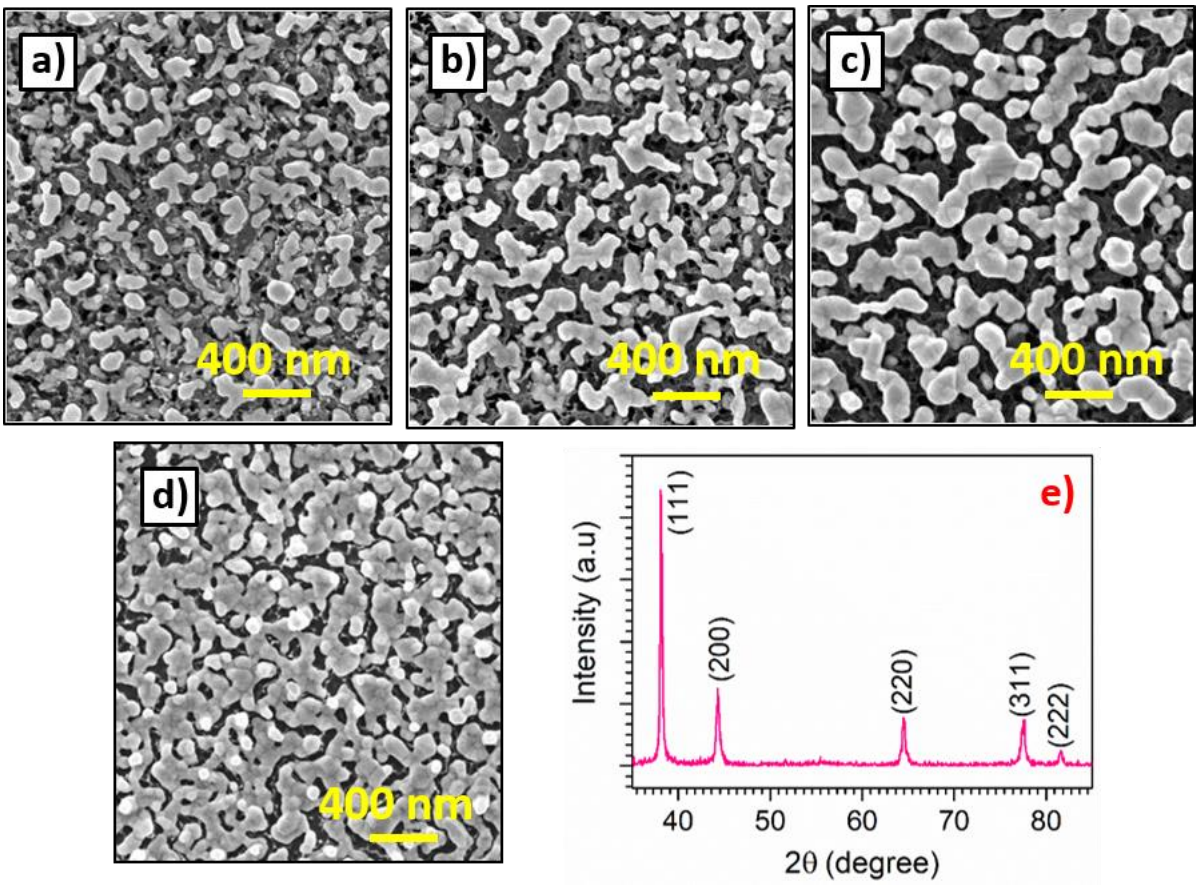

Figure 3.1 a-d) Scanning electron micrographs of Ag deposited on Si wafer for 15, 30, 45 and 60 s respectively. e) Grazing incidence X-ray diffraction pattern of 60 s Ag deposited Si wafer.

3.3.1.2. Synthesis mechanism

Before discussing the underlying growth mechanism of uniform interspaced Ag nanoclusters on Si wafer, it is worth to note that the growth of Ag has been achieved on Si in HF/$AgNO_3$ solution mixtures without using any external stimuli. Such a growth process is basically a galvanic displacement deposition (electroless deposition) where Ag^+ ions are reduced by the surface Si atoms. This can be understood by considering the energy level of Ag^+/Ag system and energy bands of Si. The potential energy of the redox pair Ag^+/Ag (0.79 V vs. SHE) being more than the valance band (VB) energy of Si (0.62 V vs. SHE) [48, 118], the reduction of Ag^+ is energetically favourable and also not limited by the minority carrier concentration in Si. Therefore, there is formation of micro-electrochemical galvanic cells on Si surface exposed to fluoride ion containing Ag^+ ion solution where both the cathodic and anodic process occur simultaneously. The cathodic process comprises the reduction of Ag^+ ions into Ag on Si surface and the anodic process involves the oxidation of Si underneath the reduced Ag. The redox reactions can be outlined as,

$$\text{At cathode: } Ag^+(aq) + e^- \rightarrow Ag^0\ (s) \qquad (3.1)$$

$$\text{At anode: } Si\ (s) + 2H_2O \rightarrow SiO_2 + 4H^+ + 4e^- \qquad (3.2\ a)$$

$$SiO_2\ (s) + 6HF \rightarrow H_2SiF_6 + 2H_2O \qquad (3.2\ b)$$

Although these redox reactions describe the overall growth of Ag on Si, the actual steps involved in the formation of interconnected Ag clusters is depicted in Fig. 3.2. At the beginning (Fig. 3.2 a)), the Ag^+ ions nearby Si surface capture electrons from the VB of Si and get deposited on Si as metallic Ag. The Ag nuclei on Si surface being more electronegative than Si strongly attract electrons from Si and become negatively charged. These negatively charged Ag nuclei now act as a catalyst and provide electrons for further reduction of upcoming Ag^+ ion in its vicinity. The continuous movement of Ag^+ ions into Ag nuclei and their deposition on Si leads to the growth of Ag nuclei into larger Ag particles. The simultaneous supply of electrons by Si beneath the Ag nanoparticles leads to local oxidation of Si and formation of SiO_2 underneath the Ag nanoparticles. These are shown schematically in Fig. 3.2 b). Subsequently, SiO_2 is etched out by HF forming shallow pits on Si surface and the Ag nanoparticles are trapped in these pits as shown in Fig. 3.2 c). As the process continues with time, the Ag nanoparticles grow into clusters, join together and finally an interconnected nanocluster of Ag assembly is formed with almost uniform inter-separation as displayed schematically in Fig. 3.2 d) and in tilted view in Fig. 3.2 e).

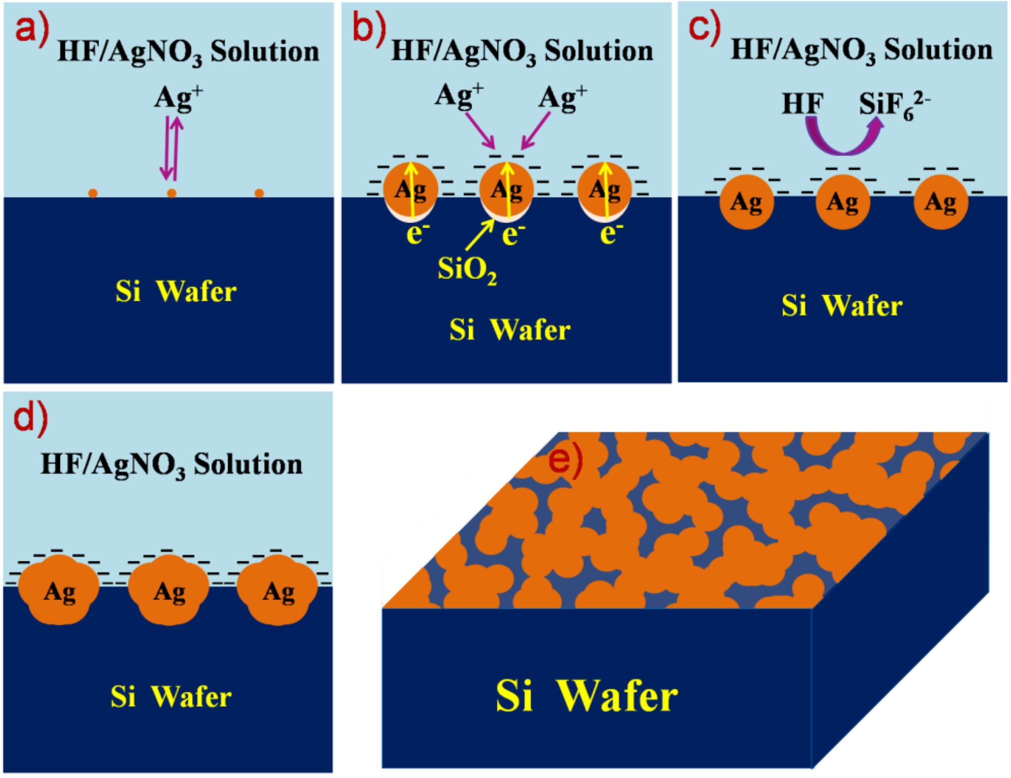

Figure 3.2 Schematic illustration of the formation of interconnected Ag nanocluster assembly on Si wafer. a) Nucleation of Ag particle. b) Ag particle growth with local oxidation of Si to SiO_2. c) Ag particles trapped into the pits. d) Growth of Ag nanoparticles into interconnected nanocluster assembly. e) Interconnected Ag nanocluster assembly on Si wafer displayed in tilted view.

3.3.2. Etching of Ag deposited Si wafer: Second step of MACE

3.3.2.1. Fabrication of nanowalls (Electron microscopy & structural analyses)

The 60 s Ag deposited Si wafer was preferred for etching in the solution mixture of HF and H_2O_2. The morphology and structure of the sample fabricated by 0.2 M H_2O_2 and 4.8 M HF etching solution mixture for 10 minute are given in Fig. 3.3. Figure 3.3 a) and b) display the top view SEM micrographs at low and high magnification respectively. The

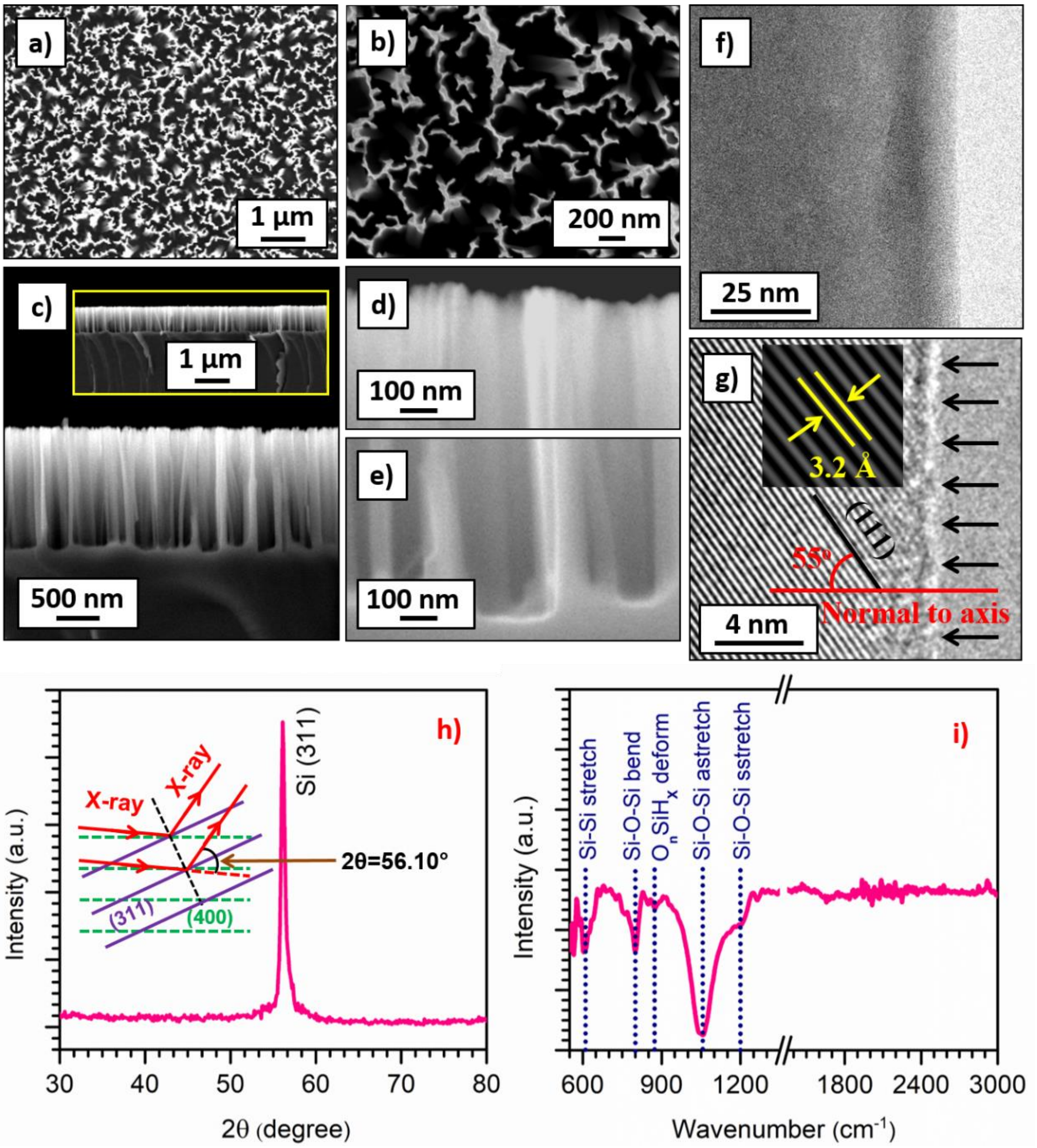

Figure 3.3 Electron microscopy, GIXRD and FTIR-ATR results. a, b) Low and high magnification SEM micrographs respectively. c) Cross-sectional SEM images. The inset in c) displays the cross-section view in larger area. d, e) A small portion of Fig. c) taken at its top and bottom represented in high magnification cross-section view respectively. f) TEM image of a nanowall. g) TEM micrograph of nanowall in high magnification. Inset in Fig. g) displays the inverse FFT pattern obtained from a selected region. The black arrows in Fig. g) indicate that the wall surface is covered with a thin amorphous layer. The angle between (111) plane (indicated by black line) and normal to the Si wall axis (indicated by red line) is portrayed in Fig. g). h) Depicts grazing incidence X-ray diffraction (GIXRD) pattern. i) Shows the ATR-FTIR spectrum.

cross-section views of the sample at different magnification are depicted respectively in Fig. 3.3 c-e). The top and bottom portion of Fig. 3.3 c) are shown in high magnification in Figs.

3.3 d) and e) respectively. Figures 3.3 a-e) indicate that the fabricated structures are mostly wall like. It is evident from Fig. 3.3 c-e) that the evolved walls are smooth, vertically aligned and uniformly formed over the whole etched region. The TEM image of a nanowall depicted in Fig. 3.3 f) reveals that surface is extremely smooth. This observation is in close agreement with the SEM results (Fig. 3.3 c-e)). Fig. 3.3 g) displays the high resolution TEM image of the wall structure which confirm the single crystalline nature of the evolved structure. The inset in Fig. 3.3 g) shows the inverse fast Fourier transform (FFT) pattern of small selected area. An inter-planar spacing of 3.2 ± 0.1 Å can be discerned from the analysis of the inverse FFT pattern, which corresponds to the (111) crystallographic plane of Si [International Centre for Diffraction data, File No. : 00-005-0565]. It is worth to note that the evolved Si nanowalls are produced from the (100) oriented base Si wafer. As illustrated in Fig. 3.3 g), the angle between the (111) crystallographic planes (indicated by black line) and the normal to the Si wall axis (indicated by red line) is ∼55º. This angle corresponds to the angle between (111) and (100) crystallographic planes of Si which suggests that the evolved SiNWs possess the same (100) crystallographic orientation as that of the base Si wafer. This is further confirmed from the analysis of the GIXRD pattern, displayed in Fig. 3.3 h). It is observed from Fig. 3.3 h) that only a single high intense diffraction peak appeared at 56.1º over the whole 2θ scattering angle measured from 20º to 80º. This sharp intense peak is ascribed to diffraction from the set of (311) planes of single crystalline SiNWs because in GIXRD configuration with Cu Kα as incident X-ray, the (311) oriented crystallographic plane which is 25.3º tilted from the (100) (or (400)) crystallographic plane, is the optimal plane that satisfies the Bragg diffraction condition [119]. This is schematically described in the inset of Fig. 3.3 h). Moreover, as indicated by the black arrow in Fig. 3.3 g), the surface of the nanowall is covered with a thin amorphous type layer. The EDX studies shows the presence of Si and oxygen (O). The Raman spectra show a high intense peak at 520 cm^{-1}

without any peaks in the range 460 to 490 cm^{-1} indicating the absence of amorphous Si. In order to identify the exact chemical and structural information of the amorphous layer, the FTIR spectroscopy in attenuated total reflection (ATR) mode, which is a well-known technique for surface characterization of materials, was conducted and the spectrum is depicted in Fig. 3.3 i). The ATR-FTIR spectrum exhibits a strong absorption band at 1050 cm^{-1} along with a shoulder at 1200 cm^{-1}, a band at 800 cm^{-1}, and two other bands at 873 and 610 cm^{-1}. The dominating bands at 1050, 1200 and 800 cm^{-1} corresponds to the antisymmetric stretching (a-stretch), symmetric stretching (s-stretch) and bending (bend) vibrational modes of Si-O-Si respectively [37, 120]. The other bands at 873 and 610 cm^{-1} are ascribed to the O_nSiH_x deformation (deform) mode and Si-Si stretching (stretch) mode respectively [37, 121]. This reveals that the amorphous structure observed in the surface of evolved nanowall consists of Si-O-Si bonded structures. It is revealed from the TEM and GIXRD studies that the metal assisted chemical etching has neither destroyed the crystallinity nor changed the crystallographic orientation in the prepared SiNWs with respect to that of base Si wafer.

3.3.2.2. Effect of etching time

In order to the investigate the influence of etching time, etching was carried out for different time viz. 1, 2, 5, 15 and 30 minutes in etching solution of fixed concentration of 4.8 M HF and 0.4 M H_2O_2. The scanning electron microscopy images of the prepared samples are summarized in Fig. 3.4. The topology and cross-section of the sample obtained by etching at 1, 2, 5, 15 and 30 minutes are depicted in Fig. 3.4 a, f), b, g), c, h), d, i) and e, j) respectively. It is observed that the nanowall obtained at low etching time are isolated from each other, whereas that obtained at high etching time (15 and 30 minute etching time, Fig. 3.4 d) and e)) are agglomerated at their top. The dimension of the agglomerated bundles is several micrometers. These agglomerated bundles are uniformly distributed on the whole surface. Fig. 3.4 k) display the height variation of nanowalls as a function of etching time. It shows that the height of nanowall exhibit a linear dependence on etching time. The etching rate was found to be 301 nm/min. Such linear dependence has been reported in literature but the etching rate values are different [69, 122, 123].

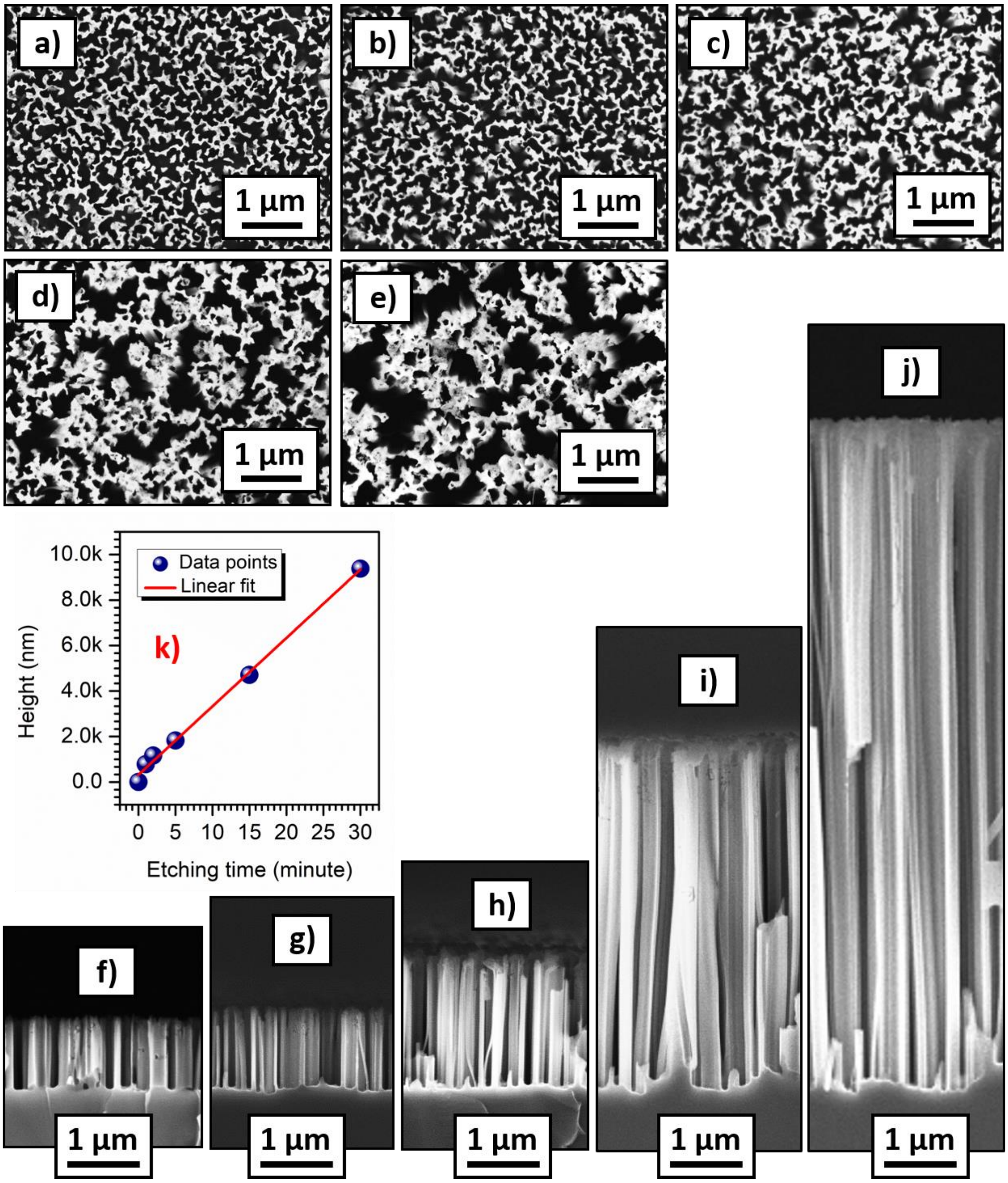

Figure 3.4 Scanning electron micrographs of the prepared sample at etching solution mixture of 4.8 M HF and 0.4 M H_2O_2 *for different etching time. Top and cross-section images are respectively displayed in a, f) 1 minute, b, g) 2 minute, c, h) 5 minute, d, i) 15 minute and e, j) 30 minute etching time. k) Plot depicting height vs. etching time of fabricated sample.*

3.3.2.3. Effect of H_2O_2 concentration

The influence of the etching parameter, H_2O_2 concentration, was also studied by preparing the sample at a fixed etching time of 10 minute in the etching solution mixture of 4.8 M HF and varying H_2O_2 concentration as shown in Fig. 3.5. The top and cross-sectional

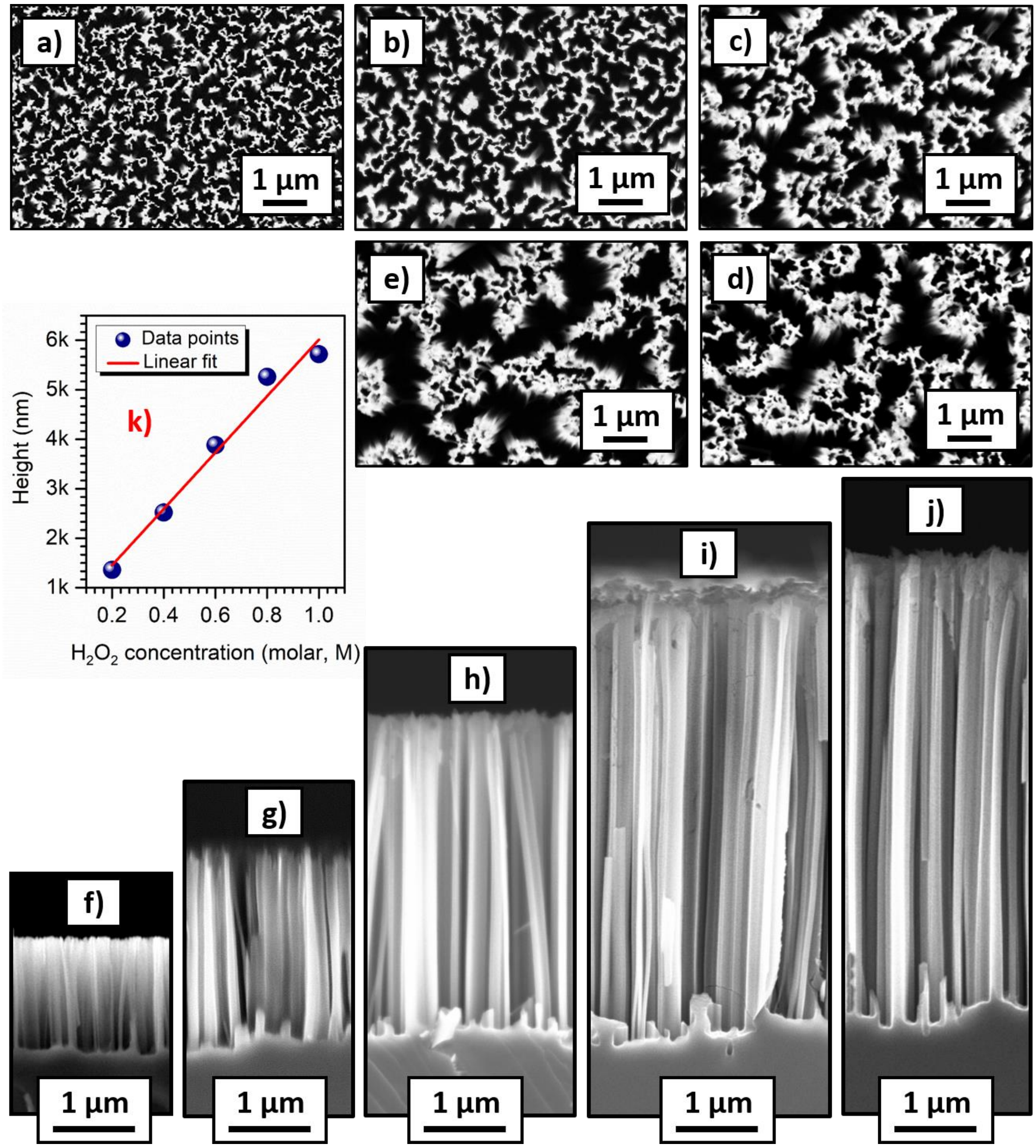

Figure 3.5 Scanning electron micrographs of the prepared sample at etching time of 10 minute for etching solution mixture of 4.8 M HF and various H_2O_2 concentration. Top and cross-section SEM images are respectively shown in a, f) 0.2 M, b, g) 0.4 M, c, h) 0.6 M, d, i) 0.8 M and e, j) 1 M H_2O_2 concentration. k) Plot displaying height vs. H_2O_2 concentration of fabricated sample.

SEM images of nanowall obtained at 0.2, 0.4, 0.6, 0.8 and 1 M H_2O_2 concentration are depicted in Fig. 3.5 a, f), b, g), c, h), d, i) and e, j) respectively. The morphology variation of nanowalls with H_2O_2 concentration was observed to be similar to that with etching time variation. It is evident that as the H_2O_2 concentration increases, the nanowalls start bunching at their top, which is clearly observed in the case of samples obtained at 0.8 and 1 M H_2O_2 concentration (Fig. 3.5 d) and e)). The effect of variation of H_2O_2 concentration on the morphology of Si nanowires was also studied by Liu et al. [59] where they have reported that the variation in H_2O_2 concentration from low to high leads to change in the morphology from nanowires to chaotic porous structures. The height variation of nanowall as a function of H_2O_2 variation is displayed in Fig. 3.5 k). This shows that the nanowall height varies linearly with H_2O_2 concentration with an etching rate of 5697 nm/M. The height variation with H_2O_2 concentration was reported by Moumni et al. [69], where they have observed a nonlinear height dependence on H_2O_2 concentration with the attenuation of height at high concentration.

Moreover, it is also observed from the SEM micrographs of fabricated samples (Fig. 3.4 and 3.5), that nanowalls prepared as a function of etching time and H_2O_2 concentration are smooth and free of pores. In order to get a better insight about the surface features, the high magnification SEM and TEM micrographs of the extreme sample (prepared at 30 minute etching time) are analysed as illustrated in Fig. 3.6. The cross-section view of top, middle and bottom portion of the nanowall obtained at 30 minute etching time are depicted in Fig 3.6 a-c) respectively. This reveals that the nanowalls are smooth and free of pore from its top to bottom. The broken region in the micrographs, indicated by red allows in Fig. 3.6 b, c) (which are formed while cleaving the sample for SEM cross-section studies) further support that the evolved structures are wall-like. The TEM micrograph of nanowall displayed in Fig. 3.6 d) also confirms that the wall structure is smooth and free of pores.

Figure 3.6 e) shows the high resolution TEM image of the wall structure which reveals that the wall is single crystalline and the surface is covered with a thin amorphous layer. The inter-planar spacing obtained from inverse fast Fourier transform (FFT) pattern of the selected portion of the wall structure is 3.2 ± 0.1 Å and matches with that of Si (111). This is similar to the results in Fig. 3.3 g).

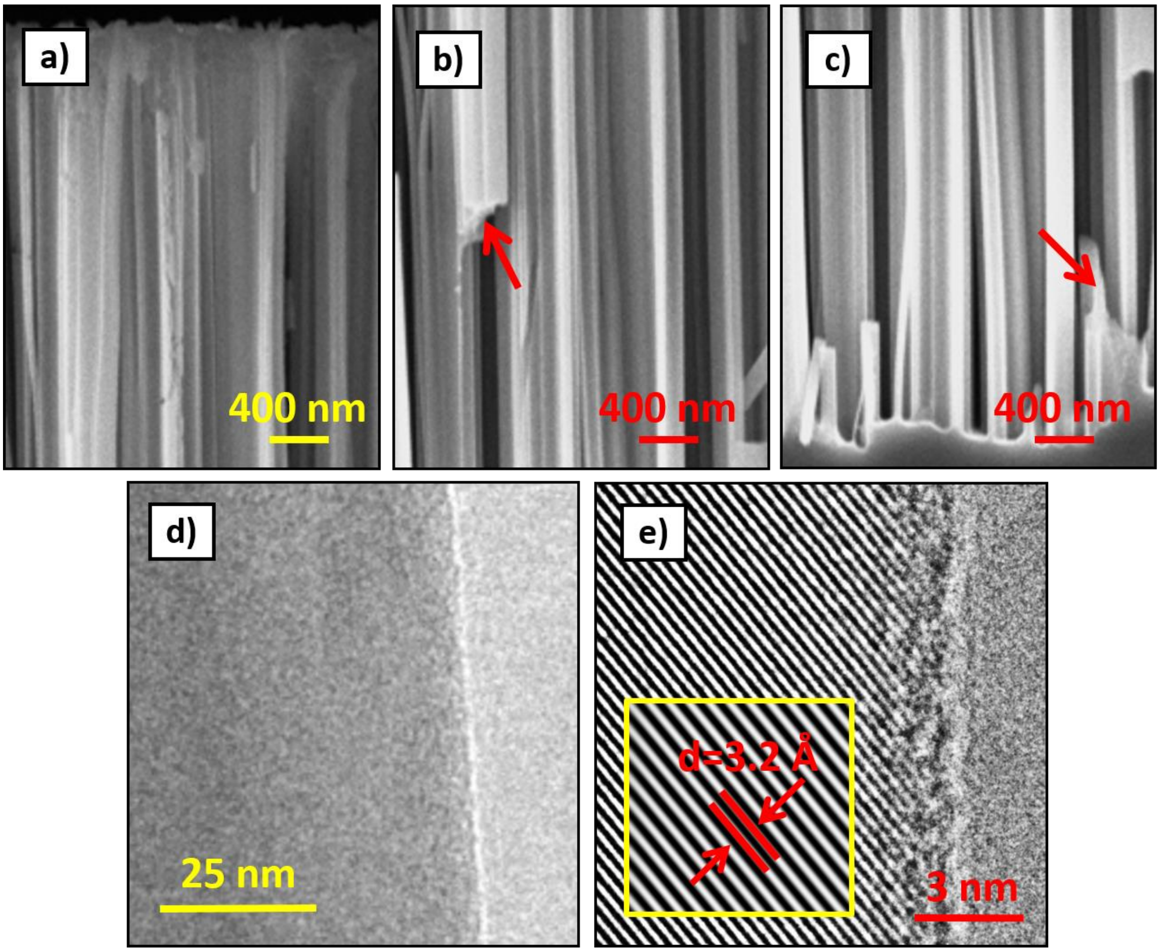

Figure 3.6 Electron micrographs of the sample prepared at 30 minute etching time. The high magnification SEM images of top, middle and bottom portions of the sample are respectively shown in a-c). The red arrows indicate the wall-like structure. d) TEM micrograph of a nanowall. e) HRTEM image of selected region. The inverse fast Fourier transform (FFT) pattern of a selected area is displayed in the inset.

3.3.2.4. Formation mechanism

Now it is worth to discuss the mechanism behind the formation of SiNWs, by etching the Ag deposited Si wafer in HF/H_2O_2 solution mixture. This can be realized by considering the potential energy of the redox pair H_2O_2/H_2O (1.78 V vs. SHE) and valance band (VB) energy of Si (0.62 V vs. SHE) [118] . Since the potential of redox pair H_2O_2/H_2O is much more positive than the VB energy of Si, it can extract a bonding electron from VB (or equivalently can inject hole into VB) of Si which is the fundamental requirement for Si etching. But, it has been found that the etching rate of bare Si in HF and H_2O_2 solution is extremely low (lower than 10 nm per hour) [41]. This infers that the fast etching of Si in HF and H_2O_2 solution mixture obtained in the present study is due to the presence of the noble metal Ag. In fact, the extraction of electrons from the VB (or equivalently the injection of holes into VB) of Si by the oxidant H_2O_2 leads to the cathodic process. The current density of the cathodic process can be described by the expression [48],

$$j_c = -zek_c n_s c_{ox} \exp\left(-\frac{E_a}{k_b T}\right) \tag{3.3}$$

Where j_c is the current density of cathodic process, z is the number of electrons transferred during the reaction, e is the electronic charge, k_c is the reaction rate constant, n_s is the density of electron at Si/HF/H_2O_2 solution interface, c_{ox} is the oxidant concentration at the interface, E_a is the activation energy for cathodic reaction, k_b is the Boltzmann constant and T is the absolute temperature. The expression suggests that the reduction in activation energy, E_a can enhance the current density and hence the reaction. The catalytic activity of the metal species (Ag) can be considered as a reduction in the activation energy, E_a for the cathodic reaction. So for the current electrochemical system of Ag nanocluster deposited Si wafer in HF/H_2O_2 solution, the etching of Si will take place preferentially in the vicinity of Ag nanocluster with the surface of nanocluster facing the HF/H_2O_2 solution acting as cathode and the surface of nanocluster facing the Si acting as anode. The cathodic half reaction involves the catalytic reduction of H_2O_2 atop the Ag nanocluster, consuming protons (H^+ ion) and electrons, whereas the anodic half reaction involves the oxidation of silicon beneath the Ag nanocluster, generating the H^+ ion and electrons and its subsequent dissolution by HF. The two half-cell reactions along with its overall reaction can be outlined as;

At cathode: $H_2O_2 + 2H^+ + 2e^- \rightarrow 2H_2O$ (E^0 =1.78 V vs. SHE) (3.4)

At anode: $Si + 2H_2O \rightarrow SiO_2 + 4H^+ + 4e^-$ (3.5 a)

$SiO_2 + 6HF \rightarrow H_2SiF_6 + 2H_2O$ (3.5 b)

Overall at anode: $Si + 6HF \rightarrow H_2SiF_6 + 4H^+ + 4e^-$ (E^0=1.2 V vs. SHE) (3.5 c)

Overall redox reaction: $Si + 2H_2O_2 + 6HF \rightarrow H_2SiF_6 + 4H_2O$ (3.6)

The motility of Ag nanocluster into the Si wafer can be described by referring to the self-electrophoresis model proposed by Peng et al. [124] in the above electrokinetic process of charge transportation. Since, the potential of the cathodic site (E_{H2O2} =1.78 V vs. SHE) is greater than that of anodic site (E_{Si}=1.2 V vs. SHE), there will be a flow of local corrosion current from cathodic site to anodic site with Ag particle serving as short-circuit galvanic cell. The flow of electron in the short-circuit galvanic cell (i.e through the Ag particle) is coupled to the transportation of H^+ ion in the etching solution surrounding the Ag particles as depicted in Fig. 3.7 a). The H^+ gradient across the Ag particle would build-up an electric field. This will drive the Ag particle (being negative charge) towards anodic site (i.e. in the downward vertical direction inside the Si wafer as shown in Fig. 3.7 b). So for the interconnected Ag nanocluster-network assembly in HF/H_2O_2 solution, the continuation of the above process leads to the un-etched part of Si to be protruded as vertical Si nanowall atop the Si wafer as illustrated in Fig. 3.7 c). The removal Ag nanocluster assembly by treating with conc. HNO_3 results the Ag free vertically aligned SiNWs. The linear increase of nanowall height with etching time can be attributed to the fact that, under the prepared etching solution composition, the solution possesses adequate amount of both oxidizing agent (H_2O_2) and etchant (HF), as a result the redox reaction proceeds retaining the etching process with time. In order to understand, the effect of etching parameter H_2O_2

concentration, the potential for the total reaction (equation 3.6) which characterizes the etching process can be expressed as [6, 72],

$$\Delta E = \Delta E^0 - \frac{0.059}{4}\left\{log\frac{[SiF_6^{2-}]}{[H_2O_2]^2[H^+]^4[F^-]^6}\right\} \qquad (3.7)$$

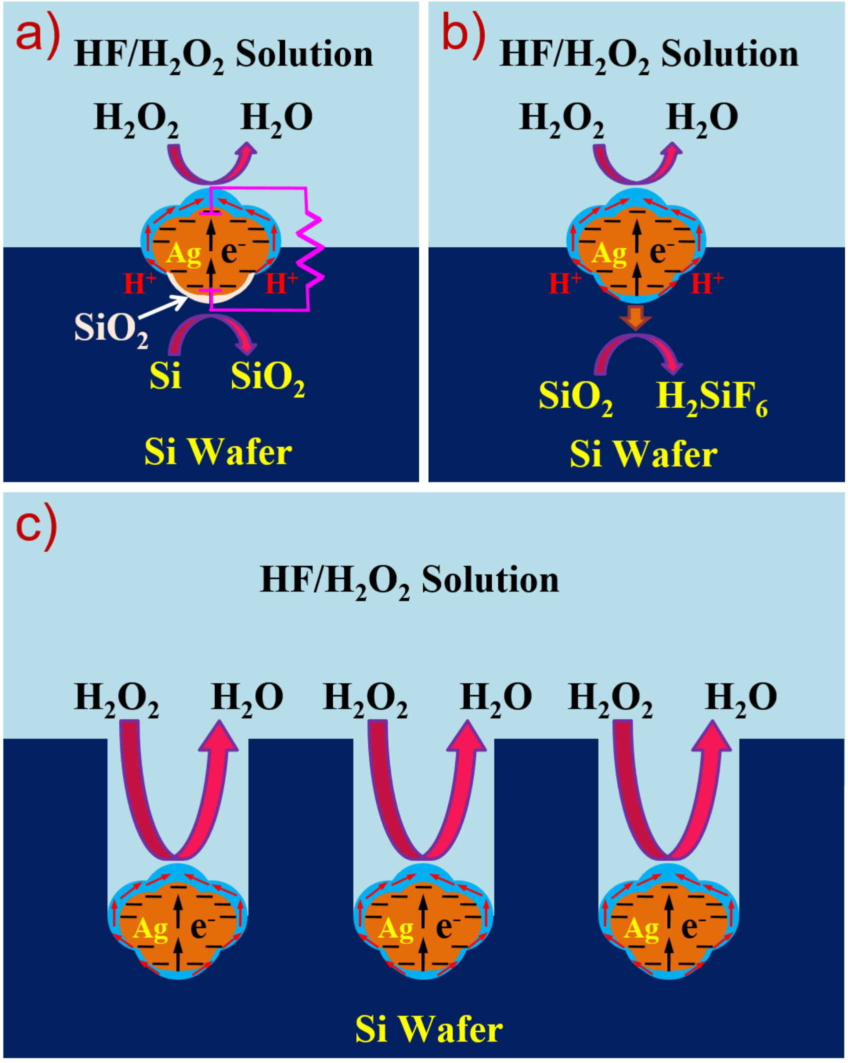

Figure 3.7 Schematic representation of electro-kinetic process involved in the movement of Ag nanocluster assembly in Si in HF/H_2O_2 solution. a) Generation of electric field across the Ag nanocluster assembly. b) Motion of Ag nanocluster in the presence of electric field. c) Collective movement of interconnected Ag nanocluster assembly in a direction normal to Si wafer, leading to the formation of vertical aligned nanowalls.

It is evident from the expression that with increase in H_2O_2 concentration the potential for the etching process increases. This shows that, thermodynamically the reaction for etching is more favourable and the etching can be enhanced. So the height of the nanowall also depend on oxidant concentration (H_2O_2). However, the oxidant concentration cannot be increased infinitely. For example, as discussed before, Liu et al. [59] have observed that the variation of H_2O_2 concentration to very high values leads to change in the morphology from nanowires to chaotic porous structures. Similarly, the variation of H_2O_2 to very high concentration can affect the etching rate (discussed before) as studied by Moumni et al. [69], where they have reported a nonlinear height dependence on H_2O_2 concentration with the attenuation of height at high concentration. This can be ascribed to the fact that, although the increase of H_2O_2 concentration to high value increases the rate of oxidation of Si, but the etching solution may not have enough HF to dissolve the formed SiO_2 at the corresponding rate to follow the same etching rate. Therefore, it is preferable to select proper range of etchant concentration to get good quality nanowalls. This indicates that in the present study, nanowalls are fabricated at the appropriate range of etchant concentration, where the variation of etching parameter has only changed the height of nanowalls without destroying it.

The bunching of SiNWs at higher etching time and H_2O_2 concentrations can be understood by considering the complex equilibrium among the various forces that act on the nanowalls. These forces are mainly: surface tension force of liquid-vapour interface that acts when the liquid level falls below the tip of nanowalls, van der Walls force that arises due to mutual electric interaction among the SiNWs and the elastic deformation force due to the stiffness of nanowalls [125]. The van der Walls force being very weak, the surface tension force of liquid-vapour interface is the driving force for the bunching of nanowalls. However, the van der Walls force becomes strong, as the separation between nanowalls decreases, and significant for very low separation. At high etching, the SiNWs being long, the surface tension force of liquid-vapour interface overcomes the elastic deformation force of SiNWs and bend the SiNWs. Due to the bending, the separation between the SiNWs reduces, which increases the van der Walls force of attraction making it favourable for bunching. This results in the aggregation of nanowalls at higher etching time and H_2O_2 concentration.

3.3.3. Fabrication of lightly doped porous silicon nanowalls/nanowires using modified MACE

3.3.3.1. Electron microscopy & structural analyses

The porous SiNWs synthesized using the modified MACE method were characterised for its morphology and structure. The electron microscopy and structural results of the porous SiNWs are summarized in Fig. 3.8. For comparison, the electron microscopic results of smooth SiNWs prepared under the same condition without the application of constant current are also summarized. Figure 3.8 a) and d) depict the top SEM images of porous and smooth walled nanowalls respectively. The inset in Fig. 3.8 a, b) shows their respective cross-section. The SEM micrographs illustrate that the Si wall structure is homogeneous in both the cases. Figures 3.8 b, e) show the TEM image of porous and solid nanowall respectively, the porous morphology of the SiNWs from that of smooth surface of solid nanowalls can easily be discerned. The HRTEM images of porous and smooth nanowalls are depicted in Fig. 3.8 c) and f) respectively. The analysis of these HRTEM images reveals the single crystalline nature of both porous and smooth nanowalls. Typical inverse fast Fourier transform (FFT) patterns obtained from the respective selected area in Fig. 3.8 c and f) are displayed in the inset. The analysis of these inverse FFT patterns yield inter-planar spacing of 3.2 ± 0.1 Å, which corresponds to Si (111) [International Centre for Diffraction data, File No.: 00-005-0565]. A thin amorphous type layer has been observed on the surface of the porous nanowall (indicated by white colour arrows in Fig. 3.8 c)) similar to that in smooth nanowalls shown in Fig. 3.8 f). The SEM micrographs obtained under different magnifications are also displayed in Fig. g-k), which reveals large density

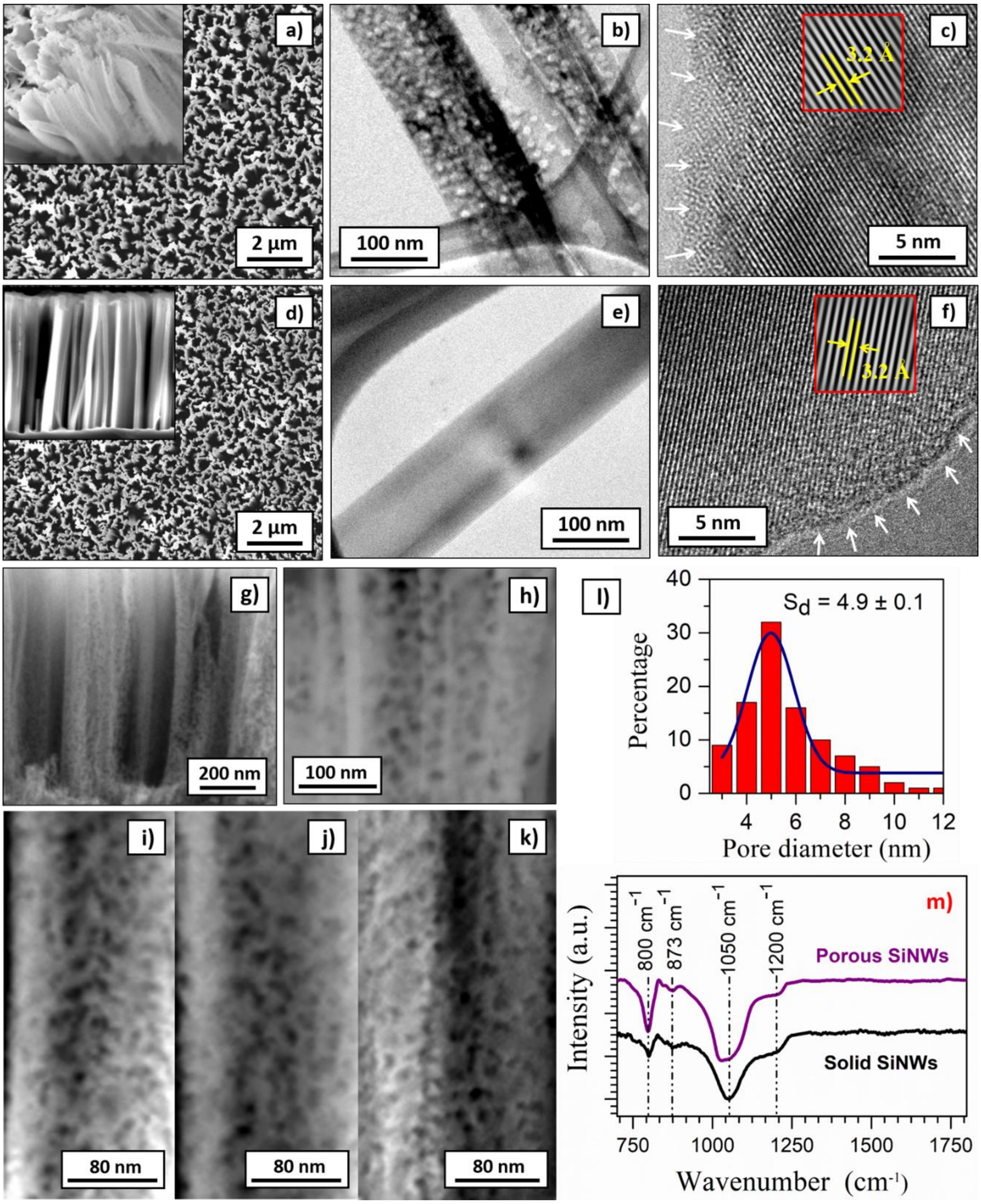

Figure 3.8 Electron microscopy and structural results of porous and solid SiNWs. a, d) Top view SEM images of porous and solid nanowalls, respectively. The insets in Fig. a) and d) show their respective cross-section view. b, e) TEM images of porous and solid nanowalls respectively. g, h) HRTEM images of the selected area in figures b) and e), respectively. The white arrow shows the thin amorphous layer covering the wall surfaces. The inverse fast Fourier transform (FFT) patterns of selected areas in Fig. c) and f) display a typical Si (111) arrangement. g-k) SEM images of porous Si nanowall shown in different magnification. l) Display the pore size distribution histogram which yields an average pore diameter, S_d = 4.9 ± 0.1 nm. m) ATR-FTIR spectra of both porous and solid nanowalls.

of pores. The diameter of the pores measured in 250 regions was used to obtain the pore size distribution histogram. The pore size distribution histogram as depicted in the inset of Fig. 3.8 l) yields an average pore diameter of 4.9 ± 0.1 nm. It is seen that the porous structure formed in the SiNWs fairly resembles the porous silicon nanostructures obtained by the anodic polarization etching [126, 127]. In order to get further insight about the thin amorphous type layer the ATR-FTIR studies have been performed, as depicted in Fig. 3.8 m), from 700 to 1800 cm^{-1} where the features corresponding to the surface bonding appear. It is observed that both porous and smooth nanowalls exhibit similar vibrational properties where ATR-FTIR spectra exhibits a strong absorption band at 1050 cm^{-1} along with a shoulder band at 1200 cm^{-1}, a band at 800 cm^{-1} and 873 cm^{-1}. As discussed previously, the dominating bands at 1050, 1200 and 800 cm^{-1} corresponds to the antisymmetric stretching (a-stretch), symmetric stretching (s-stretch) and bending (bend) vibrational modes of Si-O-Si respectively [37, 120]. The other bands at 873 cm^{-1} is ascribed to the O_nSiH_x deformation (deform) mode [121]. So the evolution of amorphous structure in the surfaces of SiNWs, as observed from the HRTEM images (Fig. 3.8 c, f)), is due to the existence of Si-O-Si structures. This suggests that the modified MACE has neither destroyed the crystallinity nor changed the crystallographic orientation of the as synthesized porous SiNWs similar to the smooth nanowalls obtained using simple MACE technique.

3.3.3.2. Synthesis mechanism

Now, it is worth discussing the formation mechanism of porous SiNWs. As indicated earlier, the modified MACE used to prepare porous SiNWs is a combined process of MACE and anodic polarization etchings. The process is schematically described in Fig. 3.9. As illustrated in the figure, there is formation of two electrochemical cells: i) galvanic cell formed at the Ag nanocluster with surface facing the etching solution acting as cathode and its surface in contact with Si acting as anode, similar to that in MACE, ii) the electrolytic cell with Si acting as anode and graphitic carbon acting as cathode. In galvanic cell, redox reaction occurs between the oxidant H_2O_2 and Si beneath the Ag cluster deposits and in the electrolytic cell, the external current drives charge transfer redox reaction between graphitic carbon and Si wafer. The electrolytic and galvanic charge transfer reactions that occur during etching process can be outlined as [64, 128, 129],

At galvanic cell;

At cathode: $H_2O_2 + 2H^+ + 2e^- \rightarrow 2H_2O$ (3.8)

At anode: $Si + 2H_2O \rightarrow SiO_2 + 4H^+ + 4e^-$ (3.9 a)

$SiO_2 + 6HF \rightarrow H_2SiF_6 + 2H_2O$ (3.9 b)

At electrolytic cell;

At cathode: $2H^+ + 2e^- \rightarrow H_2$ (3.10)

At anode: $Si + 4\ HF^{2-} \rightarrow SiF_6^{2-} + 2HF + H_2 + 2e^-$ (3.11)

These reactions create distinct current paths I_1 and I_2. The current I_1 generated from the electrolytic process flows from the graphitic carbon to the Si wafer and the current I_2 produced from the galvanic process flows from the surface of Ag clusters exposed to the etching solution to the Si beneath the Ag clusters. The arrows in Fig. 3.9 indicate the direction of current flow which is opposite to their respective electron flow direction. It should be noted that the fundamental requirement for etching of Si is the removal of bonding electrons from its valance band (or equivalently injecting holes into its valance band). This requirement can be achieved, in the macroscopic electrolytic cell by means of the external current source and in the microscopic galvanic chemical cell, by oxidant H_2O_2. The dissolution of Si that occurs at the microscopic galvanic interface contributes to the etching of Si underneath the Ag clusters, whereas the anodic reaction that happens at the electrolytic interface is the basis for the formation of pores in the Si walls. The occurrence of the repeated site selective Si etching underneath the Ag deposits leads to the vertical intrusion of Ag clusters deep into the Si wafers and the formation of vertically aligned porous SiNWs.

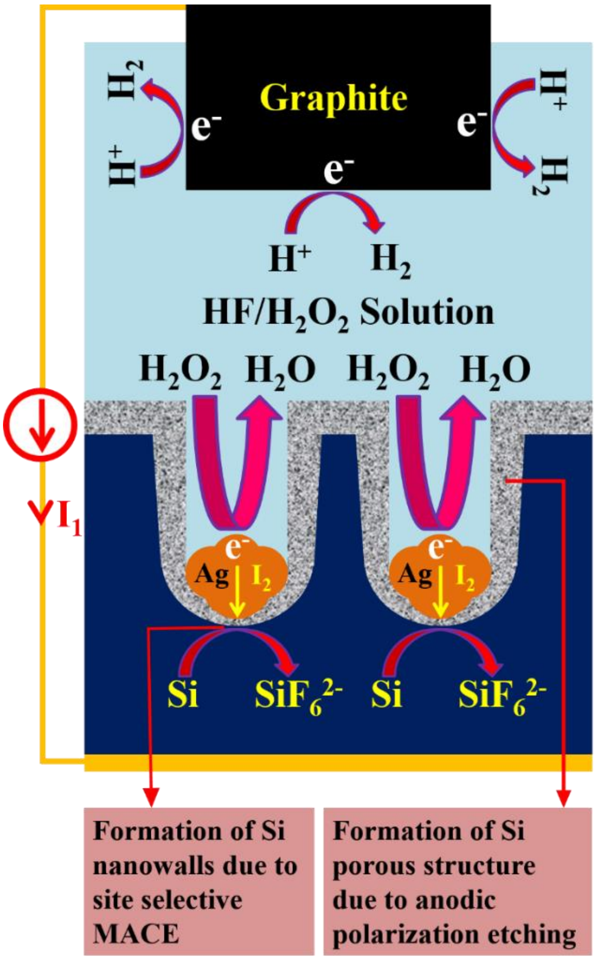

Figure 3.9 Schematic illustration of charge transports during the formation of porous SiNWs. The diagram demonstrates two current paths: I_1 *flows from graphitic carbon to Si wafer by electrolytic charge transfer reaction and* I_2 *flows from Ag clusters exposing to the etching solution to the Si underneath the Ag deposits by a galvanic charge transfer reaction.*

3.4. Summary

The results and inferences of the study are summarized as:

- The facile, low cost galvanic displacement deposition technique was used to prepare uniform interconnected Ag nano-network assembly atop the Si wafer.
- Single crystalline, vertically aligned SiNWs atop the Si were successfully fabricated without destroying the crystallinity and orientation of base Si

wafer. The influence of etching parameter: etching time and H_2O_2 concentration on morphology was investigated. The study reveals that both parameters have almost same effect on morphology and the variation of etching parameters within the range do not destroy the nanowall morphology, but results in the agglomeration of nanowalls at high etching parameters.

- ☞ The lightly doped porous SiNWs were successfully fabricated by modified MACE, where a constant current was applied to the Si wafer through the graphitic carbon. The comparison of porous nanowalls with smooth nanowalls shows that in modified MACE, crystallinity and orientation are retained as in the case of simple MACE.

Chapter 4

Microstructure - property correlations of the fabricated Si nano-architectures

The chapter correlates the microstructure of the MACE fabricated Si nano-architectures with some of its exciting properties such as antireflection, wetting and photoluminescence. The reflectance studies on the solid Si nanowalls (SiNWs), atop the Si wafer, show tremendous reduction in reflectance compared to that of planar Si wafer, in the wide wavelength range (230-1200 nm). The spectral dependence of reflectance, observed in SiNWs obtained at different etching times, exhibit a peculiar behaviour, where reflectance in the long wavelength range (750-1200 nm) decreases and that in short wavelength range (300-750 nm) increases (with a broaden peak like shape), with increase in etching time. Finite-difference time-domain (FDTD) simulation was carried out to explain the observed low reflectance behaviour. The reflectance spectra obtained from FDTD simulation qualitatively matches with the experimental reflectance spectra for low etching time (5 minute etching time) explaining the wavelength dependence of reflectance at low etching time. However, the peculiar behaviour of reflectance at high etching time could not be correlated, which is supposed to be due to the agglomeration of SiNWs. A possible mechanism based on the agglomeration of SiNWs and slight tapering at the top region of SiNWs was suggested to explain the same.

The wetting properties of SiNWs synthesized at different etching times were also studied. It is observed that the SiNWs etched for one minute exhibits a high water contact angle (WCA) of 135° as compared to that of planar Si wafer (67°). As the etching time increases, the contact angle of the SiNWs increased to a maximum of 142°, for SiNWs obtained from 5 minutes etching, and then decreases to a value of 61° for SiNWs obtained at 30 minutes of etching. This reveals that planar Si wafers, when patterned with SiNWs *atop its surface by MACE, exhibit transition from hydrophilicity to near super-hydrophobicity and again back to hydrophilicity, with etching time. The wetting behaviour was successfully explained by considering the observed vertical and agglomerated nature with slight tapering of SiNWs, obtained at low and high etching times respectively.*

The photoluminescence (PL) studies were carried out on both solid and porous SiNWs. It was found that the porous SiNWs exhibit visible PL with peaks at 1.71 and 2.01 eV, whereas the solid nanowalls did not show any visible PL. In order to find the origin of visible PL, other studies viz. temperature dependent PL, Raman scattering, ATR-FTIR and HRTEM were carried out. The studies confirm that the peaks at 1.71 and 2.01 eV originates from Si quantum structures and Si-O-Si bonded amorphous structures respectively. A qualitative correlation of quantum structure size with the PL peak energy is also carried out.

4.1. Introduction

Several research articles have shown exciting properties of MACE prepared Si nanostructures, such as excellent antireflection, surface hydrophobicity / superhydrophobicity and visible photoluminescence [12, 72, 81]. However, reports showing the combined behaviour of excellent antireflection and hydrophobicity, which is beneficial for enhancing the efficiency as well as life time (due to self-cleaning nature of hydrophobicity / superhydrophobicity) of optoelectronic devices like solar cell and photodetectors are very rare. Since highly porous Si nanostructures are achieved from highly doped base Si wafer, the visible luminescence properties are mostly studied in highly doped porous Si nanostructures, and to the best of our knowledge there are no reports on study of visible PL properties of lightly doped porous Si nanostructures prepared by combining MACE with anodic polarization etching. Moreover, the studies correlating the microstructure of the fabricated Si nano-architectures with these properties, which are crucial in view of their favourable applications, are less and needs to be investigated in detail.

Microstructure - antireflection, wetting and photoluminescence property correlations of silicon nanowalls (SiNWs) is another feature of the present study.

4.2. Experimental

The SiNWs and porous SiNWs for the present studies are fabricated by MACE and modified MACE respectively as described in chapter 3.

The microstructure of the prepared SiNWs were studied by LIBRA 200FE Zeiss high resolution transmission electron microscope (HRTEM). A commercial UV-Vis-NIR spectrophotometer (Hitachi UH4150) was used for the surface reflectance study. The contact angle meter (DSA100M, M/s. KRÜSS, Germany) was used for studying the wetting behaviour. The photoluminescence and Raman experiments were carried out using a micro-Raman spectrometer (Renishaw inVia) with an excitation light source of wavelength 514 nm using Ar^+ ion laser with a 10 s data acquisition time. The Raman scattered light and luminescence radiation signals were collected in a backscattering geometry using CCD detector. The laser power was kept at 0.02 mW during the measurements. The temperature dependent PL measurement were carried out on the porous SiNWs in the temperature range 80-375 K using the liquid N_2 cooled low temperature stage (Linkam T95, UK). Resistive heating filament housed underneath the sample in the cryostat was used to maintain the sample temperature during the data collection. Temperature stability during the measurement was typically ±1 K.

4.3. Results and discussions

4.3.1. Antireflection and Raman study of fabricated SiNWs

As shown in the inset of Fig. 4.1 a), the etched portion of Si wafer where nanowall has been formed has a complete black appearance in comparison to that of unetched part. This suggests that the prepared SiNWs exhibit good antireflection behaviour. Therefore, the antireflection behaviour of the fabricated SiNWs were studied. Figure 4.1 a) compares the spectral reflectance of SiNWs, atop the Si wafer etched for different durations, in the wavelength range of 220-1200 nm, with that of planar Si wafer. The reflectance spectrum of planar Si wafer exhibits two maxima at 270 and 370 nm followed by a gradual decrease of reflectance towards higher wavelength up to 1100 nm, after which there is an increase in the reflectance signal. The above wavelength dependence of reflectance agrees well with theoretically calculated reflectance spectrum of Si where the appearance of the two reflection maxima at 370 and 270 nm are ascribed to direct inter-band transitions, E_1 and E_2 [130]. The increase in reflectance from 1100 nm is due to the incorporation of back reflected signal originating from the rear side of Si wafer owing to the band gap of Si at 1107 nm. Importantly, the reflectance spectra of SiNWs atop the Si wafer show a remarkable reduction of reflectance in comparison, to planar Si wafer. Moreover, the spectral dependence of reflectance of SiNWs is quite different from that of planar Si wafer and also differs for SiNWs obtained at different etching times as shown in Figs. 4.1 b, c) for different wavelength ranges. Fig 4.1 b, c) depicts that the reflectance observed in SiNWs decreases with increase in etching time at long wavelength range (750-1200 nm) with a slight increase for 30 minutes etched SiNWs. Whereas at short wavelength range (300-750 nm), the reflectance increases with a broaden peak like shape especially for samples obtained with 15 and 30 minutes of etching. The reduction in reflectance are generally explained based on the following factors [11, 131-133]; (i) graded-index coating model whose mechanism resembles to that of the multilayer anti-reflection coating model, (ii) multiple light scattering within the nanostructure network, which substantially increase the path length of incident light to several orders of magnitude higher than the thickness of the nanostructures, and hence leads to complete light trapping (iii) high-index nanostructures placed on semiconductor surfaces reduce the reflectivity by capitalizing on optical Mie resonances .

The morphological studies of the SiNWs, by using SEM (Fig. 3.4, chapter 3), reveal that the wall thickness of SiNWs, as well as the interspacing between the nearest neighbour nanowalls, are smaller than the wavelength of incident radiation (220-1200 nm). Also, it is confirmed from both SEM and TEM analysis (Fig. 3.4 and 3.6, chapter 3) that the SiNWs are free of pores and have nearly uniform thickness throughout its height. Therefore, according to the effective medium theory [134], such a system of SiNWs atop the Si wafer will be characterized by a constant intermediate refractive index (n) between that of air and Si in the vertical direction as illustrated in Fig. 4.2. Such a constant intermediate refractive index can reduce the reflectance only up to certain extent for some specific wavelengths. This reveals that the graded-index coating model is not the appropriate to explain the observed broadband low reflectance in SiNWs.

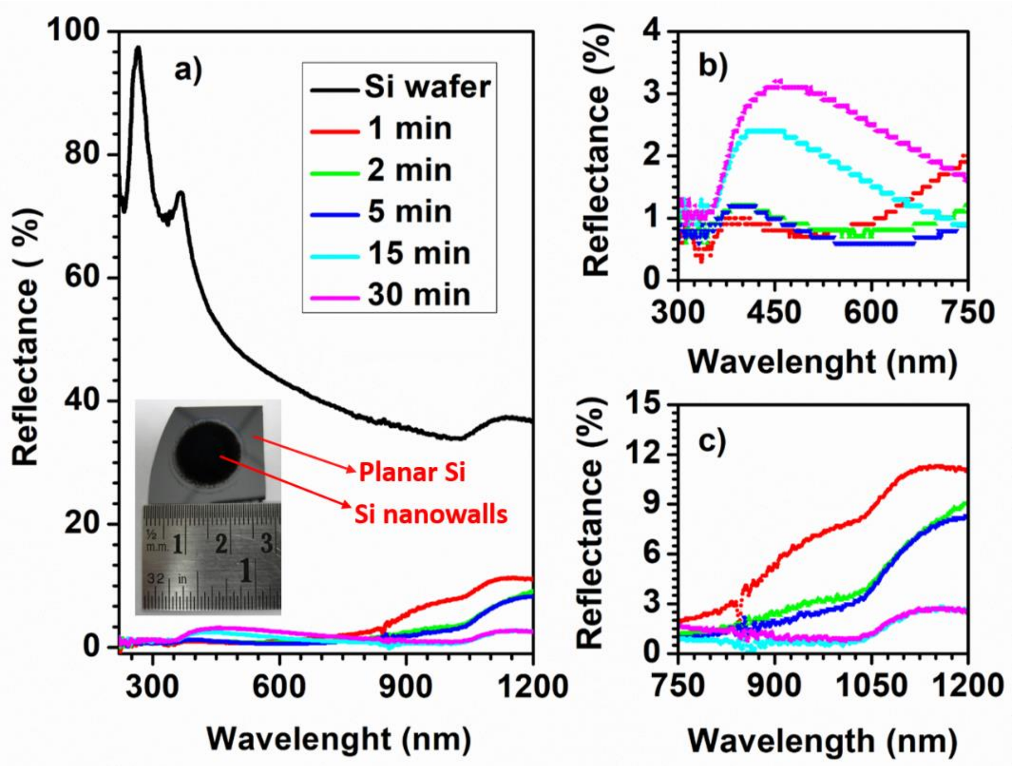

Figure 4.1 a) Spectral reflectance of planar Si wafer and SiNWs atop the Si wafer obtained at different etching times. b, c) Enlarged view of the reflectance spectra of SiNWs depicted in figure 1 a), at short wavelength (300-750 nm) and long wavelength (750-1200 nm) range respectively. The reflectance spectra represented in different colours in figures b, c) corresponds to the reflectance spectra of Si nanowalls obtained at different etching time.

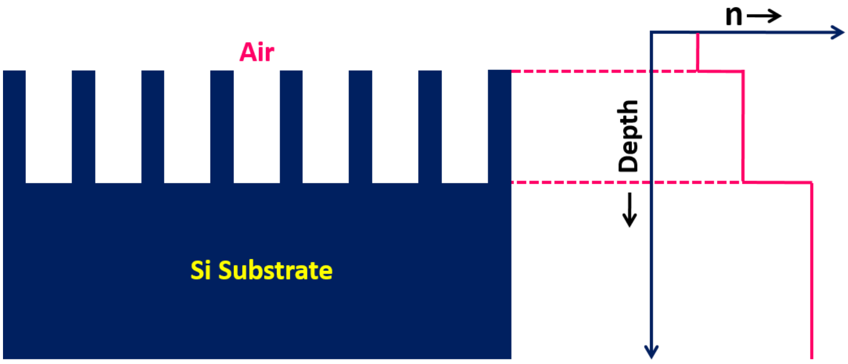

Figure 4.2 Schematic illustrating that SiNWs are characterized by a constant intermediate refractive index (n) between that of air and Si, in the vertical direction.

Owing to the size region of the fabricated SiNWs systems as discussed above, it is required to solve the Maxwell's equations to explain the light trapping behaviour of the present system. Therefore, we tried to carry out FDTD simulation which is a time-domain numerical method that solves the Maxwell's equations with appropriate boundary conditions. Before performing the simulation, it is worth to discuss the complication offered by the present SiNWs system and the simplifications needed to perform the simulations. The prepared SiNWs are surface relief structures atop the Si wafer that has been formed by etching the 500 µm thick Si wafer, whose heights are approximately 800, 1150, 1800, 4700 and 9350 nm for 1, 2, 5, 15 and 30 minutes etching time respectively (Fig. 3.4, chapter 3). Performing simulations of the above surface relief structures having such heights with 500 µm thick Si requires more computation time and larger memory. Therefore, we choose the thickness of silicon substrate equal to 2330 nm which is comparable to the thickness of the thin film silicon solar cell and also has been adopted by other researchers [135, 136]. So for 800, 1150, 1800 nm high SiNWs, the thickness of Si substrate was used to be 1530, 1180 and 530 nm respectively and for 4700 and 9350 nm high SiNWs (height being higher than 2330 nm), the thickness of Si substrate was used to be 530 nm (same as that for 1800 nm high SiNWs) for comparison. Moreover, the present SiNWs system (Fig.3.4, chapter 3) comprises of complicated nanowall structures with random dimensions, as well as internanowall spacing. All these factors are quiet difficult to handle in FDTD solution software which will restrict, one to apply the boundary conditions requiring very high memory and computation time. Therefore, for simplicity we choose an S-shape wall like structures for our prepared nanowall, to perform the FDTD simulations whose geometry is demonstrated in the inset of Fig. 4.3. The FDTD simulations were carried on this S-shaped SiNWs for different periodicity (P), heights (H) and thickness (T) as well as for disorder system (combined system of different thickness) with appropriate boundary conditions. The range of such various factors are chosen following the SEM micrographs of SiNWs (Fig. 3.4, chapter 3) and it is also worth to note that, while varying the thickness of the S-shape SiNWs, its shape changes as illustrated in Fig. 4.3, which accounts the random structure of the prepared SiNWs. A plane wave source with both electric and magnetic polarizations under normal incidence was used in the simulations. The details of the simulations are described in the Fig. 4.4. For X, Y- direction, periodic boundary condition and for Z-direction, perfectly matched layer were chosen in the simulation. A plane wave light source was set 100 nm above the nanowall. A frequency-domain field and power monitor was placed 100 nm above the light source to detect reflection.

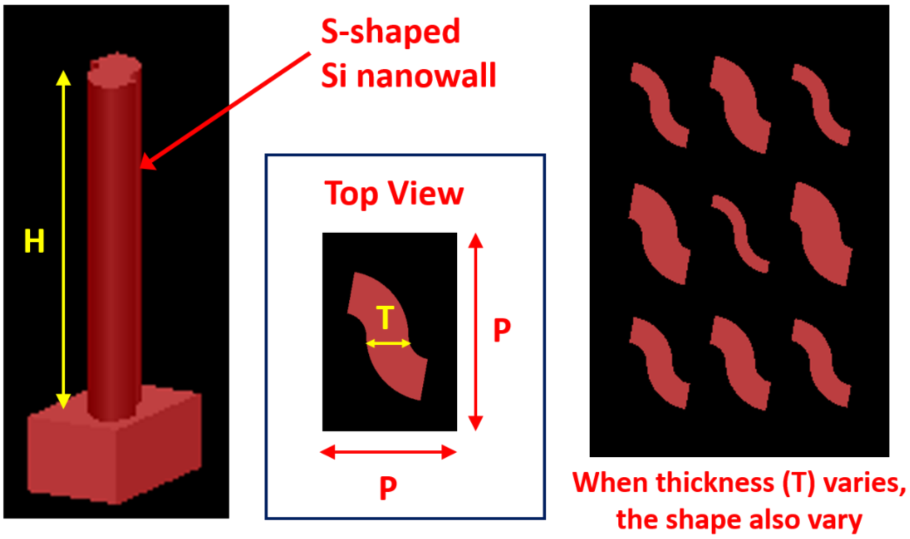

Figure 4.3 Description of S-shaped SiNW and the various simulation parameters.

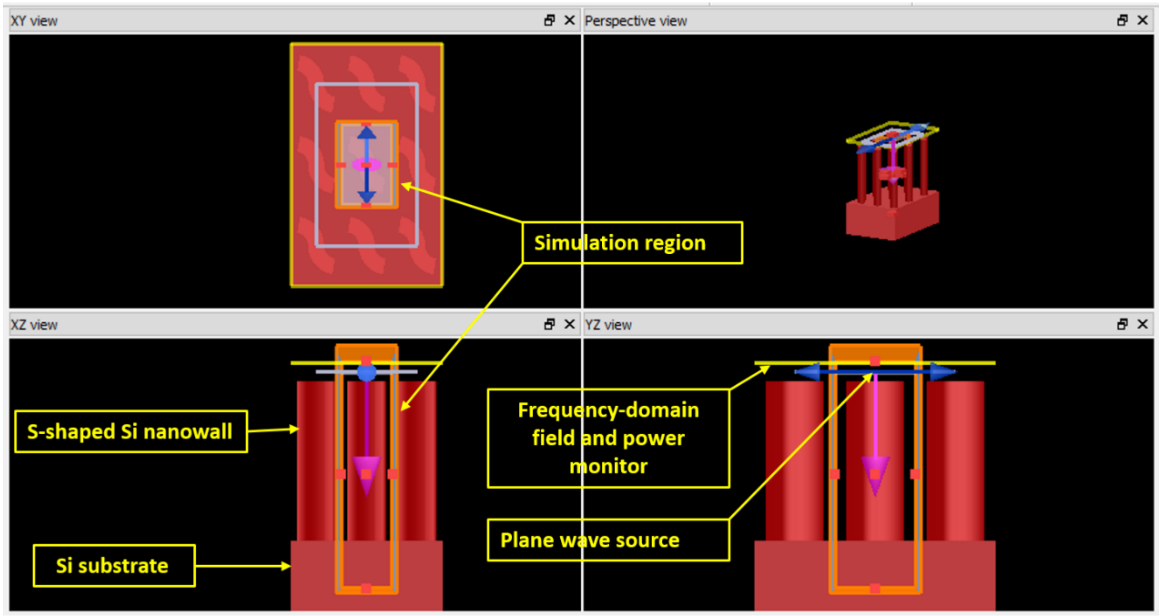

Figure 4.4 View of FDTD simulation where the source, monitor and simulation regions are demonstrated.

Fig. 4.5 summarizes the simulated reflectance spectra of the S-shaped SiNWs for the different factors. The simulated reflectance spectra of 80 nm wall thickness, 1800 nm height and 250 X 400 nm x nm periodicity are shown in Fig 4.5 a) for transverse electric (TE), transverse magnetic (TM) polarized and unpolarized (no name) light source. The spectra for unpolarized light is calculated by taking average of that of transverse electric and transverse magnetic polarized light. The spectra represented without any specification will be considered as that for unpolarized light. The same was also found out for planar Si (thickness of 2330 nm) for comparison. It is observed that the S-shape SiNWs exhibit significant lower reflectance value as well as different reflectance behavior for transverse electric and transverse magnetic polarization compared to that of planar Si. Such polarization sensitive behavior of S-shape SiNWs is ascribed to its peculiar architecture. Moreover, the reflectance spectra show quiet oscillating features which are believed to originate from the interference of radiation throughout the three-dimensional nanostructures with the periodicity matching [137]. The effect of periodicity (P) on the reflectance behaviour was also simulated for the s-shaped SiNWs for a height of 1800 nm and thickness of 80 nm as shown in Fig. 4.5 b). It

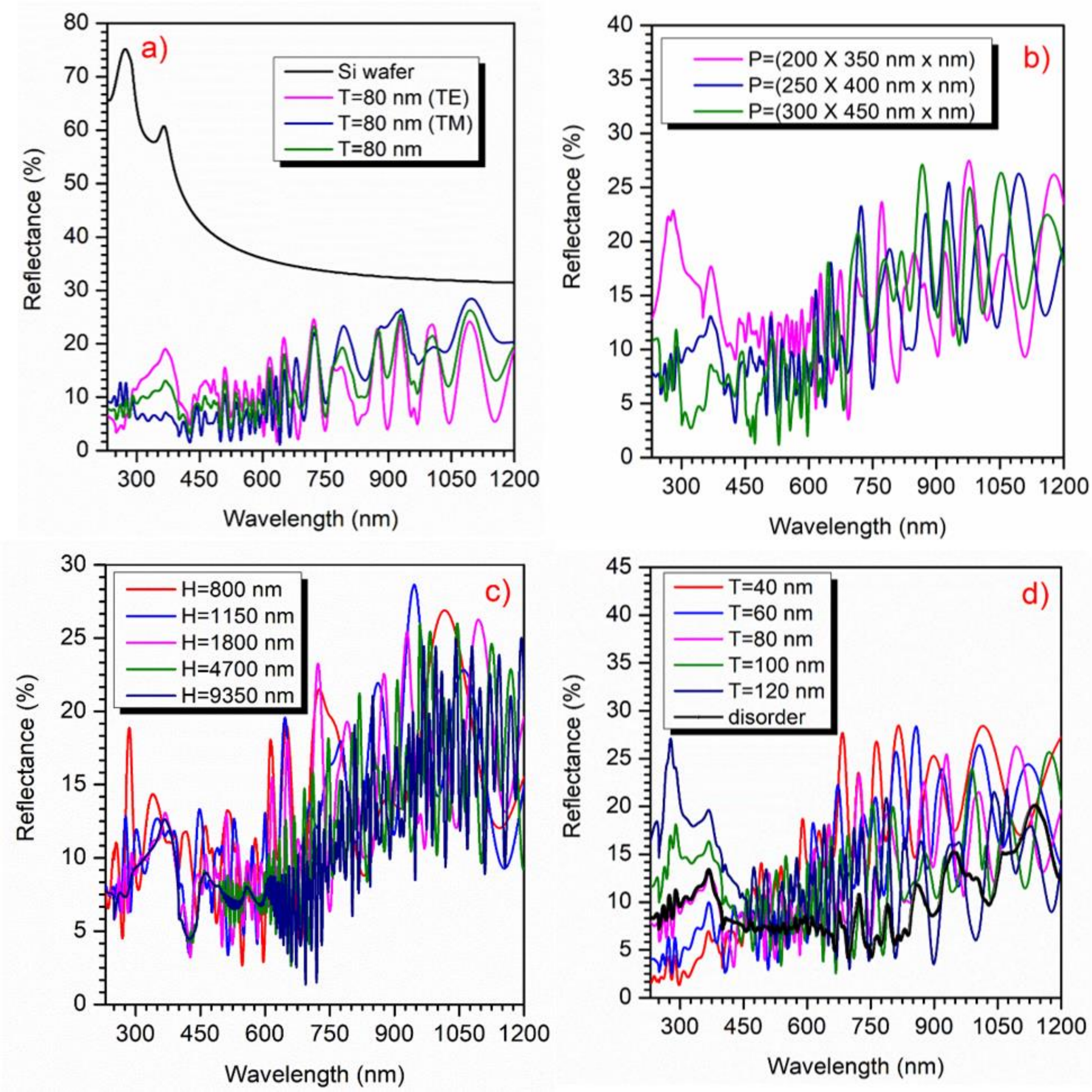

Figure 4.5 Simulated reflectance spectra of the S-shaped SiNWs. a) For 80 nm wall thickness, 1800 nm height and 250 X 400 nm x nm periodicity with transverse electric (TE), transverse magnetic (TM) polarized and unpolarized (no name) light as well as for planar Si (thickness of 2330 nm). b) For height of 1800 nm and thickness of 80 nm with different periodicity (P). c) For wall thickness of 80 nm and periodicity of 250 X 400 nm x nm with different height (H). d) For 1800 nm height and 250 X 400 nm x nm periodicity with different thickness (T) and disorder structure (combined system of 9 different thickness i.e. 40, 50, 60, 70, 80, 90, 100, 110, 120 nm)

is observed that S-shaped nanowall with low periodicity shows higher reflectance at short wavelength range (<700 nm) whereas nanowall with high periodicity exhibits slightly higher reflectance at long wavelength range (> 700 nm). The higher reflectance at short wavelength for low periodicity is due to the higher surface reflectance from the top surface of nanowalls. The slight higher reflectance at long wavelength for high periodicity can be ascribed to the insufficient absorption of nanowall (owing to indirect nature of Si band gap), as a result the incident light will reach the nanowall/substrate interface giving rise to some reflectance. The simulated reflectance spectra demonstrating the effect of nanowall height (H) on reflectance of S-shaped SiNWs with wall thickness of 80 nm and periodicity of 250 X 400 nm x nm are shown in Fig. 4.5 c). It is seen that the reflectance behaviour has no significant change with the variation in nanowall height. However, our experimental result shows significant variation in reflectance with nanowall height. But it is worth noting that in our prepared nanowall, with increase in height, the SiNWs gradually get agglomerated (Fig. 3.4, chapter 3), which was not considered in the simulation because of the difficulty in the FDTD simulation, while incorporating the agglomeration. This suggests that the observed experimental reflectance behaviour with different etching time might be due to the agglomeration of the nanowalls. Moreover, the effect of wall thickness (T) on the S-shaped SiNW along with disorder structure (combined system of 9 different thickness i.e 40, 50, 60, 70, 80, 90, 100, 110, 120 nm) for 1800 nm height and 250 X 400 nm x nm periodicity was also investigated, as depicted in Fig. 4.5 d). For the disorder structure, eight simulations were conducted with interchanging the position of nanowalls and the average of all was shown in the Fig. 4.5 d). It is observed that with increase of thickness of nanowall, the reflectance increases at short wavelength (< 700 nm) and decreases slightly at long wavelength range (> 700 nm). This behaviour is similar to that observed with the periodicity of nanowall and can be ascribed to the same reason. However, the reflectance spectra of the nanowall with disorder structure shows an interesting behaviour exhibiting low reflectance behaviour at short and long wavelength range with less oscillating behaviour. Such a compromising behaviour of reflectance in the whole wavelength range can be ascribed to the fact that, nanowall with a single thickness exhibit Mie resonance for specific wavelength whereas a system of nanowalls of different thickness exhibits resonance at several wavelengths and broadens the wavelength range of resonance. Therefore, the reflectance behaviour of disorder structure exhibits lower reflectance over the whole wavelength spectrum. The reflectance behaviour of such disorder structure was compared with the experimental reflectance spectrum of prepared SiNW with same height (1800 nm; sample obtained at 5 minute etching time) in Fig. 4.6. It is observed that the spectral reflectance behaviour of experimental spectrum quiet match with simulated reflectance spectrum though the reflectance value of simulated spectrum is high (with a value of around 7 as shown in the black curve in Fig. 4.6). The lower experimental reflectance value is due to the fact that the fabricated SiNWs are of somewhat random structure. These random structures are difficult to handle in the simulation and for simplicity we have taken S-shaped SiNWs. However, it is revealed from Fig. 4.6 that the disorder system qualitatively explains the reflectance behaviour of fabricated SiNWs. Moreover, although the simulated reflectance spectra did not explain the experimental reflectance behaviour with etching time, the increase in reflectance with a broad peak like shape with increase of etching time (especially for 15 and 30 minutes etching time, Fig. 3.4, chapter 3) can be explained by considering reflectance study of silicon nanowires by Hung et al. [56] and reflectance study of graded-density surfaces by Branz et al.[138]. According to Hung et. al, the reflectance peak may be due to the optical crossover feature between enhanced optical scattering inside the material and increased optical absorption coefficient of silicon (jumps at around 400 nm of wavelength for crystalline silicon). On the other hand, Branz et al., ascribed it to be likely due to the development of larger-scale surface features that scatter incident short wavelength light. In the present fabricated SiNWs, the SiNW prepared with higher etching time can have some tapering at the top due to the longer exposure into the etching solution, so they can be considered graded-density surface. Also, the nanowall at higher etching time are agglomerated at the top which results larger-scale features (Fig. 3.4, Chapter 3). This is described in Fig. 4.7.

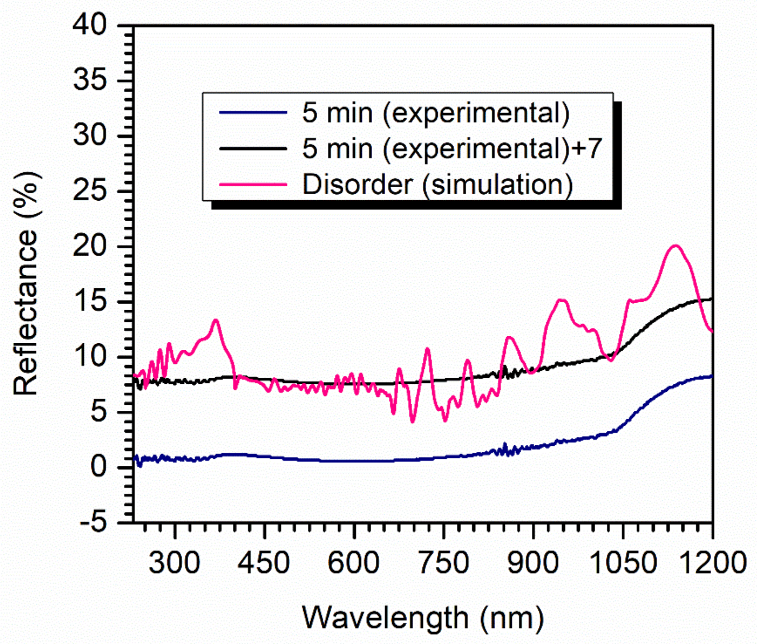

Figure 4.6 Comparison of simulated reflectance behaviour of disorder structure (pink colour curve) with the experimental reflectance spectrum of prepared SiNW with same height (1800 nm; sample obtained at 5 minute etching time (navy colour curve)). The black colour curve denotes the experimental reflectance spectrum with its reflectance value increased by 7.

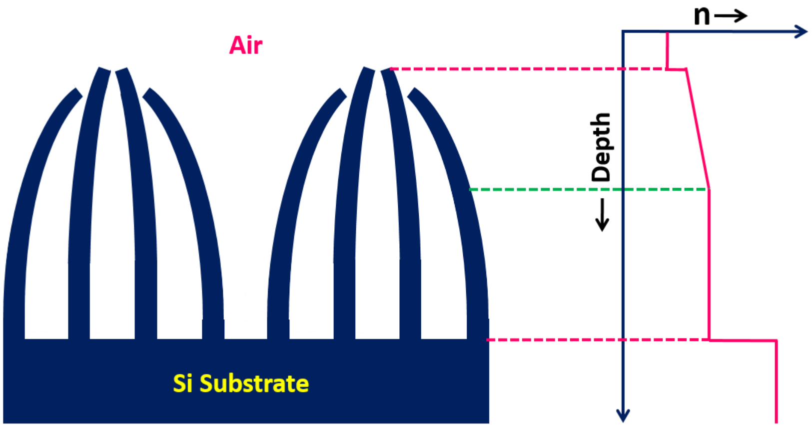

Figure 4.7 Schematic showing the congregation and tapering at the top region of SiNWs etched for higher etching time which leads to the gradual change of refractive index at that region.

The Raman scattering study was carried out on both SiNWs etched for different etching time and planar Si wafer in order to study the effect of reduction of reflectance on the scattering intensity as shown in Fig. 4.8. It is observed that both planar Si and SiNWs exhibit a sharp peak at 520 cm^{-1} which is assigned to the first-order optical phonon scattering in crystalline Si [139]. The analysis of Raman spectra reveals that both the peak position and line shape do not show any significant variation with etching time which suggests that the etching process does not affect the crystalline nature of Si. However, the Raman scattering intensity shows an enhancement of around one order of magnitude higher for the SiNWs as compared to that of planar Si wafer. Also, as the etching time increases, the scattering intensity increases initially and then decreases, with a maximum for 5 minute etching time as depicted in the inset. Since etching reduces the volume fraction of Si and hence the scattering volume, such a significant enhancement in scattering intensity claims

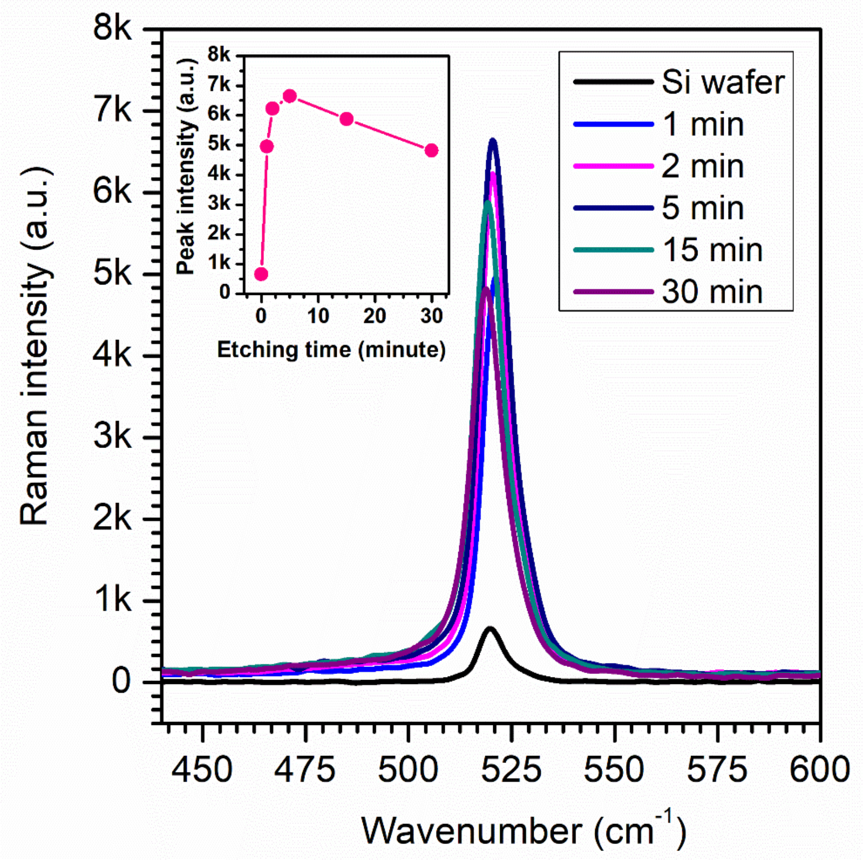

Figure 4.8 Raman spectra of Si wafer (planar) and Si etched for different durations. The inset in the figure shows the variation of Raman peak intensity as a function of etching time. In the inset, zero minute in the x-axis corresponds to the Raman intensity of planar Si wafer.

to an optical effect. The reduction of reflectance for SiNWs leads to an increase of light intensity entering the sample. Moreover, the Raman back scatter traveling towards the surface encounters the SiNWs, resulting in an additional enhancement factor for light excitation. The observed increasing and decreasing behaviour of scattering intensity with etching time with a maximum for 5 minutes etching time can be understood by considering that the wavelength of excitation radiation for Raman scattering for the present study is 514 nm and at this wavelength, the reflectance shows an almost opposite behaviour to that of scattering intensity, with etching time (Fig. 4.1). Therefore, the lowest reflectance for 5 minutes etched SiNWs at 514 nm, causes the highest Raman scattering. This reveals that Raman scattering behaviour agrees well with the reflectance behaviour in SiNWs.

In order to find out the most effective SiNWs among the SiNWs obtained by metal assisted etching for different periods of time, for solar cell application, solar-weighted reflectance (R_{sw}) was calculated, as depicted in Fig. 4.9, for the standard solar radiation spectrum (the terrestrial air mass 1.5 global (AM 1.5G)) using the following expression [140, 141],

$$R_{sw} = \frac{\int_{280}^{1107} R(\lambda) N_{photon}(\lambda) d\lambda}{\int_{280}^{1107} N_{photon}(\lambda) d\lambda} \tag{4.1}$$

Where $R(\lambda)$ is the spectral reflectance of SiNWs and $N_{photon}(\lambda)$ is the photon number of AM 1.5 G per unit area per unit wavelength. The lower and upper limit of integration is taken as the lowest wavelength, 280 nm of AM 1.5 G and wavelength corresponding to band gap value, 1107 nm of Si. The results are summarized in Fig. 4.9. It is observed that R_{sw} decreases tremendously for the etched SiNWs in comparison to that of planar Si wafer. However, a closer look at R_{sw} for SiNWs etched for different time, shown in the inset of Fig. 4.9, reveals that R_{sw} value decrease at the beginning up to five minutes of etching (minimum value of 1.27 %), followed by an increase with further etching . Such a decreasing and increasing behaviour with etching time can be attributed to the peculiar wavelength dependence of reflectance spectrum on etching time (Fig. 4.1) as well as the strong wavelength dependence of the standard solar spectrum (AM 1.5G). SiNWs obtained by etching for 5 minutes showing the lowest reflectance at shorter wavelength and an intermediate reflectance at longer wavelength results in the minimum value of R_{sw}. This suggests that SiNWs obtained after 5 minutes of etching has the optimum property to be used as an antireflection layer for solar cell application.

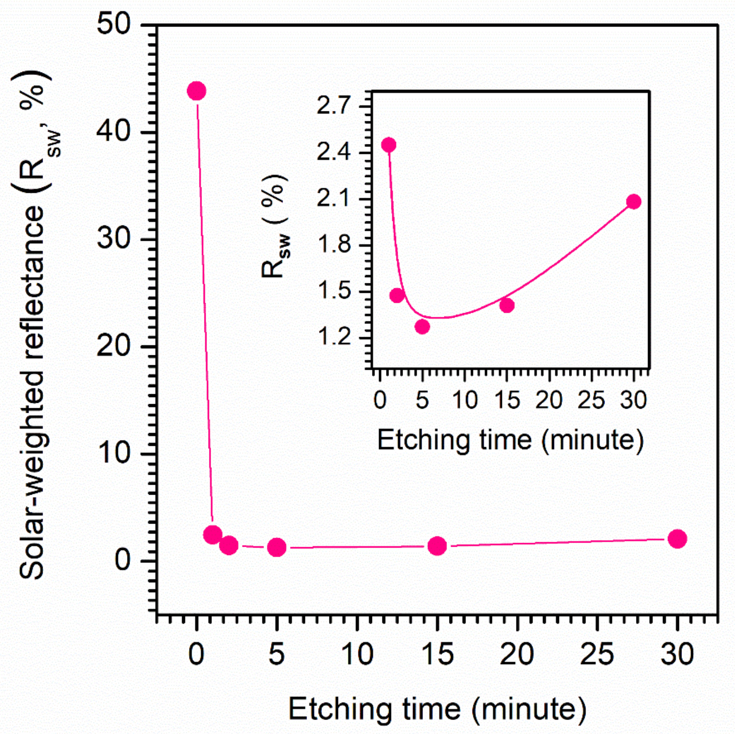

Figure 4.9 Solar-weighted reflectance (R_{sw}) of planar Si wafer and SiNWs obtained at different etching time. The data at zero minute etching time corresponds to planar Si wafer. The inset shows the enlarged view of R_{sw} verses etching time indicating that R_{sw} value exhibits a minimum at 5 minutes etching with a value of 1.27%.

4.3.2. Wetting properties of SiNWs

The wetting properties of the fabricated SiNWs, as well as the planar Si wafer, were studied by performing the contact angle measurements. The results obtained are summarized in figure 4.10. The photograph of water droplets sitting on the planar Si wafer and SiNWs etched for 1, 2, 5, 15 and 30 minutes are depicted in the inset. It is seen that the SiNWs etched for one minute exhibits a high contact angle of 135° as compared to that of planar Si wafer (67°). As the etching time increases, the contact angle of the SiNWs increases to a maximum of 142° for SiNWs obtained from 5 minutes etching and then decreases to a value of 61° for SiNWs obtained at 30 minutes of etching. This reveals that planar Si wafer, when patterned with SiNWs atop its surface by metal assisted chemical etching, exhibits transitions from hydrophilicity to near super-hydrophobicity and again back to hydrophilicity with etching time.

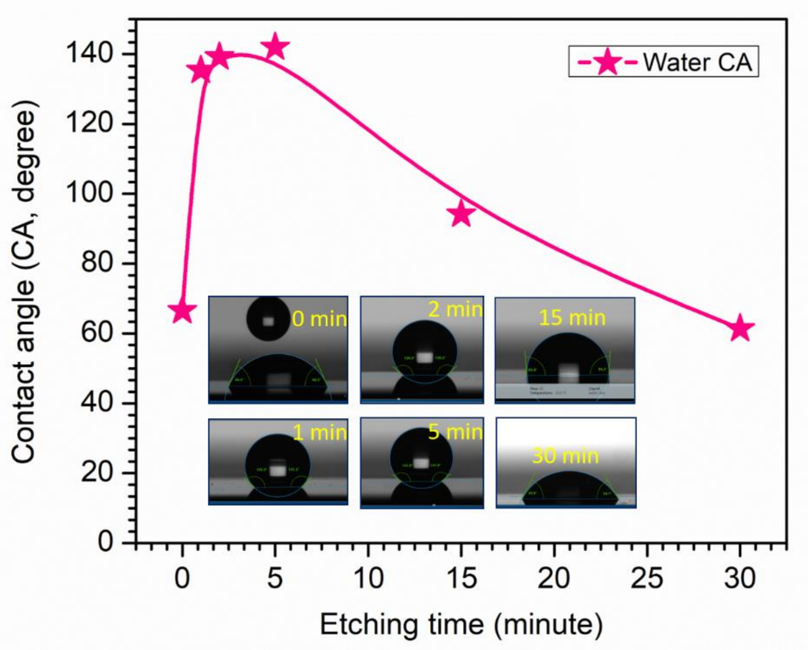

Figure 4.10 Plot of water contact angle (CA) versus etching time. The inset shows the photograph of water droplet on planar Si wafer (0 minute etching time) and SiNWs etched for 1, 2, 5, 15, 30 minutes respectively. The etching times are mentioned in each photograph.

In order to get some insight regarding the observed behaviour of SiNWs, we performed the contact angle measurement on both Si wafer and SiNWs etched for different time with another nonpolar liquid, diiodomethane and calculated the surface energy as depicted in Fig. 4.11. Fowkes model which is the most widely used two component model

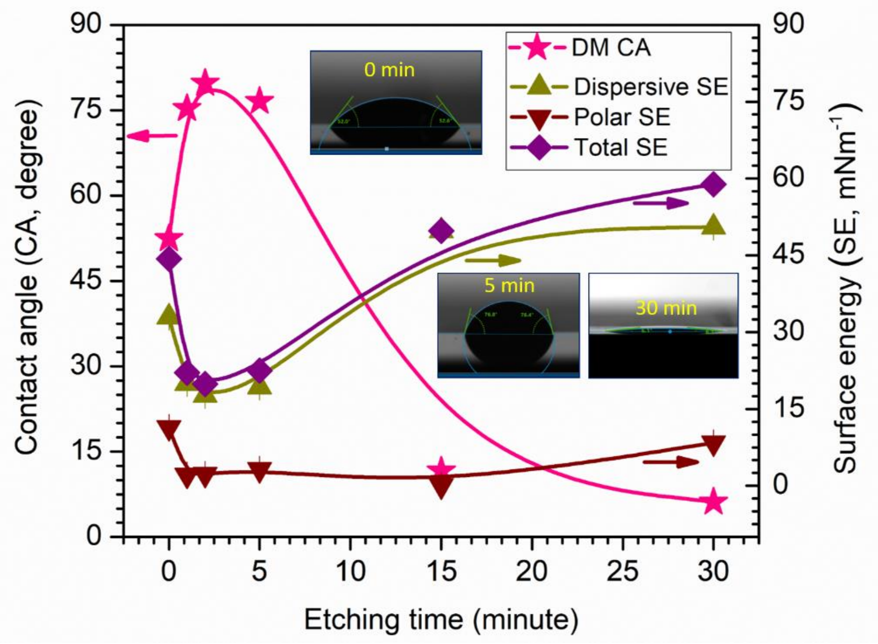

Figure 4.11 Shows the diiodemethane (DM) contact angle (CA) and surface energy (SE) versus etching time. The inset shows the photograph of diiodemethane droplet on planar Si wafer (0 minute etching time) and SiNWs etched for 5 and 30 minutes. The time mentioned in each photograph corresponds to their etching time.

to determine the surface energy of solids by measuring the contact angle using two liquids (one polar and nonpolar), was chosen to calculate the surface energy. It basically combines the Young and Young-Dupree equations and separates the surface energy into its polar and dispersive (nonpolar) components. It is given by [142, 143],

$$\gamma_l(\cos\Theta + 1) = 2[(\gamma_l^d)^{\frac{1}{2}}(\gamma_s^d)^{\frac{1}{2}} + (\gamma_l^p)^{\frac{1}{2}}(\gamma_s^p)^{\frac{1}{2}}] \qquad (4.2)$$

Where Θ is the contact angle of liquid on solid surface. γ_l^d and γ_s^d are dispersive component of surface energy of liquid and solid respectively. γ_l^p and γ_s^p are polar components of surface energy of liquid and solid respectively. γ_l ($\gamma_l = \gamma_l^p + \gamma_l^d$) is the total surface energy of liquid. The two unknown (γ_s^d and γ_s^p) can be found out from this equation by measuring the contact angle, Θ for two liquids with known values of their γ_l^d and γ_l^p. With the measured value of contact angle on Si wafer and SiNWs with different etching time for both polar liquid, water ($\gamma_l^p = 51.0$ mNm^{-1}and $\gamma_s^d = 21.8$ mNm^{-1}) and nonpolar liquid, diiodemethane ($\gamma_l^p = 0$ mNm^{-1}and $\gamma_s^d = 50.8$ mNm^{-1}), the respective γ_s^d, γ_s^p and γ_s ($\gamma_s = \gamma_s^p + \gamma_s^d$) values were calculated for Si wafer and SiNWs etched for different time, and plotted as a function of etching time as shown in Fig. 4.11. It is observed that as the etching time increases, the total surface energy along with its dispersive and polar component decreases followed by a significant increase for higher etching time. Since the Si wafer and SiNWs etched for different time have almost the same surface chemistry, the observed low and high surface energy of SiNWs etched for lower and higher etching time respectively, can be ascribed to the surface morphology [142, 144]. The surface morphology of SiNWs obtained at different etching time (Fig. 3.4, chapter 3) reveals that SiNWs prepared at lower etching time are vertical with an overall uniform inter-separation whereas the SiNWs, prepared at higher etching time, congregated at the top resulting in a somewhat distorted morphology with both higher and lower inter-separation. Also, the top region of SiNWs obtained at higher etching time may have a tapered morphology due to its higher exposure to etching solution. The strange wetting behaviour observed in the prepared SiNWs can be understood by considering both the Wenzel and Cassie–Baxter models [145, 146], used for studying the wetting behaviour of structured surfaces as well as the Laplace equation describing the pressure drop at curved interfaces [147, 148], as summarized briefly below.

According to Wenzel model, the liquid penetrates the surface crevices and fully contacts the structured surfaces. The equation describing the Wenzel model is given by,

$$cos\,\Theta_W = rcos\,\Theta \qquad (4.3)$$

Where Θ_W is the apparent contact angle measured on structured surface, r is the roughness factor, defined as the ratio of actual surface area to that of projected surface area and Θ is the measured contact angle on an analogous flat surface. This predicts that a structured surface will be more hydrophilic if its analogous flat surface is originally hydrophilic and vice versa.

In Cassie-Baxter models, the liquid is assumed to sit on the top asperities of the structured surface with air being trapped into the crevices. The Cassie-Baxter model is represented by the following equation,

$$cos\,\Theta_{CB} = f_s\,cos\,\Theta - 1 + f_s \qquad (4.4)$$

Where Θ_{CB} is the apparent contact angle measured on the structured surface and f_s is the solid fraction that is in contact with liquid. This explains the hydrophobic behaviour of structured surface from its analogous flat surface with hydrophilicity.

The Laplace equation describing the pressure difference (ΔP) across the liquid-vapour interface is given by,

$$\Delta P = \frac{2\gamma}{r} \qquad (4.5)$$

Where r is the radius of curvature of the surface of liquid. This equation predicts that a higher pressure difference across the liquid-vapour interface corresponds to a smaller radius of curvature.

Now we can describe the wetting behaviour of SiNWs atop its Si wafer as shown schematically in Fig. 4.12. Figure 4.12 a) depicts the array of vertical SiNWs holding the liquid (water) where the radius of curvature (r) of the water is governed by separation distance (d_1) among the SiNWs. So SiNWs with an inter-separation distance greater than d_1 will have a greater radius of curvature than r and hence can not support the same pressure difference across water-vapour interface according to equation 4.5 and will result in the penetration of water into the interstices of SiNWs. The SiNWs obtained at low etching time being vertical with an overall uniform and lower inter-separation distance, is capable of holding the water droplet and can be described by the schematic model in Fig. 4.12 a). So the Cassie-Baxter models (equation (4.4)) will be used to address the wetting behaviour of

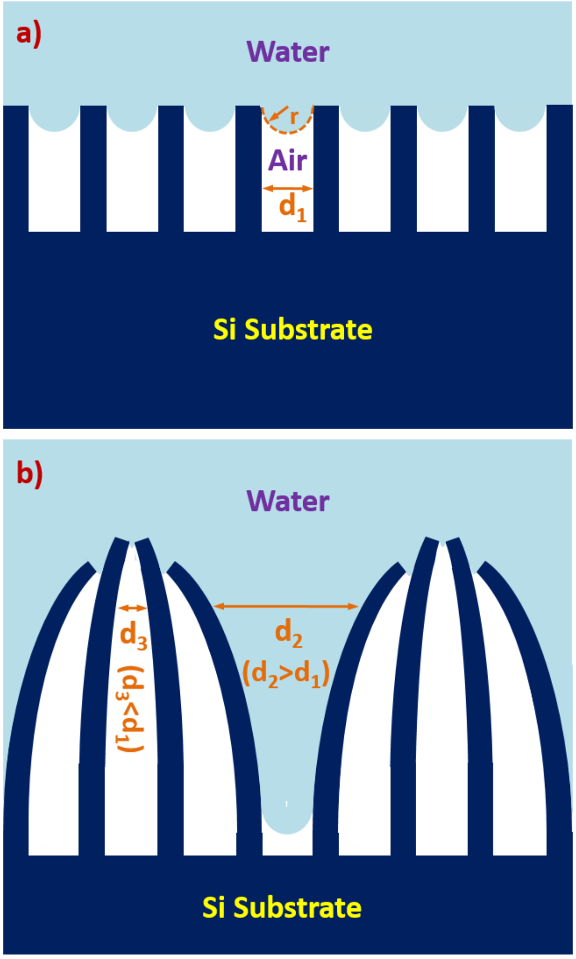

Figure 4.12 Schematic description of wetting behavior of SiNWs obtained at different etching times. a) Illustrate that SiNWs separated with a small distance (d_1) *can hold the water droplet with a radius of curvature (r). b) Depicts that aggregation and tapering of SiNWs at the top region result in both higher inter-separation distance,* d_2 *and lower inter-separation distance,* d_3 *than* d_1*. The region with lower inter-separation distance* (d_3) *holds the water droplets whereas in the region with higher inter-separation distance* (d_2)*, water penetrates the interstices of SiNWs*

SiNWs obtained at lower etching time. It explains the transition from hydrophilic behaviour of flat surface to the hydrophobic behaviour of structured surface. Considering the observed congregation of the top region of SiNWs etched for higher time and the tip tapering, its wetting behaviour can be understood by referring to Fig. 4.12 b). The congregation and tapering at the top region of SiNWs result in both the increase of inter-separation distance from d_1 to d_2 and the decrease of inter-separation distance from d_1 to d_3. So according to equation (4.5), the region of SiNWs with inter-separation distance d_3 can hold the water whereas, for the region of SiNWs with inter-separation distance d_2, the water will penetrate the interstices of SiNWs as shown schematically in Fig. 4.12 b). So the wetting behaviour of such distorted morphology will be explained by using both Wenzel and Cassie-Baxter model. Therefore, depending on the percentage of region obeying the Wenzel and Cassie-Baxter model, the contact angle can be greater and lesser than that of flat Si wafer. The height of SiNWs etched for 15 minutes is lower (by a factor of ~2) than that of 30 minutes etched SiNWs (Fig. 3.4, chapter 3), so the contact area between Si and water will be lesser for 15 minutes etched SiNWs than that of 30 minutes etched SiNWs. Hence the contribution of Wenzel model for 30 minutes etched SiNWs will be higher than that of 15 minutes etched SiNWs which will result lower contact angle for 30 minutes etched SiNWs. This explains the contact angle value of 94° and 61° for 15 and 30 minutes etched SiNWs compared to that of 67° for Si wafer.

4.3.3. Photoluminescence properties of porous SiNWs

The room temperature photoluminescence (PL) spectrum of the porous SiNWs, compared with that of pore free SiNWs and the planer Si wafer is shown in Fig. 4.13. Curve fitting with Gaussian function discloses that the room temperature PL spectrum of porous SiNWs can be de-convoluted into two Gaussian profiles with high intense peak maxima $E_{PL1} \sim 1.71$ eV and low intense peak maxima E_{PL2} at 2.01 eV. In contrast, the visible emission peaks that exist in porous SiNWs, are found to be absent in both pore free SiNWs and planar Si wafers. The origin of visible emission was studied by Sham et al. [149], from the synchrotron-light-induced optical luminescence and found that quantum size effect originated from the Si nanostructures gives optical transition, and hence luminescence. The TEM studies of porous SiNWs (Fig. 3.8 c), chapter 3) reveals that the mean dimension of the distributed pores and inter-pore Si regions is close to the reported Bohr radius value

~4.3 nm for free-exciton in Si crystals [150]. Since the dimension of pores and inter-porous Si region evolved in porous SiNWs is found to be closer to the theoretical quantum size limit, it can be considered that majority of the visible PL emission signals in the porous SiNWs originate from the confinement of charge carriers in Si quantum structure.

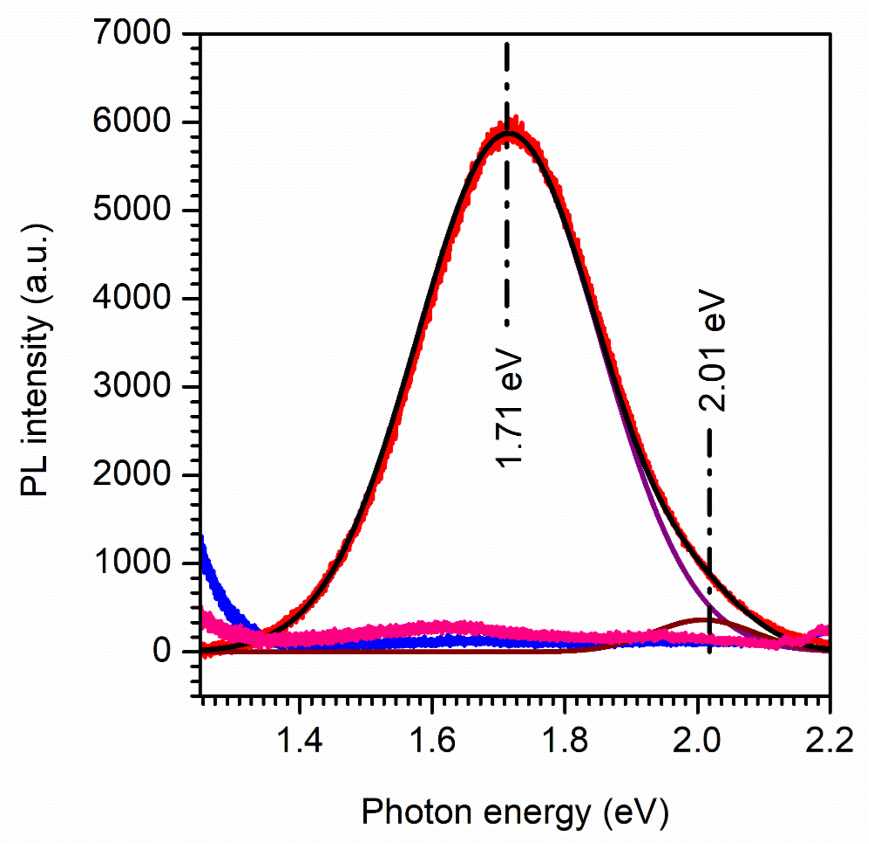

Figure 4.13 Room temperature PL spectra of porous SiNWs (red curve), pore free SiNWs (pink curve) and planar Si (blue curve). The fitted PL spectrum of porous SiNWs has two Gaussian profiles with peak maxima 1.71 (E_{P1}) and 2.01 eV (E_{P2}) as indicated by the dashed lines.

The Raman spectra of porous SiNWs and bulk Si in the range 470–550 cm^{-1} are depicted in Fig. 4.14. The notable feature present is a single strong first-order Raman scattering profile of Si [151]. It is observed that the Raman line position of porous SiNWs is down shifted by 2.8 cm^{-1} in comparison to that obtained for bulk Si wafer. In addition, the full width at half maximum (FWHM) value 9.62 cm^{-1} deduced from the fitting of the

Raman spectrum of porous SiNWs using pseudo-Voigt function is ∼2 cm^{-1} larger compared to 7.56 cm^{-1} obtained for bulk silicon. Similar redshift and asymmetry broadening in the Raman line were observed previously on porous Si [152, 153]. Moreover, no Raman line was observed in the range 470-490 cm^{-1}, indicating the absence of amorphous Si structure in porous SiNWs [153]. According to literature reports, the observed downward shift and asymmetric broadening in the Raman scattering profile may have different origin viz., strain in the lattice, inhomogeneous laser heating and electron-phonon interaction (also called Fano interaction) and phonon confinement in nanostructures [152, 154]. The results obtained from the analysis of inverse FFT pattern from HRTEM images (Fig. 3.8 c), chapter 3) indicated that porous SiNWs are single crystalline without any measurable lattice strain. The low laser power (0.02 mW) used for the Raman measurements neglect the inhomogeneous laser heating effect. Additionally, electron-phonon interaction does not exist in porous SiNWs prepared from a lightly doped Si wafer [154]. Due to these facts, on referring to the reports of Ghosh et al. [152], and Saxena et al. [154], it is concluded that the observed downward shift and asymmetric broadening in the Raman scattering profile are due to the dominance of phonon confinement in Si nanostructures. Moreover, the bond polarizability model for phonon confinement is given by [155],

$$\Delta\omega = \omega - \omega_0 = -A\left(\frac{a}{d}\right)^{\gamma} \tag{4.6}$$

Where ω denotes the Raman phonon wavenumber in a nanocrystal of diameter d, ω_0 denotes the optical phonon wavenumber at the zone centre, a is the lattice constant of crystalline Si, A (= 47.41 cm^{-1}) and γ (=1.44) are the phonon confinement parameters. For the presently observed downward Raman line shift of 2.8 cm^{-1}, the use of equation (4.6) yields the d value of 3.9 nm. This supports that the visible luminescence radiation, summarized in Fig. 4.13, arise due the quantum confinement of charge carriers in porous SiNWs.

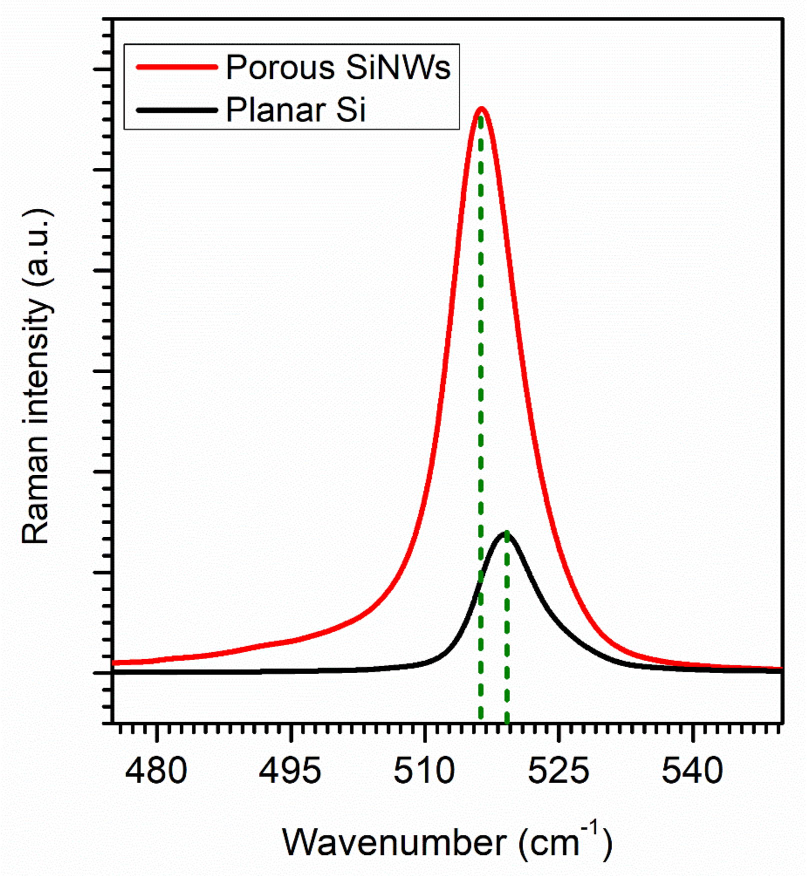

Figure 4.14 Room temperature first-order Raman spectra for porous SiNWs and planar Si. The vertical dash-dot lines indicate the location of Raman peaks.

The combined HRTEM, PL and Raman results as summarized in Figs. 3.8 c) (chapter 3), Fig. 4.13 and Fig. 4.14 are fairly agreeing that the deviation in optical properties farther away from the bulk Si arise mainly from the Si quantum structures. However, the HRTEM results (Fig. 3.8 c)) reveals that a thin amorphous layer has been formed on the Si wall surfaces. The ATR-FTIR studies depicted in Fig. 3.8 m) disclose that the thin amorphous layer consists of mostly the Si-O-Si bonding structure. As the Si walls and the oxygen coupled amorphous surface layer play a nontrivial role in the luminescence properties, the interplay that occurs at their interface structure may complicate to conclude that the visible emission in porous SiNWs is solely due to the quantum confinement effect.

It is well known that the luminescence emission peak energy corresponding to the band to band emission in Si quantum structures is sensitive to sample temperature, whereas that corresponds to the surface chemical effects are considered to be temperature insensitive [156, 157]. Therefore, on studying the PL properties of porous SiNWs as a function of sample temperature, the confirmation of quantum confinement effect and surface chemical effect on the visible emission in porous SiNWs can be verified. Figure 4.15 summarizes the overall PL behaviour of porous SiNWs in the visible region recorded at various temperatures between 80 and 375 K. All the PL spectra shown in Fig. 4.15 a) are de-convoluted into two

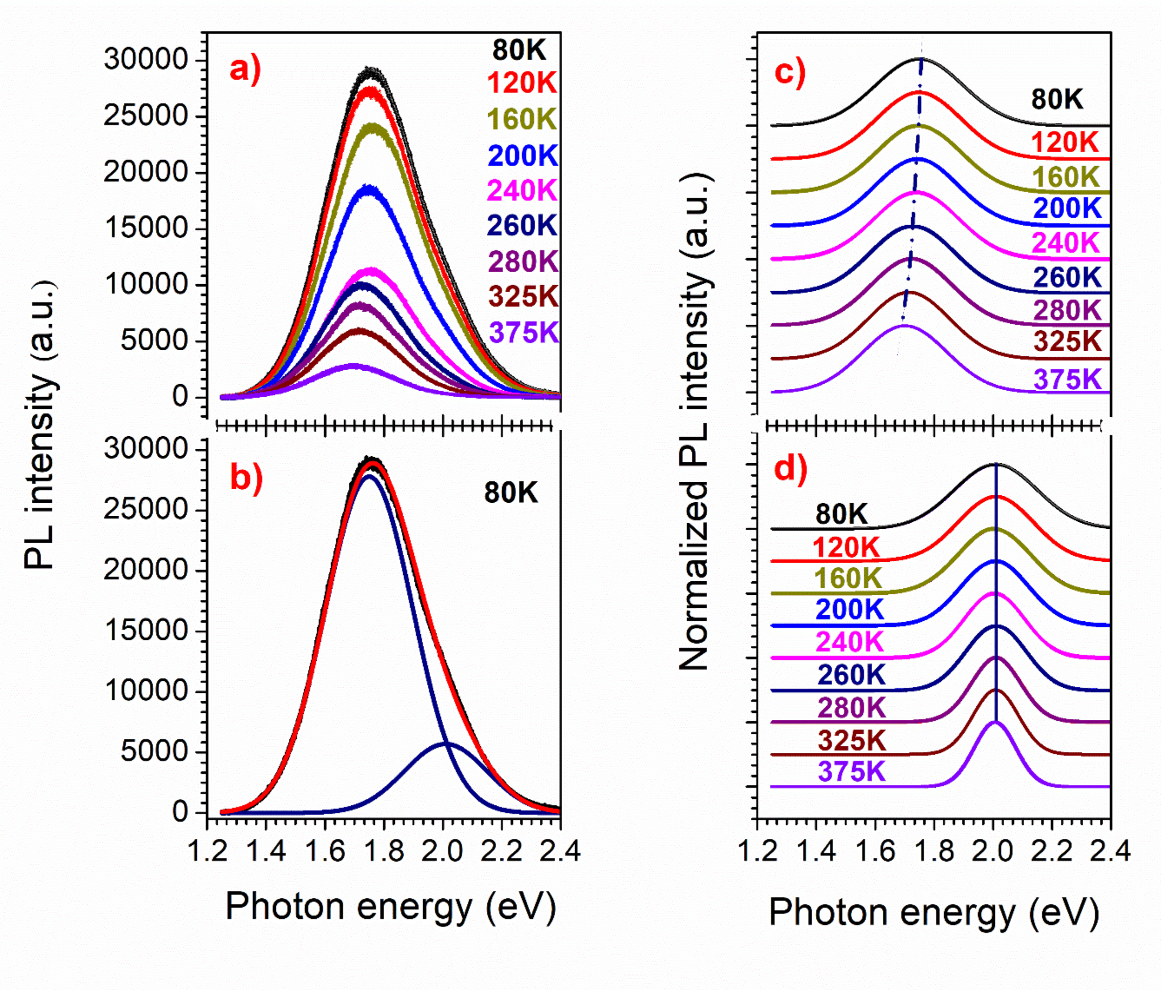

Figure 4.15 Temperature dependent PL behaviour of porous SiNWs. a) Visible PL behaviour of porous SiNWs at temperatures between 80 and 375 K. b) A fitted PL spectrum obtained at 80 K. c, d) Normalized PL spectra for peak energies E_{PL1} and E_{PL2}, respectively with sample temperatures 80, 120, 160, 200, 240, 260, 280, 325 and 375 K. Note that in Figs. a, c and d), the PL spectra shown in different colours correspond to different sample temperature.

Gaussian peak profiles. Fig. 4.15 b) shows representative fitted PL results at 80 K. The resolved luminescence peaks E_{PL1} and E_{PL2} obtained from the fit of each PL curve in Fig. 4.15 a) are shown in Fig. 4.15 c, d), respectively. It should be noted that the luminescence curves in Fig. 4.15 c, d) are normalized to their respective maximum peak intensity.

One of the most important luminescence parameters often considered in the analysis of temperature dependent luminescence behaviour in quantum semiconducting structures is luminescence emission peak energy. Figure 4.16 a, b) show the luminescence peak energies E_{PL1} and E_{PL2} with sample temperature. It is observed that there is a discrepancy in the behaviour between the emission peaks E_{PL1} and E_{PL2} with temperature. The peak energy E_{PL1} (red emission) shifts towards lower energy when the sample temperature increases from 80 to 375 K, whereas, the position of the peak energy E_{PL2} (orange emission) remains almost unchanged. Therefore, on assuming the emission peaks E_{PL1} is solely due to quantum confinement effect in porous SiNWs, the observed variation of E_{PL1} with temperature is fitted by using the well-known equation for studying the band to band emission in bulk semiconductors like Si given by [112, 156],

$$E_g(T) = E_{g,0} - A\left[\frac{2}{exp\left({\Omega}/{k_BT}\right)} + 1\right] \tag{4.7}$$

Where, $E_g(T)$, A, $E_{g,0}$, Ω and k_B are the energy band gap, temperature independent constant that describes the strength of electron-phonon interaction, energy band gap at zero Kelvin, average phonon energy and Boltzmann constant respectively. The solid line in Fig. 4.16 a) shows the best fit of the experimental data, which yields 1.887 ± 0.04 eV, 0.137 ± 0.05 eV and 0.060 ± 0.005 eV for $E_g(T)$, A and Ω respectively. Similar temperature dependent photoluminescence results have been reported previously on Si nanocrystals in the size range 1-5 nm [156, 158].

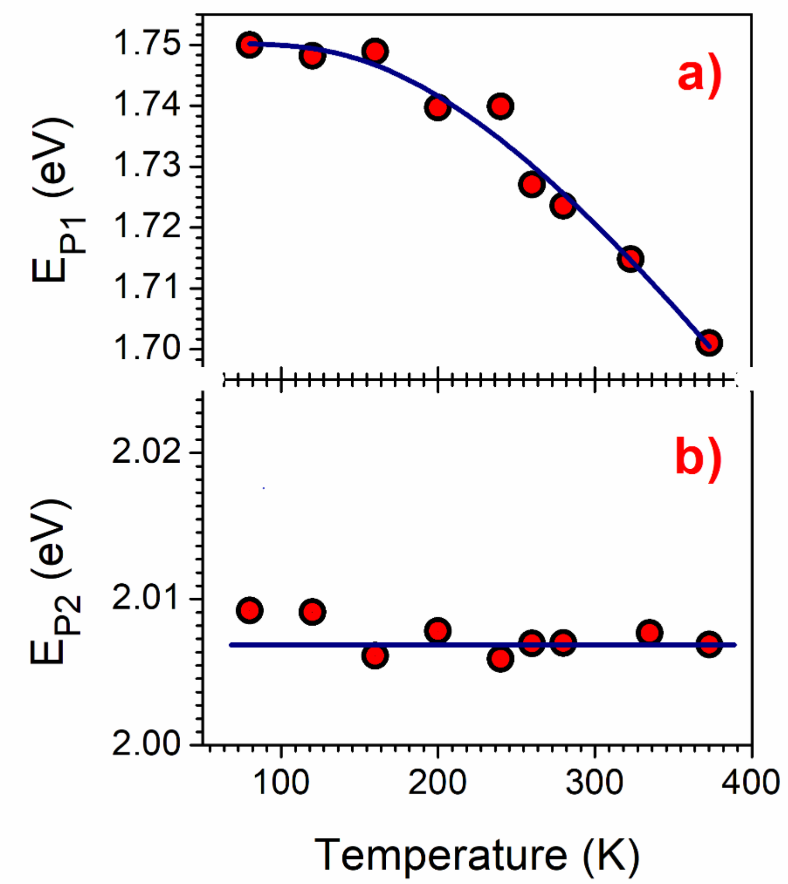

Figure 4.16 a, b) Variation of luminescence peak energies E_{PL1} *and* E_{PL1} *as a function of sample temperature, respectively. Solid curve in Fig. a) shows the best fit to the data points.*

In order to get the correlation between quantum structures in porous SiNWs and the luminescence peak energy, let us look intuitively the TEM micrographs as shown in Fig. 4.17. Fig. 4.17 a) depicts TEM and Fig 4.17 b, c) show the high resolution TEM image of porous SiNWs. It is observed that the inter-pore Si region consisting of continuous cylindrical solid fraction with uneven spherical interconnects is of quantum dimensions. In this perspective, the visible luminescence peak at 1.71 eV (E_{PL1}) emerged in the porous SiNWs can be thought of due to quantum confinement effect in the monolithic quantum wire-like cylindrical Si structure and quantum dot-like uneven spherical Si interconnects. The existence of Si quantum wire and Si quantum dot structures has been observed previously by Cullis et al. [127] and Kanemitsu et al. [126] in their respective TEM studies of porous Si prepared by anodic polarization etching. Since there are no deviations in the

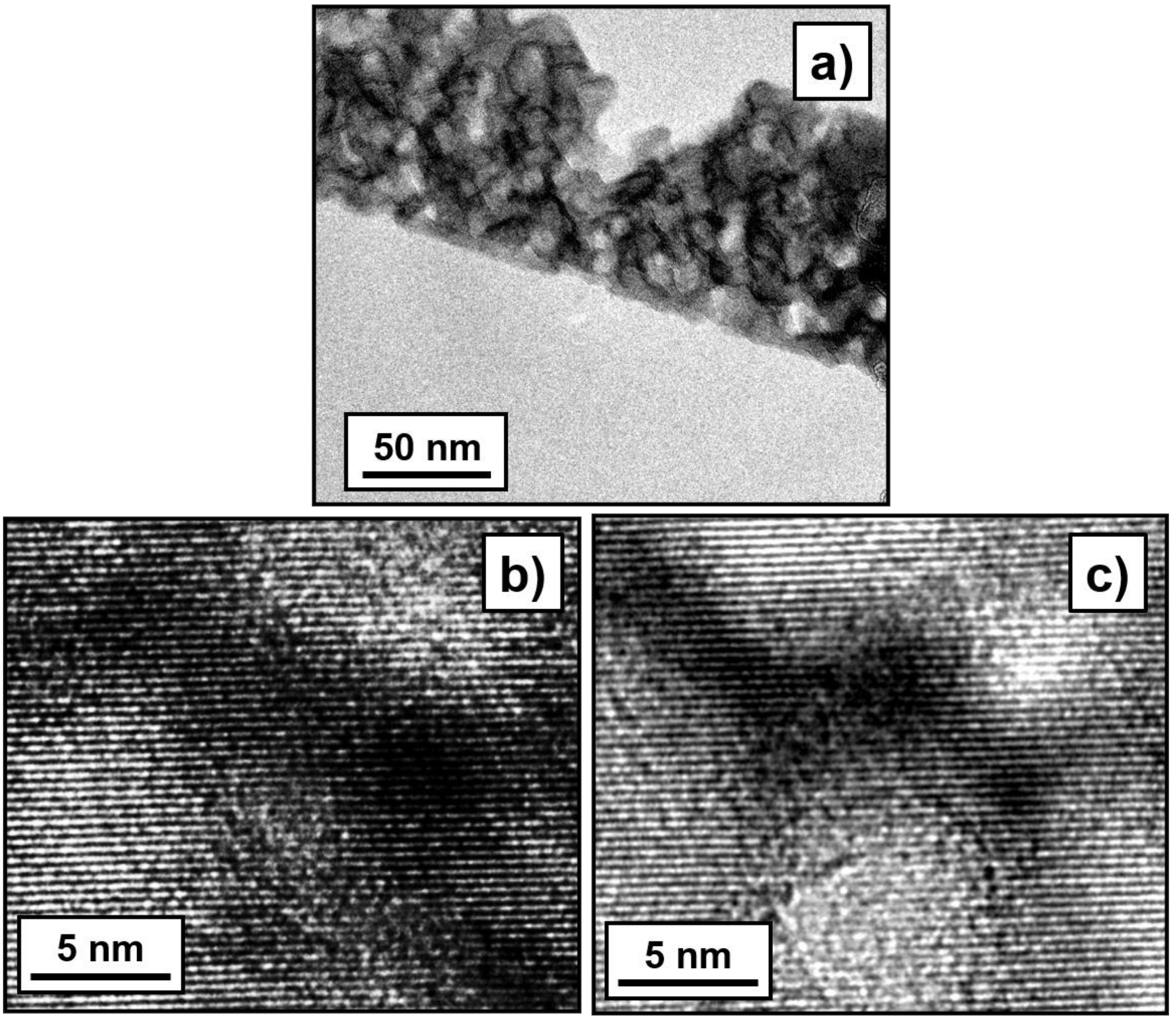

Figure 4.17 a) TEM image of porous SiNW. b, c) High resolution TEM image of porous SiNW. The phase contrast in Figs. b, c) show that inter-pore Si regions are interconnected.

lattice coherency between the wire-like cylindrical and dot-like uneven spherical Si structures, there are difficulties in correlating the observed photoluminescence peak energy with quantum structures using the existing theoretical models. For simplicity, let us apply the established equation for the isolated Si quantum dot and the quantum wire structures for the present case. The equation for the isolated quantum dot is given by [150, 159],

$$E_{PL}(d_s) = E_0 + \frac{3.73}{d_s^{1.39}} \tag{4.8}$$

Where, E_{PL} denotes the band gap energy of Si quantum dot and d_s is the diameter of the Si quantum dot and E_0 is the room temperature band gap of Si (1.12 eV). The d_s

calculated using this equation is ~ 4 nm for Si quantum dot. Similarly, the equation for Si quantum wire is given by[160],

$$E_{PL}(d_c) = E_0 + \frac{2.4}{d_c^{1.7}} \tag{4.9}$$

Where, E_{PL} denotes the band gap energy of Si quantum wire and d_c is the diameter of the Si quantum wire and E_0 is the room temperature band gap of Si (1.12 eV). The d_c determined from this equation yields ~ 3 nm for Si quantum wire. Based on the above analysis, we are summarizing that though we have correlated the structures with luminescence behaviour qualitatively, it is worth to note that the estimated d_s and d_c values from the models are fairly agreeing with the structure size obtained from the phase contrast HRTEM images of porous SiNWs. This further supports that emission peaks at 1.71 eV arises from the quantum structures present in the porous SiNWs.

4.4. Summary

The results of the present chapter are summarized as,

- ☞ The fabricated SiNWs exhibit tremendous reduction in reflectance.
- ☞ SiNWs fabricated for low etching time exhibit near-superhydrophobicity.
- ☞ The multifunctional behaviour of SiNWs synthesized at low etching time can be utilized for enhancing the efficiency and life time of Si solar cells.
- ☞ The metal assisted chemical etching combined with anodic polarization is capable of producing visible light emitting porous SiNWs.

Chapter 5

Application of MACE fabricated Si nano-architectures for gas sensor and energy storage devices

The MACE fabricated Si nanowalls (SiNWs) are explored for gas sensor and energy storage device applications. On the gas sensing front, the virgin SiNWs and SiNWs functionalized with Pt and Pd are exploited for hydrogen gas sensing device. The functionalization was achieved by the novel fluoride-free galvanic displacement deposition. Characterization by different techniques viz. SEM, EDX and GIXRD confirmed the successful functionalization. Both the Pt and Pd loaded SiNWs exhibit enhanced sensor performance compared to pristine SiNWs. The temperature dependent sensing studies manifest that Pt functionalized SiNWs display superior sensing behaviour at low temperatures (50-100ºC) in comparison to Pd functionalized SiNWs and vice versa at high temperature (150-200ºC). A parallel resistance model bearing the effect of electronic and chemical sensitization was used to elucidate the observed sensing behaviour. For energy storage devices, the SiNWs are explored for possible application as electrochemical capacitor, using the organic electrolyte tetraethylammonium tetrafluoroborate (NEt_4BF_4*) in propylene carbonate (PC). The cyclic voltammetry and galvanostatic charge-discharge studies revealed that SiNWs exhibit redox peaks in low and high potential regions. The origin of these peaks are attributed to the silver related deep level trap state in silicon in contact with adsorbed water and also from the oxidation of silicon and its hydrides by the moisture present in the electrolyte respectively. The presence of silver in SiNWs and water in the electrolyte are considered to be due to the minute amount of silver left over during its removal by* HNO_3 *owing to the bunching of nanowalls and the highly moisture sensitive nature of the electrolyte respectively. The impact of such redox peaks on areal capacitance and cycle life are investigated.*

5.1. Introduction

In recent past, Si nanostructures synthesized by metal assisted chemical etching (MACE) are investigated for application in gas sensors and energy storage devices, owing to its compatibility with established CMOS technology, which can lead to direct on chip integration into the existing Si microelectronic industry [22, 161, 162]. We are interested in the hydrogen (H_2) sensing properties of silicon nanostructures owing to its importance in nuclear industry. For hydrogen sensing, both pristine and platinum (Pt) & palladium (Pd) functionalized Si nanostructures have been investigated. Functionalized Si sensors are favourable due to their selectivity for a particular gas against other chemical species [25]. However the functionalization of Si nanostructures with these metals have mostly been achieved by techniques like electron beam evaporation, magnetron sputtering, pulsed laser deposition etc. [163, 164], which are energy and cost intensive. There are few reports on the cost effective galvanic displacement metal deposition technique [96] to functionalize Si nanostructures for H_2 sensing. However, the use of HF along with the metal salt solution in this method can change the initial morphology of the fabricated Si nanostructures. Therefore, it is required to modify the technique, to functionalize the Si nanostructures without disturbing its initial morphology.

Among different energy storage devices, electrochemical capacitor has been considered as a prominent energy storage device because of its fast charge/discharge rate, high power density, long cycle-life and safe of operation [97]. For electrochemical capacitor application, the MACE fabricated Si nanostructures are usually coated with other materials such as silicon carbide, ultrathin carbon sheath, graphene and nickel oxide [22, 98-100], due to the reactivity of Si with the commonly used aqueous electrolytes. But, use of these coated materials can cause compatibility issues with the established CMOS fabrication technology, as well as increase the production cost. Recently, the research group led by S. Sadki have studied silicon nanowires and nanotrees, grown by the vapour-liquid-solid (VLS) technique without any additional coating, for electrochemical capacitor application using different organic and ionic liquid electrolytes [21, 101, 102]. However, the issues related to high cost and high temperature VLS growth method may limit its application. Therefore, it is exciting to investigate the electrochemical behaviour of the MACE fabricated Si nanostructures in these electrolytes for its application towards electrochemical capacitor.

The investigation of Si nano-architectures both in pristine and functionalized with Pt and Pd using fluoride-free galvanic displacement technique, for H_2 sensing and electrochemical behaviour of Si nano-architectures in the electrolyte, tetraethylammonium tetrafluoroborate (NEt_4BF_4) in propylene carbonate (PC), for electrochemical capacitor application are the other highlights of the study.

5.2. Experimental

5.2.1. Gas sensing and electrochemical measurements

The SiNWs prepared by MACE was used for gas sensing and electrochemical capacitor applications. For gas sensing (H_2 sensing) both pristine and Si nanowalls functionalized with Pt/Pd are used. The fluoride-free galvanic displacement deposition method was used for the functionalization. For this, SiNWs sample was assembled into the O-ring tightened Teflon cell assembly as used for etching (Fig. 2.1, chapter 2). The surface oxide of the SiNWs was removed by treating it in 5% HF solution for 1 minute followed by washing with Milli-Q water thrice to ensure the complete removal of HF. Subsequently, metal (Pt or Pd) deposition was carried out using its aqueous salt solution (3 mM K_2PtCl_6 for Pt and 3 mM $PdCl_2$ for Pd) without the use of any fluoride species. After the functionalization, the samples were copiously rinsed with Milli-Q water and dried by nitrogen purging. Henceforth, the SiNWs functionalized with Pt and Pd will be denoted as Pt-SiNWs and Pd-SiNWs respectively.

The gas sensors were fabricated by making interdigitated Au electrodes on the SiNWs, Pt-SiNWs and Pd-SiNWs using DC sputtering. The sensing performance of the sensor device was studied in a custom built gas exposure system, as described in Fig. 2.14 (Chapter 2). The sensing measurements were conducted under dynamic condition, where the gas was flown at a constant rate over the senor device and a fixed pressure inside the sensing chamber was maintained under continuous pumping by a scroll pump. The measurement was carried out for different concentration (50-500 ppm) of analyte gas at different temperatures (50-200ºC). The sensor response was calculated from the measurement by the following equation,

$$Sensor\ response, S\ (\%) = \frac{R_G - R_0}{R_0} \times 100 \qquad (5.1)$$

Where R_G and R_0 are the resistances of the sensor device in the presence of background gas (a mixture of N_2 and O_2) and the analyte gas, H_2 (a mixture of H_2, N_2 and O_2) at different concentrations, respectively. During the whole measurement the total flow rate of gaseous mixture and flow rate of O_2 were maintained at 28 sccm and 2.8 sccm respectively, and different concentrations of H_2, were obtained by changing the flow rate of H_2 and N_2.

Electrochemical characterizations of the prepared SiNWs were conducted using the commercial potentiostat (Metrohm Autolab, model PGSTAT 302N) at room temperature. Prior to the electrochemical studies, the SiNWs sample were treated with dilute HF to remove its surface oxide layer, rinsed in acetone and dried in argon stream. The silicon wafers having the nanowalls carved on them were then successfully assembled into a home-built 3 electrodes electrochemical cell as shown in Fig. 2.5 (chapter 2). The SiNWs sample, platinum and Ag/AgCl couple were used as working, counter and reference electrodes respectively. A solution of 1 M NEt_4BF_4 in PC was used as the electrolyte. In this configuration, the cyclic voltammetry was conducted at scan rates ranging from 10 to 100 mV/s at potential windows of 0.9 and 1.2 volts. The galvanostatic charge-discharge studies were performed at different applied currents. All the electrochemical studies were performed in moisture free closed environment.

The morphology, elemental composition and mapping of fabricated samples were investigated using field emission scanning electron microscope (FESEM, Carl Zeiss Supra 55) equipped with energy dispersive X-ray spectroscope (EDX) operated in secondary electron imaging mode. The crystal structures of the samples were studied using the X-ray diffractometer (Inel, Equinox 2000) in grazing incidence configuration (GIXRD) using Cu-Kα radiation (1.541 Å). The details of these instruments are described in chapter 2.

5.3. Results and discussions

5.3.1. Gas sensing studies

5.3.1.1. Mechanism of galvanic displacement process for functionalization

The mechanism behind the functionalization process can be visualized by inspecting the standard redox potential (V vs. SHE) of the redox couples: 0.36 for Pt^{4+}/Pt, 0.90 for Pd^{2+}/Pd and -1.24 (or -0.84) for Si/SiF_6^{2-}(or Si/SiO_2) [165, 166]. Since, the redox potential of Pt^{4+}/Pt and Pd^{2+}/Pd redox couples are greater than that of Si/SiF_6^{2-}(or Si/SiO_2), the Pt or Pd ions extract valence band electrons (bonding electron) of Si and get itself reduced. The process is accompanied by the simultaneous oxidation of Si. The redox process is described by the following reactions,

At Cathode: $Pt^{4+} + 4e^- \rightarrow Pt$ ($E^0 = 0.36$ V vs. SHE; for Pt deposition) (5.2)

$Pd^{2+} + 2e^- \rightarrow Pd$ ($E^0 = 0.90$ V vs. SHE; for Pd deposition) (5.3)

At anode: $Si + 2H_2O \rightarrow SiO_2 + 4H^+ + 4e^-$ ($E^0 = -0.84$ V vs. SHE) (5.4)

The reduction of metal ions leads to nucleation and its subsequent growth into particles on the Si nanowalls forming a thin layer of silicon oxide at the interface.

5.3.1.2. Morphological and elemental analyses of pristine and functionalized SiNWs

The scanning electron micrographs of pristine SiNWs, Pt-SiNWs and Pd-SiNWs are depicted in Fig. 5.1 which reveals that nanowalls are vertically aligned to their base Si wafer. It is manifested from the top and the cross-section morphologies of Pt-SiNWs and Pd-SiNWs shown in Fig. 5.1 b, e) and c, f) respectively that Pt and Pd are deposited mostly on the top part of Si nanowalls. The energy dispersive X-ray spectroscopy (EDX) studies conducted on these samples are summarized in Fig. 5.2. The EDX spectra of the SiNWs, Pt-SiNWs and Pd-SiNWs confirm that the pristine SiNWs sample consists of only Si and oxygen whereas Pt-SiNWs (or Pd-SiNWs) contains Si, oxygen (O) and Pt (or Pd). The atomic percentages of the constituent elements are displayed in their respective insets (tables). The EDX elemental mapping was carried out at Si K and O K edge for all the samples and the same was conducted at Pt M and Pd L edges for the Pt-SiNWs and Pd-SiNWs respectively.

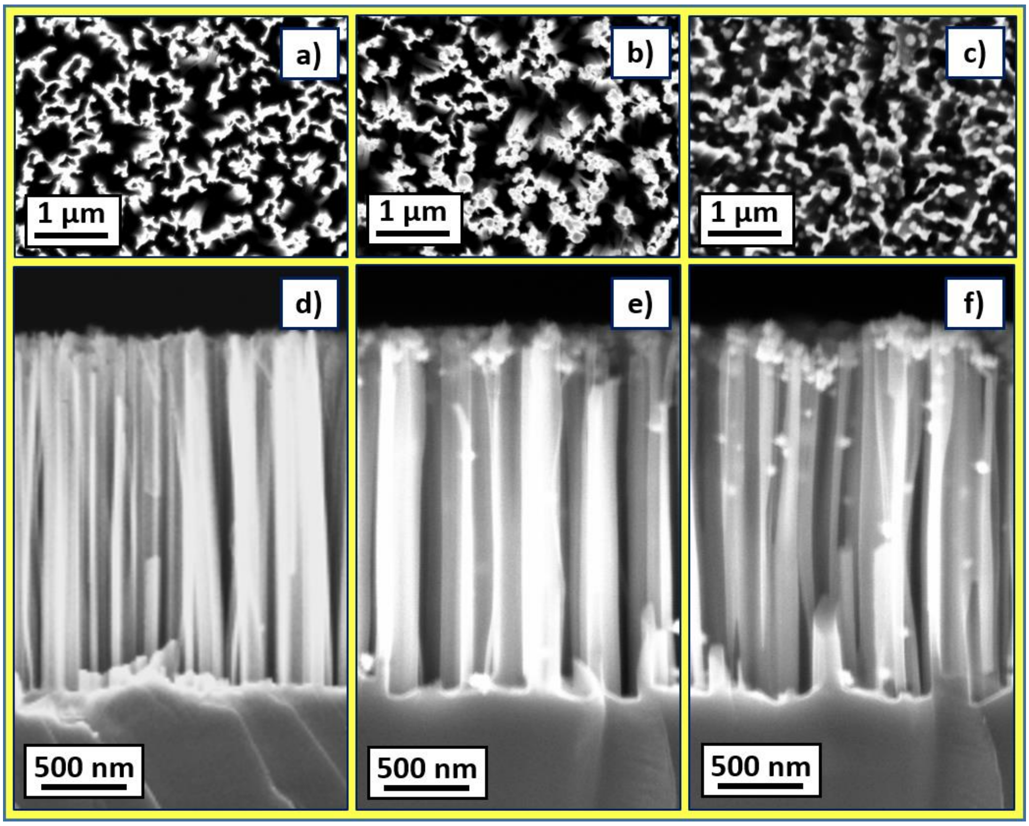

Figure 5.1 Scanning electron micrographs of pristine SiNWs, Pt-SiNWs and Pd-SiNWs are shown in top and cross-section view in figures a-c) and d-f) respectively.

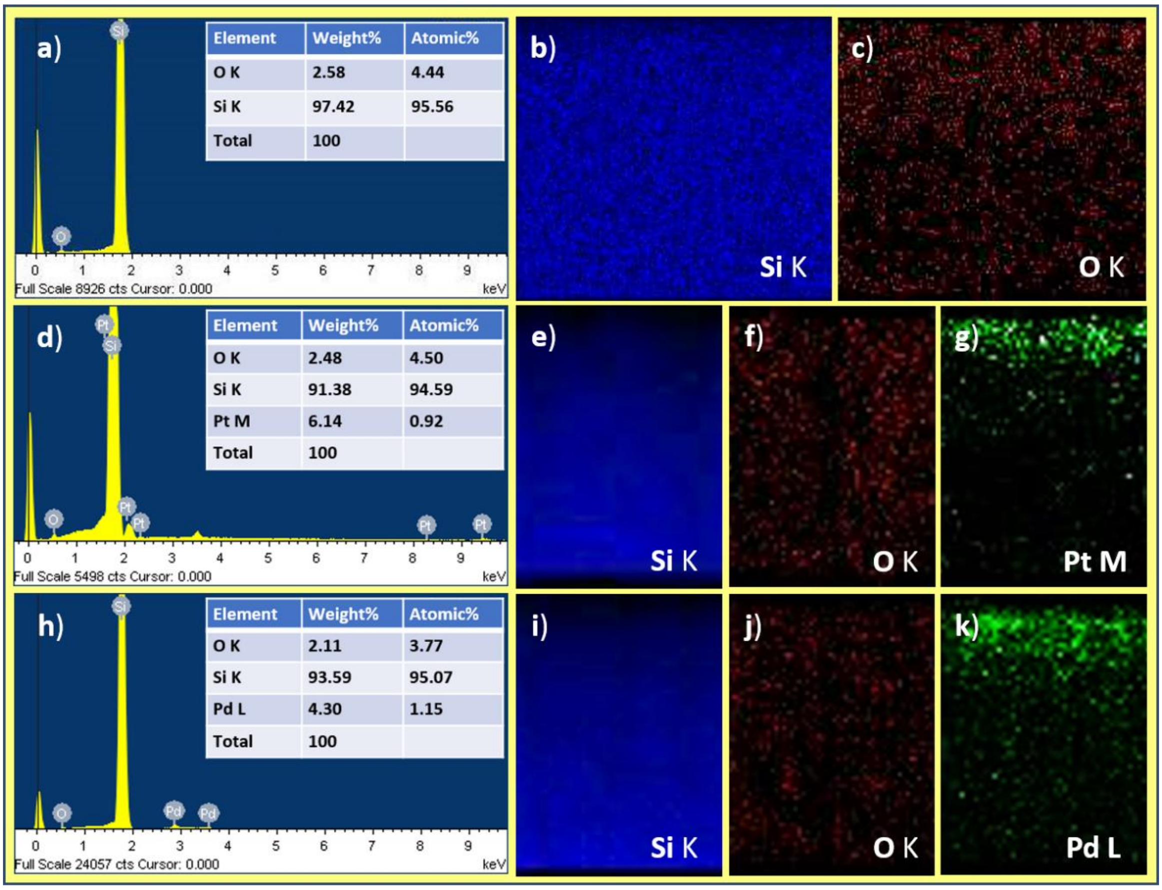

Element	Weight%	Atomic%
O K	2.58	4.44
Si K	97.42	95.56
Total	100	

Element	Weight%	Atomic%
O K	2.48	4.50
Si K	91.38	94.59
Pt M	6.14	0.92
Total	100	

Element	Weight%	Atomic%
O K	2.11	3.77
Si K	93.59	95.07
Pd L	4.30	1.15
Total	100	

Figure 5.2 a, d, h) Demonstrate the EDX spectra of pristine SiNWs, Pt-SiNWs and Pd-SiNWs respectively where the weight and atomic percentage of the elements, present in the sample are displayed in their respective insets (tables). The EDX elemental mapping at Si K edge and O K edge of pristine SiNWs, Pt-SiNWs and Pd-SiNWs samples in cross-section view are depicted in figures b, c), e, f) and i, j) respectively. g, k) Illustrate the EDX elemental mapping at Pt-M edge and Pd-L edge for Pt-SiNWs and Pd-SiNWs in cross-section view respectively.

5.3.1.3. Structural analyses of pristine and functionalized SiNWs

Figure 5.3 shows the grazing incidence X-ray diffraction (GIXRD) patterns of pristine SiNWs, Pt-SiNWs and Pd-SiNWs. It is observed that the GIXRD pattern of pristine SiNWs exhibit merely a high intense diffraction peak at 56°, whereas that of Pt-SiNWs and Pd-SiNWs exhibit additional diffraction peaks around 40°, 46°, 68°, 82° along with the high intense peak at 56°. The high intense peak at 56° is ascribed to the diffraction from (311) crystallographic plane of Si as discussed in Chapter 3. The other peaks around 40°, 46°, 68°, 82° arises due to diffraction from (111), (200), (220) and (311) crystallographic planes respectively, of the face-centered cubic Pt and Pd lattice [167]. As the diffraction peaks of

Pt and Pd lattice occurs at the same position, the GIXRD pattern of Pt-SiNWs and Pd-SiNWs exhibit almost similar appearance. This shows that fluoride-free galvanic deposition produces pure and crystalline Pt and Pd particles.

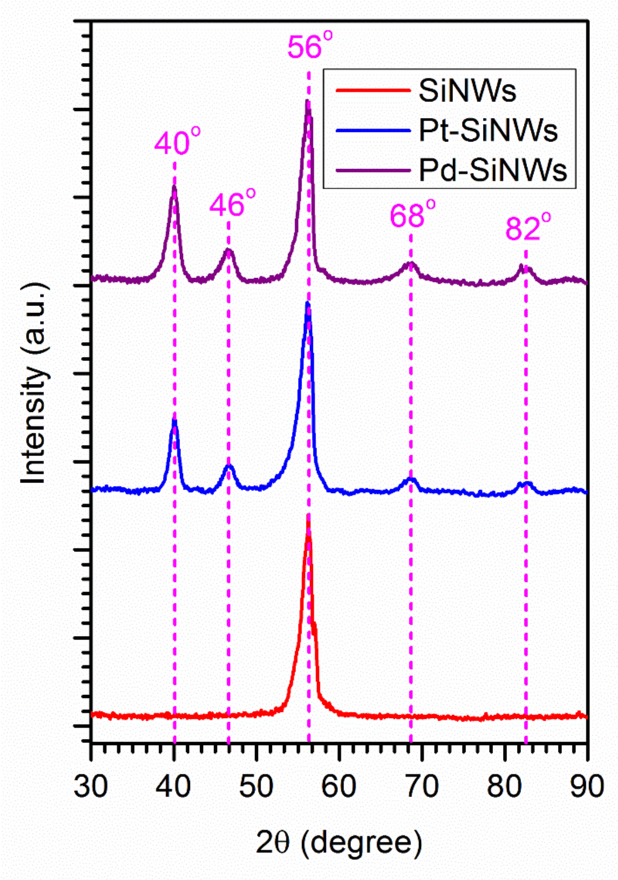

Figure 5.3 Grazing incidence X-ray diffraction patterns of pristine SiNWs, Pt-SiNWs and Pd-SiNWs samples.

5.3.1.4. Hydrogen sensing performance

Figure 5.4 summarizes the sensor response of the fabricated SiNWs, Pt-SiNWs and Pd-SiNWs devices at different operating temperatures (50-200ºC) for various H_2 concentrations (50-500 ppm). It is observed from Fig. 5.4 a, b, c) that SiNWs exhibit H_2 sensing behaviour at the concentration of 100 ppm whereas both Pt-SiNWs and Pd-SiNWs exhibit this at a lower concentration of 50 ppm. Moreover, the sensor response of SiNWs increases with the operating temperature till 150ºC and then decreases at 200ºC, whereas that for Pt-SiNWs and Pd-SiNWs increases persistently over the whole temperature range.

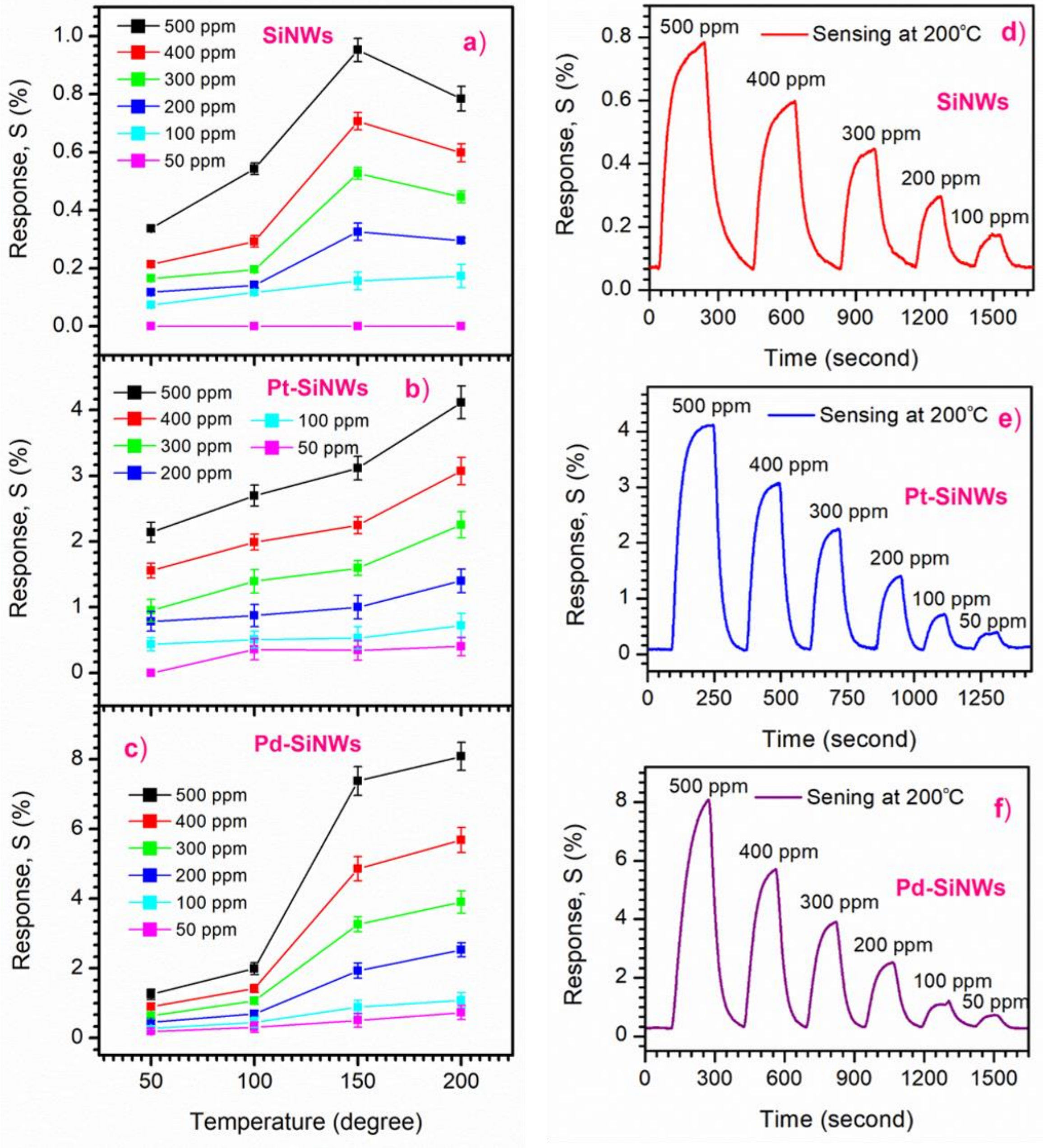

Figure 5.4 a, b, c) Summarize sensor response (S) versus operating temperature at different H_2 concentrations for SiNWs, Pt-SiNWs and Pd-SiNWs respectively. d, e, f) Display response transient at the operating temperature of 200ºC with H_2 concentrations ranging from 50 to 500 ppm, for SiNWs, Pt-SiNWs and Pd-SiNWs respectively.

Figure 5.4 d, e, f) display the response transient at the operating temperature of 200ºC with H_2 concentrations ranging from 50 to 500 ppm for SiNWs, Pt-SiNWs and Pd-SiNWs respectively. In order to have better assessment, sensor response as a function of temperature at 500 ppm and as a function of H_2 concentration at 200ºC are demonstrated in Fig. 5.5 a,

b) respectively. It is evident that both Pt-SiNWs and Pd-SiNWs shows higher sensor response than that of SiNWs. It is clear from the figure that sensor response exhibits an almost linear dependence with H_2 concentration whereas its dependence with operating temperature is quite different. A careful observation on temperature dependence of sensor response (Fig. 5.5 a)) reveals that the sensor response of Pt-SiNWs exhibits higher value than that of Pd-SiNWs at low temperatures (50-100ºC) and bears a linear temperature dependence. On the other hand, sensor response for Pd-SiNWs shows a sudden jump at 150ºC with higher value (~ twice) than that of Pt-SiNWs followed by a gradual increase.

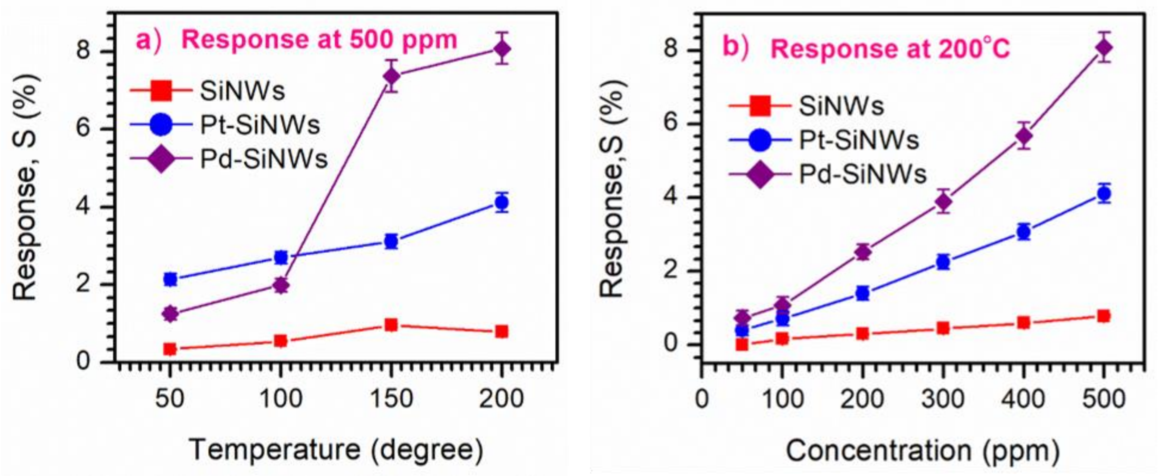

Figure 5.5 Display the comparison of sensor response (S) of the SiNWs, Pt-SiNWs and Pd-SiNWs sensor devices. a) Plot depicting sensor response (S) versus temperature at H_2 concentration of 500 ppm. b) Plot showing sensor response (S) versus H_2 gas concentration at operating temperature of 200ºC.

The H_2 sensing behaviour of SiNWs, Pt-SiNWs and Pd-SiNWs can be understood by following the resistance based parallel model used for explaining ammonia sensing behaviour of silver modified Si nanowires by Qin et al. [168] as well as the catalytic behaviour of decorated metals (Pd or Pt). The fabricated SiNWs are p-type (doping) in nature as these are obtained by etching of p-type base Si wafer. When p-type SiNWs are exposed to atmospheric environment, the oxygen molecules (O_2) are adsorbed on the SiNWs surface. Because of the strong electron affinity of the adsorbed oxygen molecules, they withdraw electron from the SiNWs and subsequently get ionized forming highly reactive oxygen species like O_2^-, $O^-$and O^{2-}(mainly O_2^- at room temperature) [169, 170]. As a consequence, hole-accumulation layer (HAL) is formed at the nanowall surface, covering the resistive core as demonstrated schematically in Fig. 5.6 a). So the current conduction through the SiNW can be described by current conduction through a parallel resistance model with two resistors connected in parallel as shown in Fig. 5.6 a). The R_C and R_H are the resistance of the two resistors and denote the resistance of resistive core and HAL respectively. Owing to the high concentration of carriers (hole) at the HAL, R_H is significantly lower than R_C. Therefore, the current flow dominantly across R_H and the resistance of the SiNW can be expressed as,

$$R_{NW} \approx R_H = \frac{\rho L}{A_H} \tag{5.5}$$

Where R_{NW} and L denote the resistance and length of the nanowall respectively. ρ and A_H denote the resistivity and cross-sectional area of the HAL respectively.

When the SiNWs sensor device is exposed to H_2 gas (reducing gas), the adsorbed oxygen species react with the adsorbed hydrogen at the SiNW surface releasing the electron back to the SiNW. The process can be described by the following reactions,

$$H_2(gas) \rightarrow H_2(ads) \tag{5.6}$$

$$2H_2(ads) + \; O_2^-(ads) \rightarrow 2H_2O(ads) + e^- \tag{5.7}$$

As a result, the HAL is effectively reduced as illustrated in Fig. 5.6 b). Constructing the parallel resistance model under the same analogy, the resistance of the SiNW after H_2 exposure can be expressed as,

$$R_{NWG} \approx \; R_{HG} = \frac{\rho L}{A_H - \Delta A_H} \tag{5.8}$$

Where R_{NWG} represent the resistance of SiNW after H_2 gas exposure, R_{HG} and ΔA_H represent the resistance and change in cross-sectional area of HAL after H_2 exposure. The comparison between equation (5.5) and (5.8) reveals that R_{NWG} is greater than R_{NW}.

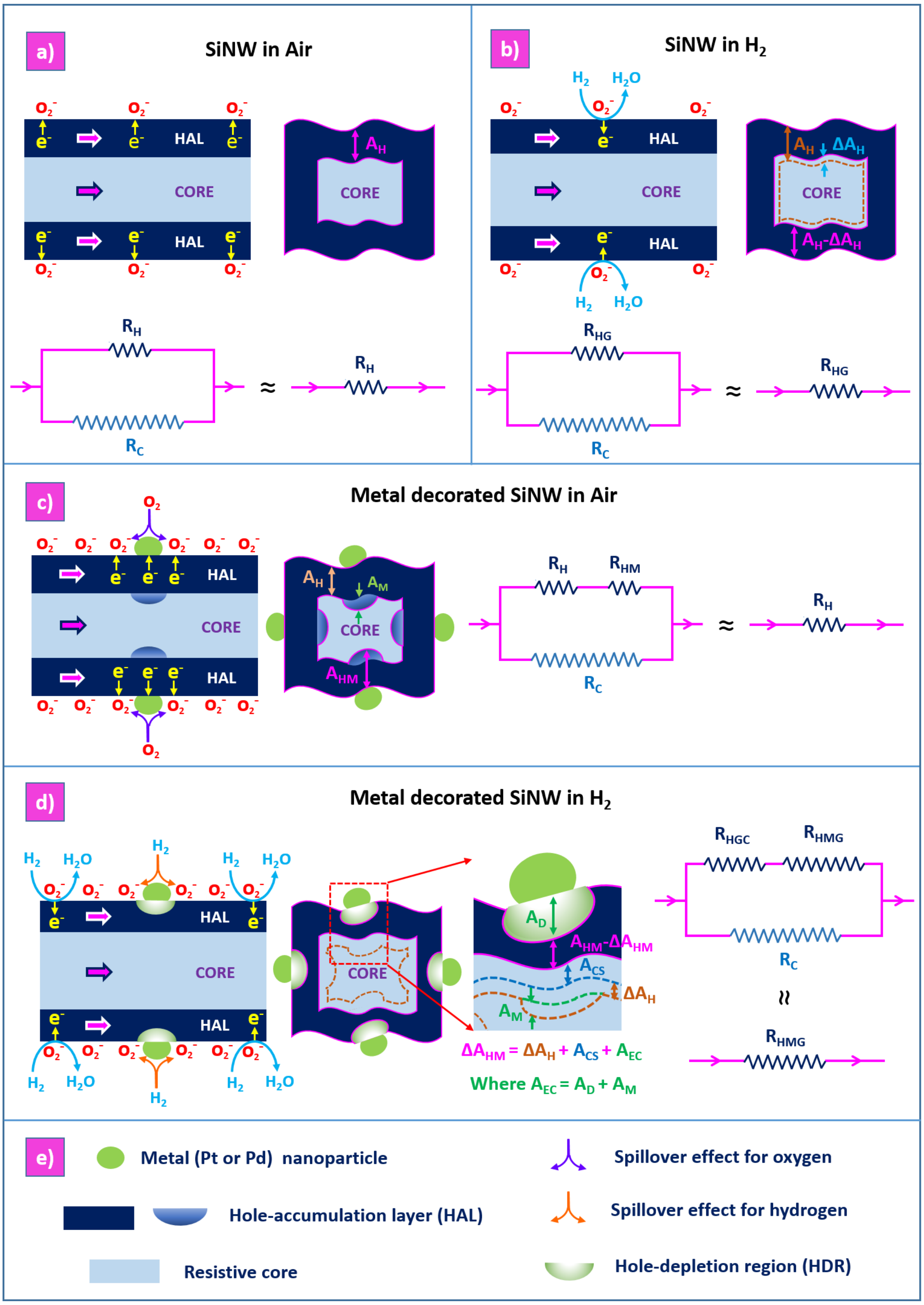

Figure 5.6 Schematic illustrating the H_2 sensing mechanism in a, b) SiNWs and c, d) metal (Pt or Pd) functionalized SiNWs. e) Description of different symbols.

Following equation (5.1), the room temperature sensing behaviour of SiNWs is explained.

Before addressing the observed temperature dependent sensing behaviour of SiNWs (i.e.

the increase in sensor response with temperature followed by decrease above 150ºC), it is worth to note that the present gas sensing mechanism is analogous to the gas sensing mechanism of metal oxide based semiconductor. An extensive study by Ahlers et al. [171] has revealed that metal oxide based semiconductor gas sensors exhibit similar temperature dependent sensing behavior (bell-shaped sensor response with temperature). This is ascribed to both the enhancement in reaction probability between adsorbed analyte gas molecule and surface oxygen ion with increase in temperature, as well as desorption of the adsorbed analyte gas after a specific temperature, leading to an optimum temperature for sensing behaviour. This explains the temperature dependence of sensor response of the SiNWs.

The superior sensing behaviour of metal functionalized SiNWs (Pt-SiNWs and Pd-SiNWs) can be explained by adding the effect of the metals to the above sensing mechanism based on the parallel resistance model. The metals cause the occurrence of two sensitizations: i) chemical sensitization (also known as spillover effect) arises due to interfacial atom transport and ii) electronic sensitization arises due to interfacial electronic redistribution. Let us first analyse the current conduction in metal functionalized SiNWs and construct the equivalent parallel resistance model in air, as demonstrated in Fig. 5.6 c). Since, the work function of the metals (5.12 eV for Pd and 5.65 eV for Pt) are higher that of p-type Si (4.9 eV), the nature of the metal and semiconductor junction is ohmic, with a flow of electron from the p-type Si to the metal [163, 172]. So, the HAL is expanded nearby the metal resulting the new area of HAL underneath the metal particle, given by, $A_{HM} = A_H + A_M$, where A_M represents the increased cross-sectional area of HAL beneath the metal particle. Under the same analogy, the equivalent parallel resistance model is built where current flow dominantly across the HAL. But in the present case, the resistance of the HAL is governed by the series combination of two resistors with resistance R_H and R_{HM}, which are further determined by the cross-sectional areas A_H and A_{HM} respectively as described in

Fig. 5.6 c). Since, R_H is greater than R_{HM} (as $A_H < A_{HM}$), the resistance of the whole HAL is governed mostly by R_H. Therefore, the resistance of the metal functionalized SiNW can be described as,

$$R_{MNW} \approx R_H = \frac{\rho L}{A_H} \tag{5.9}$$

When metal functionalized SiNWs is exposed to the H_2 environment, the H_2 spillover (chemical sensitization) occurs as demonstrated in Fig 5.6 d). In this process, significantly more H_2 molecules are adsorbed because the catalytic metal provides more active sites for its adsorption. The adsorbed H_2 molecules are subsequently dissociated into atomic species followed by their rapid diffusion through catalytic metal (Pd or Pt) owing to their high solubility and diffusivity. These diffused hydrogens then settle at the metal-Si interface and form a polarization layer which reduces effectively the work function of metal. As a result, Schottky barrier is formed at the metal-semiconductor (p-type Si) junction [173, 174]. It is worth to note that there exists a thin layer of silicon oxide at metal-Si interface, since the deposition of metal is carried out by fluoride free galvanic displacement as discussed previously. The silicon oxide layer serves as a diffusion barrier against PdSi/PtSi formation and reduces the effect of Fermi level pinning [173]. But it being too thin does not inhibit the transport of carriers and hence not included in schematic description. This process with a transition from ohmic to Schottky barrier is the phenomenon of electronic sensitization. As a consequence, hole-depletion regions (HDR) are formed around the metal particles inside the HAL as illustrated in Fig 5.6 d). So, HAL is reduced effectively underneath the metal particle with its cross-sectional area accessible for current conduction given by, $(A_{HM} - \Delta A_{HM})$, where ΔA_{HM} represents the change in cross-sectional area of HAL underneath the metal particle after H_2 exposure. It is manifested from Fig. 5.6 d) that, $\Delta A_{HM} = \Delta A_H + A_{CS} + A_{ES} = \Delta A_H + A_{CS} + A_D + A_M$, where A_{CS} and A_{ES} (=$A_D + A_M$) denote the reduction in cross-sectional area of HAL beneath the metal particle due to chemical and electronic sensitizations respectively, A_D is the area of HDR inside HAL underneath the metal particle and others have their usual meaning. Under the identical analogy, the equivalent parallel resistance model is constructed as depicted in Fig 5.6 d). In the present scenario, the resistance of the HAL is governed by the series combination of two resistors with resistances R_{HGC} and R_{HMG}. These are further determined by the cross-sectional area of HAL beneath the SiNW and metal particle respectively. As evident from the Fig. 5.6 d) that the cross-sectional area of HAL underneath the metal particle ($A_{HM} - \Delta A_{HM}$) is significantly lower than that of SiNW, therfore resistance of the whole HAL is mostly governed by R_{HMG}. Hence, the resistance of the metal functionalized SiNWs after H_2 exposure can be described by,

$$R_{MNWG} \approx R_{HMG} = \frac{\rho L}{A_{HM} - \Delta A_{HM}} = \frac{\rho L}{A_H - (\Delta A_H + A_{CS} + A_D)} \tag{5.10}$$

Where R_{MNWG} is the resistance of metal functionalized SiNW after the H_2 exposure. The final expression is then obtained by using, $A_{HM} = A_H + A_M$ and $\Delta A_{HM} = \Delta A_H + A_{CS} + A_D + A_M$.

Now, following equation (5.1), the sensor response of SiNWs and metal functionalized SiNWs can be calculated as,

$$S_{NW} = \frac{R_{NWG} - R_{NW}}{R_{NW}} = \frac{\Delta A_H}{A_H - \Delta A_H} \tag{5.11}$$

$$S_{MNW} = \frac{R_{MNWG} - R_{MNW}}{R_{MNW}} = \frac{(\Delta A_H) + (A_{CS} + A_D)}{(A_H - \Delta A_H) - (A_{CS} + A_D)} \tag{5.12}$$

Where, S_{NW} and S_{MNW} denote the sensor response of SiNWs and metal functionalized SiNWs respectively. The final expression for S_{NW} and S_{MNW} are achieved by using the expression for R_{NW}, R_{NWG}, R_{MNW} and R_{MNWG} from the equations (5.5, 5.8, 5.9 and 5.10) respectively. The comparison between the equations (5.11) and (5.12) reveals that the extra term $(A_{CS} + A_D)$ is added and subtracted in the numerator and denominator of

S_{NW}, respectively to obtain S_{MNW}. Therefore, S_{MNW} is greatly higher than S_{NW}. This successfully explains the enhanced sensing behaviour of metal functionalized SiNWs (Pt-SiNWs and Pd-SiNWs).

Before addressing the temperature dependent sensing behaviour of Pt-SiNWs and Pd-SiNWs compared in Fig. 5.5 a), which is quiet complex especially for Pd-SiNWs, it is worth to note that the Pd-SiNWs is expected to exhibit higher sensor response than that of Pt-SiNWs because of the higher surface coverage of Pd with H_2 than that of Pt [174, 175]. A plausible explanation for such complex sensing behaviour can be thought of, by considering that the hydrogen sensing behaviour in present study are performed in presence of oxygen atmosphere. In oxygen atmosphere, molecular oxygen reacts with metal surface and gets chemisorbed. The reaction of this surface with chemisorbed H_2 results the catalytic formation of water molecules, which are subsequently desorbed from the surface. The process can be described by the following surface reactions [176],

$$M - O + \frac{3}{2} H_2(ads) \rightarrow M - H + H_2O(ads) \tag{5.13}$$

$$H_2O(ads) \rightarrow H_2O(g) \tag{5.14}$$

Adsorbed OH can take part in reaction (5.13) as an intermediate [176]. According to literature reports, the rate of water formation on Pt is rather faster than that on Pd, in air under identical condition of T=100ºC and P_{H_2}(ranging from 200-5000 ppm) [176, 177]. Therefore at low temperatures in oxygen atmosphere, due to the higher water formation rate at the Pt surface, the formation of $Pt - H$ can exceed the formation of metal oxide $Pt - O$ and vice versa for Pd. So at equilibrium, there will be resultant formation of $Pt - H$ and $Pd - O$ over Pt and Pd surface respectively. The formation of $Pd - O$ over Pd surface can deteriorate the electronic sensitization (as described previously) in case of Pd-SiNWs sample which gives rise to low sensor response. This is in line with the gas sensing study by C. Liu at al. [169], where they have reported that the formation of $Pd - O$ causes the reduction in sensitivity of SnO_2-based gas sensors. It is also reported that PdO is a p-type semiconductor [178]. So for the present case of p-type SiNWs (since obtained by etching p-type wafer), nature of the junction between PdO and SiNWs will be ohmic (instead of Schottky) which also suggests the absence of electronic sensitization. However, at higher temperature, the rate of water formation at Pd surface may increases to be high enough, resulting in the net formation of $Pd - H$. As a consequence, electronic sensitization starts to occur and because of the higher surface coverage of hydrogen on Pd surface, there is an enhancement in sensor response of Pd-SiNWs with a jump at high temperature region (150ºC), followed by a steady increase afterwards. On the other hand, in case of Pt-SiNWs, since the electronic sensitization takes places from the low temperature and continues afterword, the senor response exhibits an almost linear temperature dependence throughout the whole temperature region. This elucidates fairly the observed complex temperature dependent sensor behaviour of Pt-SiNWs and Pd-SiNWs. Nevertheless, an in depth-study should be carried to find a precise explanation of such temperature dependent sensing behaviour.

5.3.2. Electrochemical Studies

5.3.2.1. Morphological studies of SiNWs

The scanning electron micrographs of the MACE fabricated SiNWs for electrochemical studies are depicted in Fig. 5.7. The top and cross-section SEM images as displayed respectively in Fig. 5.7 a, b) for sample-1 and Fig. 5.7 c, d) for sample-2 reveal that nanowalls are smooth and vertically aligned in both the samples. It is evident from their corresponding insets shown at bottom right and top left, that SiNWs are homogeneously distributed over the whole etched region with bunching at top region. The height of the nanowalls are found to be ~10.2 and 11.9 µm for sample-1 and sample-2 respectively from the SEM analyses.

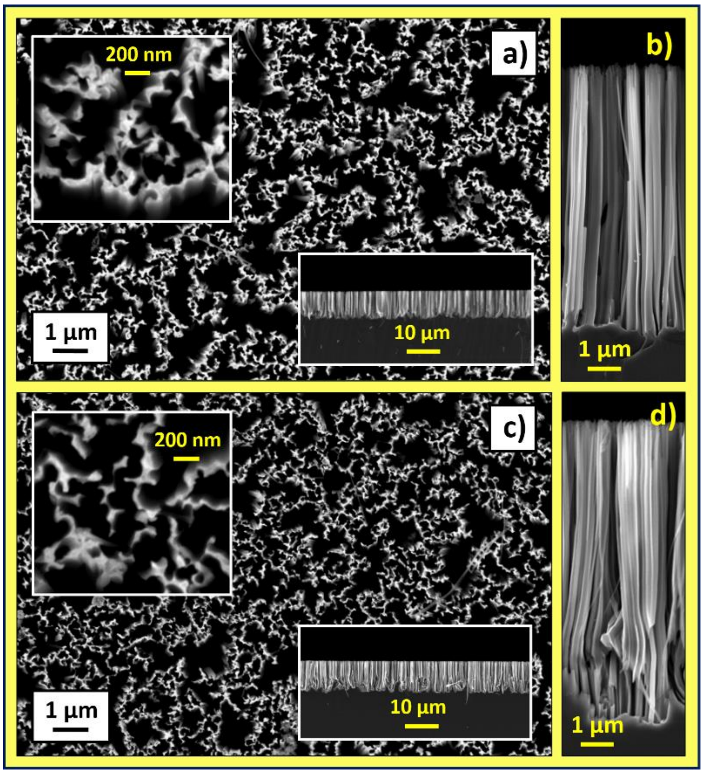

Figure 5.7 Scanning electron micrographs of MACE fabricated SiNWs. ***a, c)*** *Topology of sample-1 and sample-2 respectively. The insets at top left and bottom right display the magnified top and large area cross-section view respectively.* ***b, d)*** *Magnified cross-section of sample-1 and sample-2 respectively.*

5.3.2.2. Cyclic voltammetry (CV) studies

Figure 5.8 summarizes the cyclic voltammetry (CV) of the fabricated SiNWs samples conducted at different scan rates viz. 10, 20, 40, 60, 80 and 100 mV/s. It is observed from the CV curve of sample-1 (Fig. 5.8 a)) in potential window of 0.9 V, from -0.45 to +0.45 against Ag/AgCl electrode that there exists redox peaks around -0.05 V. The analyses on these peaks reveals that the intensity of both oxidation and reduction peaks are almost same for all the scan rates. The plausible origin of the redox peak can be ascribed to the presence of adsorbed water molecules on the SiNWs and deep level trap states in the band gap of Si due to the presence of very small concentration of silver [179]. Fobelets et al. [180] has reported the presence of adsorbed water molecules on Si nanowires even under high

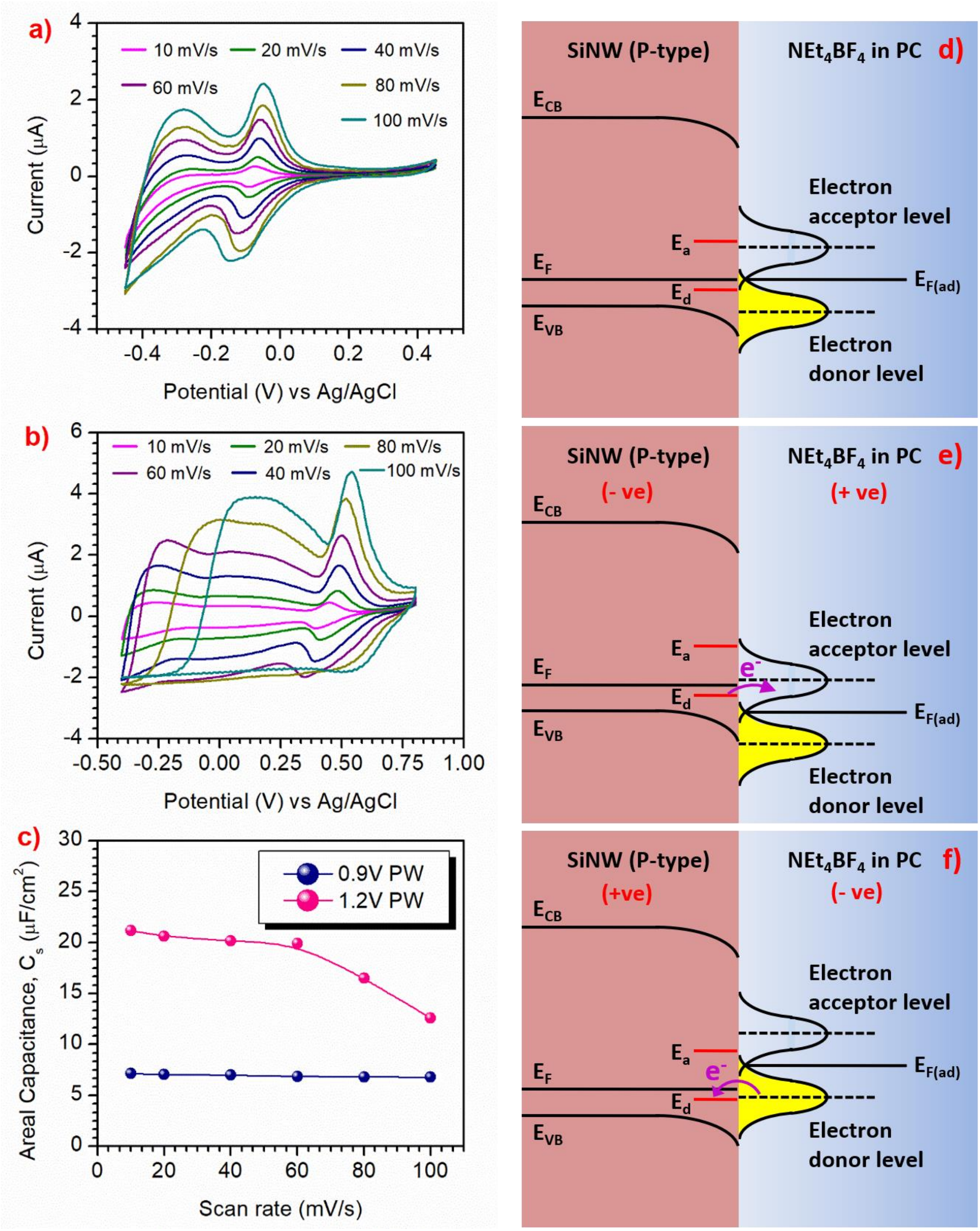

Figure 5.8 Cyclic voltammetry curves of ***a)*** *sample-1 in the potential window 0.9 V (from -0.45 to + 0.45 V) and* ***b)*** *sample-2 in the potential window 1.2 V (from -0.4 to + 0.8 V) at different scan rate.* ***c)*** *Comparison of areal capacitance (C_S) vs. scan rate obtained in 0.9 and 1.2 V potential window.* ***d-f)*** *Schematic illustrating the energy band diagram of Ag related trap level in the band gap of Si, in contact with adsorbed water in the electrolyte (NEt$_4$BF$_4$ in PC) with* ***d)*** *no applied bias,* ***e)*** *an applied +ve bias and* ***f)*** *an applied –ve bias to electrolyte with respect to SiNWs. The large density of surface states causes the pinning of Fermi level, so the space charge region is independent of applied bias.*

vacuum conditions. This adsorbed water provides the required donor/acceptor levels in the electrolyte side. Small concentrations of Ag can be present in the SiNWs because the SiNWs are produced by metal (Ag) assisted chemical etching technique, where SiNWs are seen to be bunched in the present study that hinders the complete removal of Ag after HNO_3 treatment. It is reported that the very small concentration of Ag produce deep level trap states in the band gap of Si [181]. Therefore, as illustrated in the energy band diagram (Fig. 5.8 d)), there will be Ag related trap states in the Si band gap, in contact with the adsorbed H_2O along with its donor/acceptor levels in electrolyte side [179]. The common trap levels associated with Ag are the acceptor level (E_a) and the donor level (E_d) which are positioned ~ 0.56 eV below the conduction band edge (E_{CB}) and ~ 0.23 eV above the valance band edge (E_{VB}) respectively. Since, the present SiNWs are lightly doped p-type (because these are produced by etching lightly doped p-type Si wafer as discussed in chapter 3), the Fermi level (E_F) lies well above the valence band edge. In this case the donor trap (E_d) is filled. When a +ve bias is applied to the electrolyte with respect to the SiNW electrode, electrons from the donor trap moves into the electrolyte and vice-versa when the electrolyte is in the -ve bias as described in Fig. 5.8 e) and 5.8 f), respectively [179]. Therefore, a redox peak is anticipated during cyclic voltammetry. The peaks observed in the above potential range can be attributed to charge transfer process. The CV curves of sample-2, in the potential window of 1.2 V (from -0.4 to +0.8) are displayed in Fig. 5.8 b). The redox peak is observed around 0.5 V in the CV curves. The nature of these redox peaks taking place at higher potential is fairly different from that observed in Fig. 5.8 a). A careful observation reveals that the intensity of reduction peak is comparatively lower than that of the oxidation peaks and also the reduction peaks even disappear at higher scan rate. So, the peaks observed around 0.5 V in Fig. 5.8 b), cannot be attributed to redox peaks arising from Ag related trap levels in Si band gap, in contact with adsorbed H_2O where the oxidation and reduction peaks are coupled to each other. It should be noted that, in the present study, the electrolyte (NEt_4BF_4 in PC) used is highly moisture sensitive. Therefore, the presence of H_2O is always possible in the electrolyte. Hence redox peaks corresponding to oxidation of silicon is anticipated in the CV which occurs at higher potentials. Therefore, the observed redox peak around 0.5 V in Fig. 5.8 b), can be attributed to the surface oxidation of Si or its hydride (which is formed when SiNWs are treated with HF, prior to CV measurement), with the following plausible reactions [97],

$$Si + H_2O \rightarrow SiOH + H^+ + e^- \tag{5.15 a}$$

$$SiH + H_2O \rightarrow SiOH + 2H^+ + 2e^- \tag{5.15 b}$$

The areal capacitance, C_s (capacitance per unit area of the electrode in F/cm^2) of the fabricated SiNWs is estimated from the CV curve using the following expression [182, 183],

$$C_s = \frac{\int IdV}{\nu . A . \Delta V} \tag{5.16}$$

Where, $\int IdV$ is the area under the CV curve, ν is the scan rate, A is the area of the electrode exposed to the electrolyte and ΔV is the potential window. The estimated C_s obtained in the potential windows 0.9 and 1.2 V, at a scan rate of 10 mV/s are ~ 7.1 and 21.1 $\mu F/cm^2$ respectively. It is worth noting that the achieved capacitance value are comparatively lower than that achieved by Sadki et al. in their VLS grown Si nanowires/nanotrees (900 $\mu F/cm^2$) [102]. This can be attributed to following factors: i) the present MACE fabricated Si nanostructures are wall like with the total surface area lower than that of VLS grown Si nanowires/nanotrees and ii) being fabricated by etching lightly doped Si wafer, the nanowalls are lightly doped, whereas the VLS grown Si nanowires/nanotrees are heavily doped. The plot of C_s vs. scan rate obtained for the potential windows 0.9 and 1.2 V is depicted in Fig 5. 8 c). It is manifested that the C_s value obtained in the potential window 0.9 V exhibits an almost constant value for all the scan rates, whereas that obtained in the 1.2 V potential window decreases with scan rate especially at higher scan rate.

5.3.2.3. Galvanostatic charge-discharge (GCD) studies

The galvanostatic charge-discharge (GCD) studies conducted in the potential window of 0.9 V (from -0.45 to +0.45 V) for sample-1 and 1.2 V (from -0.4 to +0.8 V) for sample-2 at different applied currents are displayed in Fig. 5.9 a) and 5.9 b) respectively. It is observed that the GCD curves for both the cases slightly deviate from the ideal linear behaviour observed for double-layer type capacitor electrode. Such behaviour can be attributed to the presence of redox peaks in the CV curve in the region around -0.05 V for the scan in 0.9 V potential window and 0.5 V for the scan in the 1.2 V potential window (Fig. 5.8 a) and 5.8 b) respectively). These are clearly discerned in their respective GCD curves. Therefore, the observed capacitive behaviour of the SiNWs is considered to be due to the combined effect of both the double-layer type and pseudo-type capacitance nature of the electrode-electrolyte system. The areal capacitance, C_s can also be determined from the GCD curves by using the following expression [29, 31],

$$C_s = \frac{I \times t_d}{A \times \Delta V} \tag{5.17}$$

Where, I is the current during discharging process, t_d is the discharging time and other symbols have their usual meaning. The C_s determined from the above expresion, for the above two cases at an applied current of 2μA are 1.1 μF/cm^2 and 14 μF/cm^2 respectively, which are in the same range with that estimated from CV curves.

The cycle life being a significant factor for a elctrochemical capcitor electrode for evaluating its performance, the capacitance retention of the syntheiszed SiNWs are plotted against their cycle number as shown in Fig. 5.9 c). A capcitance loss of 4 and 17 % was observed in 500 cycles for the cases where the potential window is 0.9 and 1.2 V respectively. The reduction in the capacitance value can be ascribed to the pseudocapacitanace nature of the present electrodes. The higher degradation in the 1.2 V potential window case is due to the origin of its redox peaks arising from oxidation of Si and its hydride, which can be concominatly etched by the fluoride ions generated by BF_4^- ions of the electrolyte (NEt_4BF_4). This leads to the consumption of active electrode resulting into the severe degradation of capacitance. Therefore, although the net capacitance value in case of 0.9 V potential window is lower than that obtained in case of 1.2 V potential window, the former exhibits better electrochemical capacitor performance in terms of operational stability.

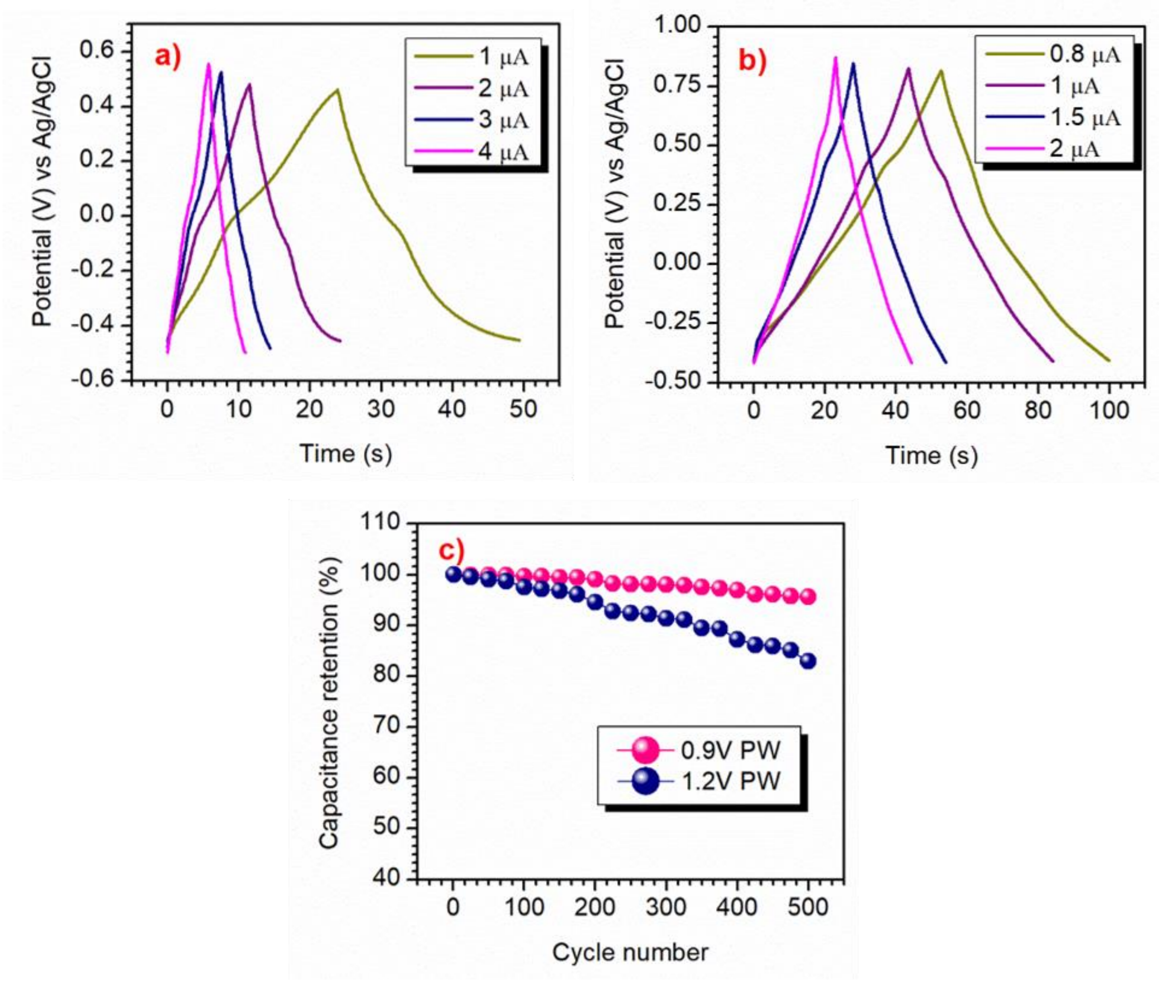

*Figure 5.9 Galvanostatic charge-discharge (GCD) curves at different applied currents for **a)** sample-1 in the potential window of 0.9 V (from -0.45 to +0.45 V) and **b)** sample-2 in the potential window of 1.2 V (from -0.4 to +0.8 V). **c)** Comparison of capacitance retention vs. cycle number obtained in 0.9 and 1.2 V potential windows.*

5.4. Summary

The outcomes of the present chapter are:

- Both pristine and Pt/Pd functionalized SiNWs shows H_2 sensing behaviour. The functionalized SiNWs exhibit enhanced behaviour with Pt and Pd showing better response at low and high temperature respectively.
- Both fabrication and functionalization are achieved by cost-effective and CMOS compatible technique, so the present study opens avenue for scaling-up of these materials as employable hydrogen sensors.
- Electrochemical capacitor studies were conducted on wafer-scale synthesized SiNWs.
- The present electrochemical capacitor study is the first report, on MACE fabricated SiNWs in the NEt_4BF_4 in PC.
- MACE being simple, cost effective and CMOS compatible, the presents study suggests its direct utilization in existing matured silicon microelectronic industry for fabrication of silicon nanostructure based electrochemical capacitor.

References

[1] F. Priolo, T. Gregorkiewicz, M. Galli, T.F. Krauss, Silicon nanostructures for photonics and photovoltaics, Nature nanotechnology, 9 (2014) 19.

[2] K.-Q. Peng, X. Wang, L. Li, Y. Hu, S.-T. Lee, Silicon nanowires for advanced energy conversion and storage, Nano Today, 8 (2013) 75-97.

[3] B. Zhang, J. Jie, X. Zhang, X. Ou, X. Zhang, Large-scale fabrication of silicon nanowires for solar energy applications, ACS applied materials & interfaces, 9 (2017) 34527-34543.

[4] A. Saar, Photoluminescence from silicon nanostructures: the mutual role of quantum confinement and surface chemistry, Journal of Nanophotonics, 3 (2009) 032501.

[5] D.A. Neamen, Semiconductor physics and devices: basic principles, New York, NY: McGraw-Hill2012.

[6] L. Lin, S. Guo, X. Sun, J. Feng, Y. Wang, Synthesis and photoluminescence properties of porous silicon nanowire arrays, Nanoscale research letters, 5 (2010) 1822-1828.

[7] V. Kumar, K. Saxena, A. Shukla, Size-dependent photoluminescence in silicon nanostructures: quantum confinement effect, Micro & Nano Letters, 8 (2013) 311-314.

[8] L. Lin, X. Sun, R. Tao, Z. Li, J. Feng, Z. Zhang, Photoluminescence origins of the porous silicon nanowire arrays, Journal of Applied Physics, 110 (2011) 073109.

[9] C. Meier, A. Gondorf, S. Lüttjohann, A. Lorke, H. Wiggers, Silicon nanoparticles: Absorption, emission, and the nature of the electronic bandgap, Journal of Applied Physics, 101 (2007) 103112.

[10] R. Juhasz, Silicon nanowires, nanopillars and quantum dots: Fabrication and characterization, KTH2005.

[11] Z. Wang, R. Zhang, S. Wang, M. Lu, X. Chen, Y. Zheng, L. Chen, Z. Ye, C. Wang, K. Ho, Broadband optical absorption by tunable Mie resonances in silicon nanocone arrays, Scientific reports, 5 (2015) 1-6.

[12] S.K. Srivastava, D. Kumar, M. Sharma, R. Kumar, P. Singh, Silver catalyzed nano-texturing of silicon surfaces for solar cell applications, Solar Energy Materials and Solar Cells, 100 (2012) 33-38.

[13] Y. Wang, T. Wang, P. Da, M. Xu, H. Wu, G. Zheng, Silicon nanowires for biosensing, energy storage, and conversion, Advanced materials, 25 (2013) 5177-5195.

[14] J. Goldberger, A.I. Hochbaum, R. Fan, P. Yang, Silicon vertically integrated nanowire field effect transistors, Nano letters, 6 (2006) 973-977.

[15] A.I. Hochbaum, R. Chen, R.D. Delgado, W. Liang, E.C. Garnett, M. Najarian, A. Majumdar, P. Yang, Enhanced thermoelectric performance of rough silicon nanowires, Nature, 451 (2008) 163-167.

[16] H.-C. Wu, H.-Y. Tsai, H.-T. Chiu, C.-Y. Lee, Silicon rice-straw array emitters and their superior electron field emission, ACS applied materials & interfaces, 2 (2010) 3285-3288.

[17] P. Hoyer, M. Theuer, R. Beigang, E.-B. Kley, Terahertz emission from black silicon, Applied physics letters, 93 (2008) 091106.

[18] J. Oh, H.-C. Yuan, H.M. Branz, An 18.2%-efficient black-silicon solar cell achieved through control of carrier recombination in nanostructures, Nature nanotechnology, 7 (2012) 743.

[19] M. Otto, M. Algasinger, H. Branz, B. Gesemann, T. Gimpel, K. Füchsel, T. Käsebier, S. Kontermann, S. Koynov, X. Li, Black silicon photovoltaics, Advanced optical materials, 3 (2015) 147-164.

[20] S. Chandrasekaran, T. Nann, N.H. Voelcker, Nanostructured silicon photoelectrodes for solar water electrolysis, Nano Energy, 17 (2015) 308-322.

[21] F. Thissandier, P. Gentile, N. Pauc, T. Brousse, G. Bidan, S. Sadki, Tuning silicon nanowires doping level and morphology for highly efficient micro-supercapacitors, Nano Energy, 5 (2014) 20-27.

[22] J.P. Alper, S. Wang, F. Rossi, G. Salviati, N. Yiu, C. Carraro, R. Maboudian, Selective ultrathin carbon sheath on porous silicon nanowires: materials for extremely high energy density planar micro-supercapacitors, Nano letters, 14 (2014) 1843-1847.

[23] K. Karki, E. Epstein, J.-H. Cho, Z. Jia, T. Li, S.T. Picraux, C. Wang, J. Cumings, Lithium-assisted electrochemical welding in silicon nanowire battery electrodes, Nano letters, 12 (2012) 1392-1397.

[24] M. Ge, X. Fang, J. Rong, C. Zhou, Review of porous silicon preparation and its application for lithium-ion battery anodes, Nanotechnology, 24 (2013) 422001.

[25] M. Gao, M. Cho, H.J. Han, Y.S. Jung, I. Park, Palladium-decorated silicon nanomesh fabricated by nanosphere lithography for high performance, room temperature hydrogen sensing, Small, 14 (2018) 1703691.

[26] F. Demami, L. Ni, R. Rogel, A.-C. Salaun, L. Pichon, Silicon nanowires based resistors as gas sensors, Sensors and Actuators B: Chemical, 170 (2012) 158-162.

[27] B.-R. Huang, Y.-K. Yang, H.-L. Cheng, Rice-straw-like structure of silicon nanowire arrays for a hydrogen gas sensor, Nanotechnology, 24 (2013) 475502.

[28] F.A. Harraz, Porous silicon chemical sensors and biosensors: A review, Sensors and Actuators B: Chemical, 202 (2014) 897-912.

[29] S. Chen, A. van den Berg, E.T. Carlen, Sensitivity and detection limit analysis of silicon nanowire bio (chemical) sensors, Sensors and actuators B: Chemical, 209 (2015) 486-489.

[30] S. Dhanekar, S. Jain, Porous silicon biosensor: Current status, Biosensors and bioelectronics, 41 (2013) 54-64.

[31] R. Wagner, s.W. Ellis, Vapor-liquid-solid mechanism of single crystal growth, Applied physics letters, 4 (1964) 89-90.

[32] W. Zheng, Fabrication of capacitors based on silicon nanowire arrays generated by metal-assisted wet chemical etching, Massachusetts Institute of Technology2016.

[33] L. Chen, W. Lu, C.M. Lieber, Semiconductor nanowire growth and integration, (2014).

[34] H. Jansen, M. de Boer, R. Legtenberg, M. Elwenspoek, The black silicon method: a universal method for determining the parameter setting of a fluorine-based reactive ion etcher in deep silicon trench etching with profile control, Journal of Micromechanics and Microengineering, 5 (1995) 115.

[35] S. Jeong, M.D. McGehee, Y. Cui, All-back-contact ultra-thin silicon nanocone solar cells with 13.7% power conversion efficiency, Nature communications, 4 (2013) 1-7.

[36] Y. Chen, Z. Xu, M.R. Gartia, D. Whitlock, Y. Lian, G.L. Liu, Ultrahigh throughput silicon nanomanufacturing by simultaneous reactive ion synthesis and etching, ACS nano, 5 (2011) 8002-8012.

[37] M.J. Sailor, Porous silicon in practice: preparation, characterization and applications, John Wiley & Sons2012.

[38] D. Dimova-Malinovska, M. Sendova-Vassileva, N. Tzenov, M. Kamenova, Preparation of thin porous silicon layers by stain etching, Thin Solid Films, 297 (1997) 9-12.

[39] X. Li, P. Bohn, Metal-assisted chemical etching in HF/H 2 O 2 produces porous silicon, Applied Physics Letters, 77 (2000) 2572-2574.

[40] K.Q. Peng, Y.J. Yan, S.P. Gao, J. Zhu, Synthesis of large-area silicon nanowire arrays via self-assembling nanoelectrochemistry, Advanced materials, 14 (2002) 1164-1167.

[41] Z. Huang, N. Geyer, P. Werner, J. De Boor, U. Gösele, Metal-Assisted Chemical Etching of Silicon: A Review: In Memory of Prof. Ulrich Gösele, Advanced materials, 23 (2011) 285-308.

[42] H. Han, Z. Huang, W. Lee, Metal-assisted chemical etching of silicon and nanotechnology applications, Nano today, 9 (2014) 271-304.

[43] X. Li, Metal assisted chemical etching for high aspect ratio nanostructures: A review of characteristics and applications in photovoltaics, Current Opinion in Solid State and Materials Science, 16 (2012) 71-81.

[44] W.-K. To, C.-H. Tsang, H.-H. Li, Z. Huang, Fabrication of n-type mesoporous silicon nanowires by one-step etching, Nano letters, 11 (2011) 5252-5258.

[45] K. Peng, J. Zhu, Simultaneous gold deposition and formation of silicon nanowire arrays, Journal of electroanalytical chemistry, 558 (2003) 35-39.

[46] S.K. Srivastava, D. Kumar, S. Schmitt, K. Sood, S. Christiansen, P. Singh, Large area fabrication of vertical silicon nanowire arrays by silver-assisted single-step chemical etching and their formation kinetics, Nanotechnology, 25 (2014) 175601.

[47] N. Geyer, N. Wollschläger, B. Fuhrmann, A. Tonkikh, A. Berger, P. Werner, M. Jungmann, R. Krause-Rehberg, H.S. Leipner, Influence of the doping level on the porosity of silicon nanowires prepared by metal-assisted chemical etching, Nanotechnology, 26 (2015) 245301.

[48] K. Peng, J. Hu, Y. Yan, Y. Wu, H. Fang, Y. Xu, S. Lee, J. Zhu, Fabrication of single-crystalline silicon nanowires by scratching a silicon surface with catalytic metal particles, Advanced Functional Materials, 16 (2006) 387-394.

[49] L. Liu, K.Q. Peng, Y. Hu, X.L. Wu, S.T. Lee, Fabrication of Silicon Nanowire Arrays by Macroscopic Galvanic Cell-Driven Metal Catalyzed Electroless Etching in Aerated HF Solution, Advanced Materials, 26 (2014) 1410-1413.

[50] W. Choi, T. Liew, M. Dawood, H.I. Smith, C. Thompson, M. Hong, Synthesis of silicon nanowires and nanofin arrays using interference lithography and catalytic etching, Nano letters, 8 (2008) 3799-3802.

[51] Z. Huang, H. Fang, J. Zhu, Fabrication of silicon nanowire arrays with controlled diameter, length, and density, Advanced materials, 19 (2007) 744-748.

[52] K. Balasundaram, J.S. Sadhu, J.C. Shin, B. Azeredo, D. Chanda, M. Malik, K. Hsu, J.A. Rogers, P. Ferreira, S. Sinha, Porosity control in metal-assisted chemical etching of degenerately doped silicon nanowires, Nanotechnology, 23 (2012) 305304.

[53] J. De Boor, N. Geyer, J.V. Wittemann, U. Gösele, V. Schmidt, Sub-100 nm silicon nanowires by laser interference lithography and metal-assisted etching, Nanotechnology, 21 (2010) 095302.

[54] D. Wang, R. Ji, S. Du, A. Albrecht, P. Schaaf, Ordered arrays of nanoporous silicon nanopillars and silicon nanopillars with nanoporous shells, Nanoscale research letters, 8 (2013) 42.

[55] K.-Q. Peng, X. Wang, L. Li, X.-L. Wu, S.-T. Lee, High-performance silicon nanohole solar cells, Journal of the American Chemical Society, 132 (2010) 6872-6873.

[56] Y.-J. Hung, S.-L. Lee, K.-C. Wu, Y. Tai, Y.-T. Pan, Antireflective silicon surface with vertical-aligned silicon nanowires realized by simple wet chemical etching processes, Optics express, 19 (2011) 15792-15802.

[57] F.-Y. Wang, Q.-D. Yang, G. Xu, N.-Y. Lei, Y. Tsang, N.-B. Wong, J.C. Ho, Highly active and enhanced photocatalytic silicon nanowire arrays, Nanoscale, 3 (2011) 3269-3276.

[58] L.A. Osminkina, K.A. Gonchar, V.S. Marshov, K.V. Bunkov, D.V. Petrov, L.A. Golovan, F. Talkenberg, V.A. Sivakov, V.Y. Timoshenko, Optical properties of silicon nanowire arrays formed by metal-assisted chemical etching: evidences for light localization effect, Nanoscale research letters, 7 (2012) 1-6.

[59] Y. Liu, G. Ji, J. Wang, X. Liang, Z. Zuo, Y. Shi, Fabrication and photocatalytic properties of silicon nanowires by metal-assisted chemical etching: effect of H 2 O 2 concentration, Nanoscale research letters, 7 (2012) 663.

[60] X. Zhong, Y. Qu, Y.-C. Lin, L. Liao, X. Duan, Unveiling the formation pathway of single crystalline porous silicon nanowires, ACS applied materials & interfaces, 3 (2011) 261-270.

[61] K.W. Kolasinski, Electron transfer during metal-assisted and stain etching of silicon, Semiconductor Science and Technology, 31 (2015) 014002.

[62] C. Chiappini, X. Liu, J.R. Fakhoury, M. Ferrari, Biodegradable porous silicon barcode nanowires with defined geometry, Advanced functional materials, 20 (2010) 2231-2239.

[63] R.A. Lai, T.M. Hymel, V.K. Narasimhan, Y. Cui, Schottky barrier catalysis mechanism in metal-assisted chemical etching of silicon, ACS applied materials & interfaces, 8 (2016) 8875-8879.

[64] C. Chartier, S. Bastide, C. Lévy-Clément, Metal-assisted chemical etching of silicon in HF–H2O2, Electrochimica Acta, 53 (2008) 5509-5516.

[65] J.D. Kim, P.K. Mohseni, K. Balasundaram, S. Ranganathan, J. Pachamuthu, J.J. Coleman, X. Li, Scaling the Aspect Ratio of Nanoscale Closely Packed Silicon Vias by MacEtch: Kinetics of Carrier Generation and Mass Transport, Advanced Functional Materials, 27 (2017) 1605614.

[66] J. Wang, Y. Hu, H. Zhao, H. Fu, Y. Wang, C. Huo, K.Q. Peng, Oxidant Concentration Modulated Metal/Silicon Interface Electrical Field Mediates Metal-Assisted Chemical Etching of Silicon, Advanced Materials Interfaces, 5 (2018) 1801132.

[67] J. Kim, Y.H. Kim, S.-H. Choi, W. Lee, Curved silicon nanowires with ribbon-like cross sections by metal-assisted chemical etching, Acs Nano, 5 (2011) 5242-5248.

[68] W. McSweeney, C. Glynn, H. Geaney, G. Collins, J.D. Holmes, C. O’Dwyer, Mesoporosity in doped silicon nanowires from metal assisted chemical etching monitored by phonon scattering, Semiconductor Science and Technology, 31 (2015) 014003.

[69] B. Moumni, A.B. Jaballah, Correlation between oxidant concentrations, morphological aspects and etching kinetics of silicon nanowires during silver-assist electroless etching, Applied Surface Science, 425 (2017) 1-7.

[70] P. Karadan, S. John, A.A. Anappara, C. Narayana, H.C. Barshilia, Evolution mechanism of mesoporous silicon nanopillars grown by metal-assisted chemical etching and nanosphere lithography: correlation of Raman spectra and red photoluminescence, Applied Physics A, 122 (2016) 669.

[71] A. Najar, A. Slimane, M.N. Hedhili, D. Anjum, R. Sougrat, T. Ng, B. Ooi, Effect of hydrofluoric acid concentration on the evolution of photoluminescence characteristics in porous silicon nanowires prepared by Ag-assisted electroless etching method, Journal of Applied Physics, 112 (2012) 033502.

[72] Y. Qu, L. Liao, Y. Li, H. Zhang, Y. Huang, X. Duan, Electrically conductive and optically active porous silicon nanowires, Nano letters, 9 (2009) 4539-4543.

[73] A.I. Hochbaum, D. Gargas, Y.J. Hwang, P. Yang, Single crystalline mesoporous silicon nanowires, Nano letters, 9 (2009) 3550-3554.

[74] B. Mikhael, B. Elise, M. Xavier, S. Sebastian, M. Johann, P. Laetitia, New silicon architectures by gold-assisted chemical etching, ACS applied materials & interfaces, 3 (2011) 3866-3873.

[75] S. Dhariwal, R. Sharma, Field-assisted recombination in silicon solar cells with heavily doped base: a loss mechanism for the open-circuit voltage, Semiconductor science and technology, 7 (1992) 315.

[76] S.K. Srivastava, D. Kumar, P. Singh, M. Kar, V. Kumar, M. Husain, Excellent antireflection properties of vertical silicon nanowire arrays, Solar Energy Materials and Solar Cells, 94 (2010) 1506-1511.

[77] Y.-T. Lu, A.R. Barron, Nanopore-type black silicon anti-reflection layers fabricated by a one-step silver-assisted chemical etching, Physical Chemistry Chemical Physics, 15 (2013) 9862-9870.

[78] C.I. Yeo, Y.M. Song, S.J. Jang, Y.T. Lee, Wafer-scale broadband antireflective silicon fabricated by metal-assisted chemical etching using spin-coating Ag ink, Optics express, 19 (2011) A1109-A1116.

[79] C.Y. Chen, W.J. Li, H.H. Chen, Tailoring Broadband Antireflection on a Silicon Surface through Two-Step Silver-Assisted Chemical Etching, ChemPhysChem, 13 (2012) 1415-1420.

[80] W. Xie, J. Oh, W. Shen, Realization of effective light trapping and omnidirectional antireflection in smooth surface silicon nanowire arrays, Nanotechnology, 22 (2011) 065704.

[81] J.-P. Lee, S. Choi, S. Park, Extremely superhydrophobic surfaces with micro-and nanostructures fabricated by copper catalytic etching, Langmuir, 27 (2011) 809-814.

[82] L. Cao, T.P. Price, M. Weiss, D. Gao, Super water-and oil-repellent surfaces on intrinsically hydrophilic and oleophilic porous silicon films, Langmuir, 24 (2008) 1640-1643.

[83] T. Wang, G. Liu, J. Kong, C. Wong, Fabrication and Hydrophobic Properties of Column-Array Silicon Using Wood-Structured Silver-Assisted Chemical Etching, Advanced Materials Interfaces, 3 (2016) 1600552.

[84] A. Gouda, M. Elsayed, A. Khalifa, Y. Ismail, M. Swillam, Lithography-free wide-angle antireflective self-cleaning silicon nanocones, Optics letters, 41 (2016) 3575-3578.

[85] Y. Wu, F. Gao, H. Wu, X. Liu, X. Zheng, S.F. Liu, H. Wang, S. Zhou, F. Li, The effects of Ag particle morphology on the antireflective properties of silicon textured using Ag-assisted chemical etching, Journal of Alloys and Compounds, 670 (2016) 156-160.

[86] C. Amri, R. Ouertani, A. Hamdi, H. Ezzaouia, Effect of Silver-Assisted Chemical Vapor Etching on morphological properties and silicon solar cell performance, Materials Science in Semiconductor Processing, 63 (2017) 176-183.

[87] C. Yeo, J.B. Kim, Y.M. Song, Y.T. Lee, Antireflective silicon nanostructures with hydrophobicity by metal-assisted chemical etching for solar cell applications, Nanoscale research letters, 8 (2013) 159.

[88] K. Nishioka, T. Sueto, N. Saito, Formation of antireflection nanostructure for silicon solar cells using catalysis of single nano-sized silver particle, Applied Surface Science, 255 (2009) 9504-9507.

[89] S. Li, W. Ma, X. Chen, K. Xie, Y. Li, X. He, X. Yang, Y. Lei, Structure and antireflection properties of SiNWs arrays form mc-Si wafer through Ag-catalyzed chemical etching, Applied Surface Science, 369 (2016) 232-240.

[90] Y.-J. Hung, S.-L. Lee, K.-C. Wu, Y.-T. Pan, Realization and characterization of aligned silicon nanowire array with thin silver film, IEEE Photonics Journal, 3 (2011) 617-626.

[91] J.-Y. Jung, H.-D. Um, S.-W. Jee, K.-T. Park, J.H. Bang, J.-H. Lee, Optimal design for antireflective Si nanowire solar cells, Solar Energy Materials and Solar Cells, 112 (2013) 84-90.

[92] J.-Y. Jung, Z. Guo, S.-W. Jee, H.-D. Um, K.-T. Park, J.-H. Lee, A strong antireflective solar cell prepared by tapering silicon nanowires, Optics Express, 18 (2010) A286-A292.

[93] C.-C. Chang, Y.-R. Liu, C.-Y. Chen, Highly-antireflective porous Si films prepared with metal-assisted chemical etching, Surface and Coatings Technology, 303 (2016) 232-236.

[94] K. Peng, Y. Xu, Y. Wu, Y. Yan, S.T. Lee, J. Zhu, Aligned single-crystalline Si nanowire arrays for photovoltaic applications, small, 1 (2005) 1062-1067.

[95] H.-C. Chang, K.-Y. Lai, Y.-A. Dai, H.-H. Wang, C.-A. Lin, J.-H. He, Nanowire arrays with controlled structure profiles for maximizing optical collection efficiency, Energy & Environmental Science, 4 (2011) 2863-2869.

[96] L.B. Ahmed, S. Naama, A. Keffous, A. Hassein-Bey, T. Hadjersi, H2 sensing properties of modified silicon nanowires, Progress in Natural Science: Materials International, 25 (2015) 101-110.

[97] M.-P. Liu, C.-H. Li, H.-B. Du, X.-Z. You, Facile preparation of silicon hollow spheres and their use in electrochemical capacitive energy storage, Chemical Communications, 48 (2012) 4950-4952.

[98] J.P. Alper, M. Vincent, C. Carraro, R. Maboudian, Silicon carbide coated silicon nanowires as robust electrode material for aqueous micro-supercapacitor, Applied Physics Letters, 100 (2012) 163901.

[99] S. Chatterjee, R. Carter, L. Oakes, W.R. Erwin, R. Bardhan, C.L. Pint, Electrochemical and corrosion stability of nanostructured silicon by graphene coatings: toward high power porous silicon supercapacitors, The Journal of Physical Chemistry C, 118 (2014) 10893-10902.

[100] B. Tao, J. Zhang, F. Miao, S. Hui, L. Wan, Preparation and electrochemistry of NiO/SiNW nanocomposite electrodes for electrochemical capacitors, Electrochimica Acta, 55 (2010) 5258-5262.

[101] D. Gaboriau, D. Aradilla, M. Brachet, J. Le Bideau, T. Brousse, G. Bidan, P. Gentile, S. Sadki, Silicon nanowires and nanotrees: elaboration and optimization of new 3D architectures for high performance on-chip supercapacitors, RSC advances, 6 (2016) 81017-81027.

[102] F. Thissandier, P. Gentile, T. Brousse, G. Bidan, S. Sadki, Are tomorrow's micro-supercapacitors hidden in a forest of silicon nanotrees?, Journal of Power Sources, 269 (2014) 740-746.

[103] J.B. Allen, R.F. Larry, Electrochemical methods fundamentals and applications, John Wiley & Sons2001.

[104] B.E. Conway, Electrochemical supercapacitors: scientific fundamentals and technological applications, Springer Science & Business Media2013.

[105] J.I. Goldstein, D.E. Newbury, J.R. Michael, N.W. Ritchie, J.H.J. Scott, D.C. Joy, Scanning electron microscopy and X-ray microanalysis, Springer2017.

[106] Z. Luo, A practical guide to transmission Electron microscopy, volume II: advanced microscopy, Momentum Press2015.

[107] B. Cullity, S. Stock, Elements of X-ray diffraction third edition prentice hall upper saddle river, NJ2001.

[108] J.R. Ferraro, Introductory raman spectroscopy, Elsevier2003.

[109] B.C. Smith, Fundamentals of Fourier transform infrared spectroscopy, CRC press2011.

[110] G. Ramer, B. Lendl, Attenuated Total Reflection F ourier Transform Infrared Spectroscopy, Encyclopedia of Analytical Chemistry: Applications, Theory and Instrumentation, (2006).

[111] A. Fox, Optical Properties of Solids, ser, Oxford Master Series in Physics: Condensed Matter Physics. Oxford University …2001.

[112] Y. Peter, M. Cardona, Fundamentals of semiconductors: physics and materials properties, Springer Science & Business Media2010.

[113] S. Del Sorbo, Light scattering in Disordered Textures with Self-Similarity and High Aspect-Ratio.

[114] K. Yee, Numerical solution of initial boundary value problems involving Maxwell's equations in isotropic media, IEEE Transactions on antennas and propagation, 14 (1966) 302-307.

[115] A. Taflove, S.C. Hagness, Computational electrodynamics: the finite-difference time-domain method, Artech house2005.

[116] T. Young, III. An essay on the cohesion of fluids, Philosophical transactions of the royal society of London, (1805) 65-87.

[117] V. Schmidt, J. Wittemann, U. Gosele, Growth, thermodynamics, and electrical properties of silicon nanowires, Chemical reviews, 110 (2010) 361-388.

[118] Y. Qi, Z. Wang, M. Zhang, F. Yang, X. Wang, A processing window for fabricating heavily doped silicon nanowires by metal-assisted chemical etching, The Journal of Physical Chemistry C, 117 (2013) 25090-25096.

[119] M. Birkholz, Thin film analysis by X-ray scattering, John Wiley & Sons2006.

[120] X. Sun, S. Wang, N. Wong, D. Ma, S. Lee, B.K. Teo, FTIR spectroscopic studies of the stabilities and reactivities of hydrogen-terminated surfaces of silicon nanowires, Inorganic chemistry, 42 (2003) 2398-2404.

[121] L. Canham, Handbook of porous silicon, Springer2014.

[122] N.T.N. Lam, N.T. Giang, P.T. Kien, N.D. Dung, N.N. Ha, N-type silicon nanowires prepared by silver metal-assisted chemical etching: Fabrication and optical properties, Materials Science in Semiconductor Processing, 90 (2019) 198-204.

[123] L.U. Vinzons, L. Shu, S. Yip, C.-Y. Wong, L.L. Chan, J.C. Ho, Unraveling the morphological evolution and etching kinetics of porous silicon nanowires during metal-assisted chemical etching, Nanoscale research letters, 12 (2017) 1-12.

[124] K. Peng, A. Lu, R. Zhang, S.T. Lee, Motility of metal nanoparticles in silicon and induced anisotropic silicon etching, Advanced Functional Materials, 18 (2008) 3026-3035.

[125] A. Togonal, L. He, P. Roca i Cabarrocas, Effect of wettability on the agglomeration of silicon nanowire arrays fabricated by metal-assisted chemical etching, Langmuir, 30 (2014) 10290-10298.

[126] Y. Kanemitsu, H. Uto, Y. Masumoto, T. Matsumoto, T. Futagi, H. Mimura, Microstructure and optical properties of free-standing porous silicon films: Size

dependence of absorption spectra in Si nanometer-sized crystallites, Physical review B, 48 (1993) 2827.

[127] A. Cullis, L. Canham, Visible light emission due to quantum size effects in highly porous crystalline silicon, Nature, 353 (1991) 335-338.

[128] V. Lehmann, Electrochemistry of silicon: instrumentation, science, materials and applications, 2002.

[129] N. Geyer, B. Fuhrmann, H.S. Leipner, P. Werner, Ag-mediated charge transport during metal-assisted chemical etching of silicon nanowires, ACS applied materials & interfaces, 5 (2013) 4302-4308.

[130] S. Adachi, Optical dispersion relations for Si and Ge, Journal of applied physics, 66 (1989) 3224-3231.

[131] S.K. Srivastava, C. Rauthan, V. Kumar, P. Singh, Aperiodic silicon nanowire arrays: fabrication, light trapping properties and solar cell applications, Advances in Nanomaterials, Springer2016, pp. 329-363.

[132] P. Spinelli, M. Verschuuren, A. Polman, Broadband omnidirectional antireflection coating based on subwavelength surface Mie resonators, Nature communications, 3 (2012) 1-5.

[133] E.F. Pecora, A. Cordaro, P.G. Kik, M.L. Brongersma, Broadband antireflection coatings employing multiresonant dielectric metasurfaces, ACS Photonics, 5 (2018) 4456-4462.

[134] H.K. Raut, V.A. Ganesh, A.S. Nair, S. Ramakrishna, Anti-reflective coatings: A critical, in-depth review, Energy & Environmental Science, 4 (2011) 3779-3804.

[135] F.-Q. Zhang, K.-Q. Peng, R.-N. Sun, Y. Hu, S.-T. Lee, Light trapping in randomly arranged silicon nanorocket arrays for photovoltaic applications, Nanotechnology, 26 (2015) 375401.

[136] L. Hu, G. Chen, Analysis of optical absorption in silicon nanowire arrays for photovoltaic applications, Nano letters, 7 (2007) 3249-3252.

[137] H. Lin, F. Xiu, M. Fang, S. Yip, H.-Y. Cheung, F. Wang, N. Han, K.S. Chan, C.-Y. Wong, J.C. Ho, Rational design of inverted nanopencil arrays for cost-effective, broadband, and omnidirectional light harvesting, ACS nano, 8 (2014) 3752-3760.

[138] H.M. Branz, V.E. Yost, S. Ward, K.M. Jones, B. To, P. Stradins, Nanostructured black silicon and the optical reflectance of graded-density surfaces, Applied Physics Letters, 94 (2009) 231121.

[139] B. Li, D. Yu, S.-L. Zhang, Raman spectral study of silicon nanowires, Physical Review B, 59 (1999) 1645.

[140] H. Sai, Y. Kanamori, K. Arafune, Y. Ohshita, M. Yamaguchi, Light trapping effect of submicron surface textures in crystalline Si solar cells, Progress in Photovoltaics: Research and Applications, 15 (2007) 415-423.

[141] I. Hwang, D. Choi, S. Lee, J.H. Seo, K.-H. Kim, I. Yoon, K. Seo, Enhancement of light absorption in photovoltaic devices using textured polydimethylsiloxane stickers, ACS applied materials & interfaces, 9 (2017) 21276-21282.

[142] N. Selvakumar, H.C. Barshilia, K. Rajam, Effect of substrate roughness on the apparent surface free energy of sputter deposited superhydrophobic polytetrafluoroethylene coatings: A comparison of experimental data with different theoretical models, Journal of Applied Physics, 108 (2010) 013505.

[143] L. Ostrovskaya, A. Podesta, P. Milani, V. Ralchenko, Influence of surface morphology on the wettability of cluster-assembled carbon films, EPL (Europhysics Letters), 63 (2003) 401.

[144] H.C. Barshilia, D.K. Mohan, N. Selvakumar, K. Rajam, Effect of substrate roughness on the apparent surface free energy of sputter deposited superhydrophobic polytetrafluoroethylene thin films, Applied Physics Letters, 95 (2009) 033116.

[145] N. Vrancken, S. Sergeant, G. Vereecke, G. Doumen, F. Holsteyns, H. Terryn, S. De Gendt, X. Xu, Superhydrophobic breakdown of nanostructured surfaces characterized in situ using ATR–FTIR, Langmuir, 33 (2017) 3601-3609.

[146] D.M. Spori, T. Drobek, S. Zürcher, M. Ochsner, C. Sprecher, A. Mühlebach, N.D. Spencer, Beyond the lotus effect: roughness influences on wetting over a wide surface-energy range, Langmuir, 24 (2008) 5411-5417.

[147] E.Y. Bormashenko, Wetting of real surfaces, Walter de Gruyter GmbH & Co KG2018.

[148] P. Bhattacharya, S. Gohil, J. Mazher, S. Ghosh, P. Ayyub, Universal, geometry-driven hydrophobic behaviour of bare metal nanowire clusters, Nanotechnology, 19 (2008) 075709.

[149] T. Sham, D. Jiang, I. Coulthard, J. Lorimer, X. Feng, K. Tan, S. Frigo, R. Rosenberg, D. Houghton, B. Bryskiewicz, Origin of luminescence from porous silicon deduced by synchrotron-light-induced optical luminescence, Nature, 363 (1993) 331-334.

[150] C. Delerue, G. Allan, M. Lannoo, Theoretical aspects of the luminescence of porous silicon, Physical Review B, 48 (1993) 11024.

[151] J. Parker Jr, D. Feldman, M. Ashkin, Raman scattering by silicon and germanium, Physical Review, 155 (1967) 712.

[152] R. Ghosh, A. Pal, P. Giri, Quantitative analysis of the phonon confinement effect in arbitrarily shaped Si nanocrystals decorated on Si nanowires and its correlation with the photoluminescence spectrum, Journal of Raman Spectroscopy, 46 (2015) 624-631.

[153] R. Tsu, H. Shen, M. Dutta, Correlation of Raman and photoluminescence spectra of porous silicon, Applied physics letters, 60 (1992) 112-114.

[154] S.K. Saxena, R. Borah, V. Kumar, H.M. Rai, R. Late, V. Sathe, A. Kumar, P.R. Sagdeo, R. Kumar, Raman spectroscopy for study of interplay between phonon confinement and Fano effect in silicon nanowires, Journal of Raman Spectroscopy, 47 (2016) 283-288.

[155] M. Kosović, O. Gamulin, M. Balarin, M. Ivanda, V. Đerek, D. Ristić, M. Marciuš, M. Ristić, Phonon confinement effects in Raman spectra of porous silicon at non-resonant excitation condition, Journal of Raman Spectroscopy, 45 (2014) 470-475.

[156] X. Wang, J. Zhang, L. Ding, B. Cheng, W. Ge, J. Yu, Q. Wang, Origin and evolution of photoluminescence from Si nanocrystals embedded in a SiO 2 matrix, Physical Review B, 72 (2005) 195313.

[157] J. Heitmann, F. Müller, L. Yi, M. Zacharias, D. Kovalev, F. Eichhorn, Excitons in Si nanocrystals: confinement and migration effects, Physical Review B, 69 (2004) 195309.

[158] A. Hartel, S. Gutsch, D. Hiller, M. Zacharias, Fundamental temperature-dependent properties of the Si nanocrystal band gap, Physical Review B, 85 (2012) 165306.

[159] G. Ledoux, O. Guillois, D. Porterat, C. Reynaud, F. Huisken, B. Kohn, V. Paillard, Photoluminescence properties of silicon nanocrystals as a function of their size, Physical Review B, 62 (2000) 15942.

[160] J.-A. Yan, L. Yang, M. Chou, Size and orientation dependence in the electronic properties of silicon nanowires, Physical Review B, 76 (2007) 115319.

[161] A. Mirzaei, S.Y. Kang, S.-W. Choi, Y.J. Kwon, M.S. Choi, J.H. Bang, S.S. Kim, H.W. Kim, Fabrication and gas sensing properties of vertically aligned Si nanowires, Applied Surface Science, 427 (2018) 215-226.

[162] W. McSweeney, H. Geaney, C. O'Dwyer, Metal-assisted chemical etching of silicon and the behavior of nanoscale silicon materials as Li-ion battery anodes, Nano Research, 8 (2015) 1395-1442.

[163] J. Baek, B. Jang, M.H. Kim, W. Kim, J. Kim, H.J. Rim, S. Shin, T. Lee, S. Cho, W. Lee, High-performance hydrogen sensing properties and sensing mechanism in Pd-coated p-type Si nanowire arrays, Sensors and Actuators B: Chemical, 256 (2018) 465-471.

[164] K. Hassan, A.I. Uddin, G.-S. Chung, Hydrogen sensing properties of Pt/Pd bimetal decorated on highly hydrophobic Si nanowires, international journal of hydrogen energy, 41 (2016) 10991-11001.

[165] C. Fang, A. Agarwal, E. Widjaja, M.V. Garland, S.M. Wong, L. Linn, N.M. Khalid, S.M. Salim, N. Balasubramanian, Metallization of silicon nanowires and SERS response from a single metallized nanowire, Chemistry of Materials, 21 (2009) 3542-3548.

[166] W. Ye, H. Tong, C. Wang, Study on microcontamination of silver onto p-type crystalline silicon (111) from an aqueous solution using cyclic voltammetry, Microchimica Acta, 152 (2005) 85-88.

[167] M. Baca, K. Cendrowski, W. Kukulka, G. Bazarko, D. Moszyński, B. Michalkiewicz, R. Kalenczuk, B. Zielinska, A Comparison of Hydrogen Storage in Pt, Pd and Pt/Pd Alloys Loaded Disordered Mesoporous Hollow Carbon Spheres, Nanomaterials, 8 (2018) 639.

[168] Y. Qin, D. Liu, T. Zhang, Z. Cui, Ultrasensitive silicon nanowire sensor developed by a special Ag modification process for rapid NH3 detection, ACS applied materials & interfaces, 9 (2017) 28766-28773.

[169] C. Liu, Q. Kuang, Z. Xie, L. Zheng, The effect of noble metal (Au, Pd and Pt) nanoparticles on the gas sensing performance of SnO 2-based sensors: a case study on the {221} high-index faceted SnO 2 octahedra, CrystEngComm, 17 (2015) 6308-6313.

[170] X. Wang, F. Sun, Y. Duan, Z. Yin, W. Luo, Y. Huang, J. Chen, Highly sensitive, temperature-dependent gas sensor based on hierarchical ZnO nanorod arrays, Journal of Materials Chemistry C, 3 (2015) 11397-11405.

[171] S. Ahlers, G. Müller, T. Doll, A rate equation approach to the gas sensitivity of thin film metal oxide materials, Sensors and Actuators B: Chemical, 107 (2005) 587-599.

[172] U. Mishra, J. Singh, Semiconductor device physics and design, Springer Science & Business Media2007.

[173] K. Skucha, Z. Fan, K. Jeon, A. Javey, B. Boser, Palladium/silicon nanowire Schottky barrier-based hydrogen sensors, Sensors and Actuators B: Chemical, 145 (2010) 232-238.

[174] M. Löfdahl, M. Eriksson, M. Johansson, I. Lundström, Difference in hydrogen sensitivity between Pt and Pd field-effect devices, Journal of applied physics, 91 (2002) 4275-4280.

[175] A. Salomonsson, M. Eriksson, H. Dannetun, Hydrogen interaction with platinum and palladium metal–insulator–semiconductor devices, Journal of Applied Physics, 98 (2005) 014505.

[176] F. Yang, K.C. Donavan, S.-C. Kung, R.M. Penner, The surface scattering-based detection of hydrogen in air using a platinum nanowire, Nano letters, 12 (2012) 2924-2930.

[177] M. Johansson, L.-G. Ekedahl, Hydrogen adsorbed on palladium during water formation studied with palladium membranes, Applied surface science, 173 (2001) 122-133.

[178] F. Annanouch, S. Roso, Z. Haddi, S. Vallejos, P. Umek, C. Bittencourt, C. Blackman, T. Vilic, E. Llobet, p-Type PdO nanoparticles supported on n-type WO3 nanoneedles for hydrogen sensing, Thin Solid Films, 618 (2016) 238-245.

[179] A. Shougee, F. Konstantinou, T. Albrecht, K. Fobelets, Cyclic voltammetry peaks due to deep level traps in Si nanowire array electrodes, IEEE Transactions on Nanotechnology, 17 (2017) 154-160.

[180] K. Fobelets, C. Li, D. Coquillat, P. Arcade, F. Teppe, Far infrared response of silicon nanowire arrays, RSC advances, 3 (2013) 4434-4439.

[181] W. McSweeney, O. Lotty, N.V.V. Mogili, C. Glynn, H. Geaney, D. Tanner, J.D. Holmes, C. O'Dwyer, Doping controlled roughness and defined mesoporosity in chemically etched silicon nanowires with tunable conductivity, Journal of Applied Physics, 114 (2013) 034309.

[182] S. Ortaboy, J.P. Alper, F. Rossi, G. Bertoni, G. Salviati, C. Carraro, R. Maboudian, MnO x-decorated carbonized porous silicon nanowire electrodes for high performance supercapacitors, Energy & Environmental Science, 10 (2017) 1505-1516.

[183] S. Ghosh, T. Mathews, B. Gupta, A. Das, N.G. Krishna, M. Kamruddin, Supercapacitive vertical graphene nanosheets in aqueous electrolytes, Nano-Structures & Nano-Objects, 10 (2017) 42-50.

Thesis Highlight

Name of the Student: Anil Kumar Behera
Name of CI: Indira Gandhi Centre for Atomic Research **Enrolment No.:** PHYS 02 2014 04 008
Thesis Title: Fabrication, selected microstructure-property correlations and applications of Si nanowalls
Discipline: Physical Sciences **Sub-Area of Discipline:** Materials Science/Nanotechnology
Date of viva voce: 20/05/2021

- Single crystalline vertically aligned Si nanowalls (SiNWs) atop the Si wafer were successfully fabricated by facile, cost-effective and CMOS compactible 2-step metal assisted chemical etching (MACE) technique (Figure 1). The lightly doped porous SiNWs were also fabricated by the modified MACE (i.e MACE combined with anodic polarization etching)
- The SiNWs fabricated with low etching time exhibits the dual behaviour of excellent antireflectivity and near-superhydrophobicty (Figure 2). These multifunctional behaviours can be utilized for enhancing the efficiency and life time of optoelectronic devices like Si solar cells.
- The lightly doped porous SiNWs shows visible photoluminescence (Figure 3) which arises mostly from quantum structures present in porous SiNWs. This reveal that MACE combined with anodic polarization etching is capable of producing visible light emitting porous SiNWs.
- Both pristine and Pt/Pd functionalized SiNWs (denoted as SiNWs, Pt-SiNWs and Pd-SiNWs) shows H_2 sensing behaviour. The functionalized SiNWs exhibit enhanced behaviour with Pt and Pd showing better response at low and high temperature respectively (Figure 4). Since the fabrication and functionalization of SiNWs are achieved by a simple, low cost and CMOS compatible technique, the present study opens room for scaling-up the process to fabricate employable hydrogen sensors.

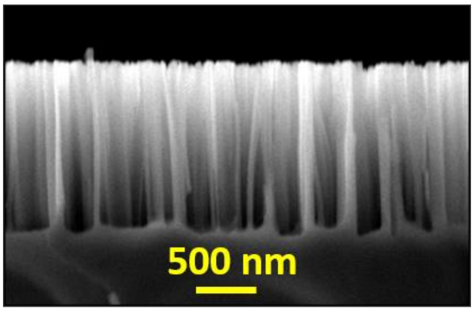

Fig. 1. Scanning electron microscopy image of SiNWs fabricated by metal assisted chemical etching

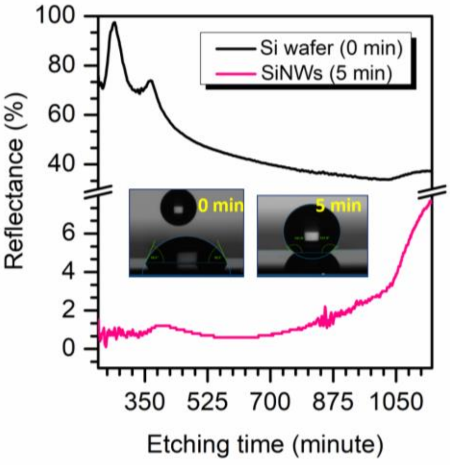

Fig. 2. Spectral reflectance of planar Si wafer (0 minute etching time) and SiNWs (5 minute etching time). Insets show photograph of water droplet atop them.

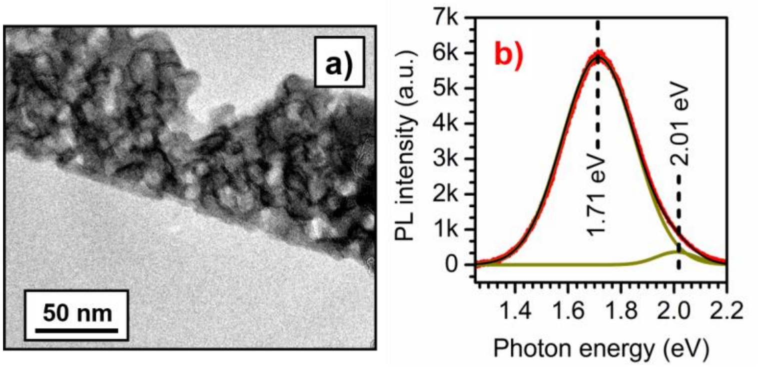

Fig. 3. a) Transmission electron microscopy image porous SiNW. b) Room temperature photoluminescence (PL) spectrum of porous SiNWs (red curve). The fitted PL spectrum has two Gaussian profiles with peak maxima at 1.71 and 2.01 eV as indicated by the dashed lines.

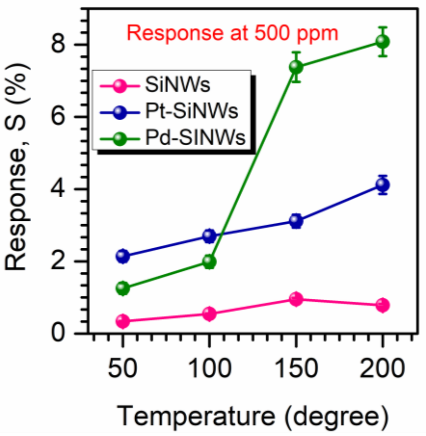

Fig. 4. Display sensor response (S) versus temperature for the SiNWs, Pt-SiNWs and Pd-SiNWs sensor devices..